

# ABSTRACT

Title of dissertation: A Modular Quantum System of Trapped Atomic Ions  
David Hucul, Doctor of Philosophy, 2015

Dissertation directed by: Professor Christopher Monroe  
Joint Quantum Institute,  
University of Maryland Department of Physics and  
National Institute of Standards and Technology

Scaling up controlled quantum systems to involve large numbers of qubits remains one of the outstanding challenges of quantum information science. One path toward scalability is the use of a modular architecture where adjacent qubits may be entangled with applied electromagnetic fields, and remote qubits may be entangled using photon interference. Trapped atomic ion qubits are one of the most promising platforms for scaling up quantum systems by combining long coherence times with high fidelity entangling operations between proximate and remote qubits. In this thesis, I present experimental progress on combining entanglement between remote atomic ions separated by  $\sim 1$  meter with near-field entanglement between atomic ions in the same ion trap. I describe the experimental improvements to increase the remote entanglement rate by orders of magnitude to nearly  $5 \text{ sec}^{-1}$ . This is the first experimental demonstration where the remote entanglement rate exceeds the decoherence rate of the entangled qubits. The flexibility of creating remote entanglement through photon interference is demonstrated by using the interference

of distinguishable photons without sacrificing remote entanglement rate or fidelity. Next I describe the use of master clock in combination with a frequency comb to lock the phases of all laser-induced interactions between remote ion traps while removing optical phase stability requirements. The combination of both types of entanglement gates to create a small quantum network are described. Finally, I present ways to mitigate cross talk between photonic and memory qubits by using different trapped ion species. I show preliminary work on performing state detection of nuclear spin 0 ions by using entanglement between atomic ion spin and photon polarization. These control techniques may be important for building a large-scale modular quantum system.



# A Modular Quantum System of Trapped Atomic Ions

by

David Alexander Hucul

Dissertation submitted to the Faculty of the Graduate School of the  
University of Maryland, College Park in partial fulfillment  
of the requirements for the degree of  
Doctor of Philosophy  
2015

Advisory Committee:

Professor Chris Monroe, Chair/Advisor

Professor Steve Rolston

Professor Luis Orozco

Professor Alexey Gorshkov

Professor Mohammad Hafezi

© Copyright by  
David Alexander Hucul  
2015

## Dedication

*To Tracy*

## Acknowledgments

John Boyd, a famous fighter pilot, once wrote that in order to succeed you must have three things in this order: 1). the right people, 2). good ideas, and 3). the right hardware. Working in the Monroe lab, I've been surrounded by good ideas and the right hardware, but I've been fortunate to have been around some very good people throughout my time at the University of Maryland. Based on my experience trying to perform some tough experiments that require collaboration with a team of people, Boyd's ranking has become obvious to me.

First of all, I'd like to thank my adviser Chris Monroe. When I was an undergraduate at Michigan, I was looking for a summer research job. My freshman mechanics professor, Gus Evrard, offered to introduce me to some physics professors so I could find a summer research job (I didn't want to spend another summer working in a stock room at a large retail store with a target-shaped logo). He introduced me to Chris Monroe, and after talking to Chris (he showed me an ion on a TV screen!) and seeing his physics colloquium that week, I was hooked on atomic physics. Chris was nice enough to hire me for the summer and let me work on a rotating Pringles potato chip as an analogue to an ion trap. Things progressed and I eventually got to work on the first ion trap experiments where an ion was shuttled around a corner in a T-junction ion trap. After leaving for a brief hiatus at MIT, I returned to work with Chris again at the University of Maryland. Chris has been phenomenal to have as an adviser with his physics abilities only surpassed by his ability to manage people. I will look back fondly on my time as a Monrovia.

To say things progressed when I was an undergrad is to leave out my undergrad

day-to day advisor: Winfried Hensinger, then a post-doc. He has an enthusiasm unknown to mankind, and his enthusiasm (and insistence on ordering things overnight) wore off on me. During some of my lowest points in at MIT, learning Winni's enthusiasm as an undergrad kept me in physics. To any other graduate student reading this going through the inevitable tough points of grad school, I can only offer some simple advice. If you love physics, stick with it. Work hard to make your time in graduate school worthwhile and enriching to you.

When I arrived at Maryland, I got to work with two incredibly talented post docs (Peter Maunz and Dzmitry Matsukevich) briefly and with David Hayes for a few years. Dave showed me the ropes of the UMD Monroe lab and was an ideal senior graduate student to work with. Though I was happy to see Dave graduate, I deeply missed physics discussions with him and rounding out the bottom part of the batting order and the right hand side of the outfield in softball with him. Around the same time, I also got to work with undergrad Kenny Lee and post doc Susan Clark. Susan was instrumental in our lab re-learning how to do remote entanglement through photon interference, and Kenny built a lot of the electronics that made our lab run. Volkan Inlek soon joined the lab and quickly became our lab FPGA expert. I blinked, and he quickly became an expert at optics, and experimental design, and now at the time of my graduation, he is the senior graduate student on our experiment. I hope I was able to help Volkan along as much as others have helped me. Clay Crocker (graduate student) and Grahame Vittorini (post doc) joined our lab and were both key to getting the "2 x 1" experiment to work along with the the other subsequent phase control and photon interference experiments.

The atmosphere of the “ion-photon” lab was wonderful and our group prospered as a result, a real testament to Volkan, Clay, and Grahame.

I have to thank some of our industry partners who helped make some of the equipment that made the experimental ideas in this thesis a reality. In 2009 and 2010, many companies stopped performing small, challenging jobs for universities following the financial meltdown in 2008 and 2009. Nadeem Rizvi from Laser Micro-machining Lt’d took on a tough laser machining job making the blade trap ceramic pieces. Daniel Stick and Adrian Casias from Sandia were kind enough to coordinate and gold-coat the laser machined blade trap pieces. Brent Long from Maryland Machine made the complex blade holder, and Photon Gear did an amazing job with the single photon microscope objective. The work in this thesis would not have been possible without all of their help with small batch, challenging, and not necessarily financially lucrative jobs.

I want to thank all of the Monroe lab members I got to work with at Maryland. They are (in no particular order): Paul Hess, Brian Neyenhuis, Phil Richerme, Shantanu Debnath, Ken Wright, Jake Smith, Kale Johnson, David Wong-Campos, Caroline Figgatt, Harvey Kaplan, Chris Rickerd, Lexi Parsagian, Ksenia Sosnova, Geoffrey Ji, Kate Collins, Lenore Koenig, Crystal Senko, Taeyoung Choi, Daniel Brennan, Andrew Manning, Jonathan Mizrahi, Simcha Korenblit, Rajibul Islam, Wes Campbell, Brian Fields, Charles Conover, Le Luo, Emily Edwards, Kihwan Kim, Jon Sterk, Qudsia Quraishi, Ming-Shien Chang, and Steve Olmschenk. I also want to thank Jungsang Kim from Duke for the advice and fruitful discussions throughout the years.

My dad and mom (Dennis and Margo Hucul) and brother (Matthew Hucul) have always been there for me to talk to and offer words of support. I am forever grateful to them.

When I was finishing my master's thesis in early 2009, I hoped that my girlfriend Tracy Wharton would follow me from Boston to College Park. Thankfully she did, and I could not have been luckier. We are now married, we have a daughter, and I can't imagine my life without her. Asking Tracy to marry me was the best and easiest decision I ever made. I could not have done this work without her support.

# Table of Contents

List of Tables	viii
List of Figures	ix
<b>1 Quantum information processors and modularity</b>	<b>1</b>
1.1 Scaling up quantum systems using modular architectures . .	4
<b>2 Experimental considerations</b>	<b>10</b>
2.1 Experimental system considerations . . . . .	10
2.2 Design of a segmented blade trap . . . . .	13
2.3 Vacuum system pump down and non-evaporable getters . . .	15
2.4 The $^{171}\text{Yb}^+$ hyperfine qubit . . . . .	17
2.5 Coherent Manipulations in an ion trap . . . . .	21
<b>3 Photon entanglement of remote qubits</b>	<b>27</b>
3.1 Atom Photon Entanglement . . . . .	30
3.2 Practical interferometer alignment considerations . . . . .	36
3.2.1 Micromotion compensation . . . . .	39
3.2.2 Interferometer mode matching . . . . .	40
3.2.3 Setting fiber strain . . . . .	41
3.3 Photon interference on a beam splitter . . . . .	43
3.3.1 Heralded entanglement using photon frequency qubits	57
3.4 Fast remote entanglement of trapped ions . . . . .	60
3.5 Entanglement of quantum memories using distinguishable photon interference . . . . .	71
<b>4 Phonon entanglement of proximate trapped ion qubits</b>	<b>84</b>
4.1 Entanglement between interacting trapped ions with raman lasers . . . . .	84
4.2 Quantum gates with absolute phase stability . . . . .	93
4.2.1 Multi-qubit entangling gates . . . . .	98
4.3 Phase Stabilization Circuit . . . . .	109
4.4 Implications towards scalability . . . . .	113



5	Entanglement using photons and phonons	115
5.1	Juxtaposition of two entanglement buses . . . . .	118
5.2	A modular quantum system . . . . .	124
6	Dual species ion trap	127
6.1	Entanglement swapping between photonic link qubits and memory qubits . . . . .	131
6.2	State detection of qubits based on entanglement . . . . .	137
7	Outlook	144
A	Appendix	149

## List of Tables

5.1	Resource scaling of modular architectures across different platforms	. 126
5.2	Coherent entanglement distance across different platforms	. . . . . 127

## List of Figures

1.1	Scaling quantum systems . . . . .	4
1.2	Modular network for large scale quantum information processing systems . . . . .	8
2.1	Ion trap geometries for a modular quantum system . . . . .	11
2.2	Ion trap collection optics and geometry . . . . .	14
2.3	Segmented four blade geometry . . . . .	17
2.4	Ion trap vacuum chamber cool down with and without non-evaporable getters . . . . .	18
2.5	Doppler cooling, optical pumping, and state detection of $^{171}\text{Yb}^+$ ions	19
2.6	State detection of $^{171}\text{Yb}^+$ ions . . . . .	22
2.7	Two photon Raman transitions in $^{171}\text{Yb}^+$ . . . . .	23
2.8	Raman transitions with a mode locked 532 nm laser . . . . .	26
3.1	Fiber coupling single ions . . . . .	33
3.2	Filtering $\pi$ polarized light with a single mode optical fiber . . . . .	34
3.3	Ion photon polarization entanglement . . . . .	36
3.4	Single photon interferometer . . . . .	37
3.5	Fiber strain and micromotion compensation optics . . . . .	44
3.6	Photonic modes on a beam splitter . . . . .	46
3.7	Phase evolution of ion photon entanglement . . . . .	54
3.8	Qubit manipulations for generating entanglement between and within modules . . . . .	63
3.9	Heralded entanglement fidelity and rate between modules . . . . .	67
3.10	Photon statistics from interference of identical photons entangled with a qubit . . . . .	73
3.11	Photon statistics from interference of distinguishable photons entangled with a qubit . . . . .	76
3.12	Phase evolution from interference of distinguishable photons . . . . .	78
3.13	Remote atom fidelity using indistinguishable and distinguishable photon interference . . . . .	79
3.14	Phase coherence of remote entangled atoms using interference of distinguishable photons . . . . .	82

4.1	Simplified diagram for absolute phase control in a modular quantum system . . . . .	96
4.2	Optical phase insensitivity of copropagating Raman transitions . . . .	98
4.3	Raman spectrum diagram for phase sensitive and phase insensitive entangling gates . . . . .	99
4.4	stuff . . . . .	101
4.5	Alignment of Raman wavevectors to trapped ion chain . . . . .	105
4.6	Entangling gate phase coherence . . . . .	106
4.7	Entangling gate phase sensitivity . . . . .	108
4.8	Absolute phase control circuit . . . . .	110
4.9	Simplified lock circuit for a modular quantum system . . . . .	112
5.1	Experimental setup and a modular architecture for large scale quantum network . . . . .	118
5.2	Qubit manipulations for generating entanglement between and within modules . . . . .	119
5.3	Entanglement between qubits in the same module without and with heralded entanglement between modules . . . . .	123
6.1	Probability of spontaneous emission from photonic qubits absorbed by neighboring memory qubits . . . . .	129
6.2	State detection of a barium-ytterbium Mølmer-Sørensen gate . . . .	136
6.3	Laser geometry and state detection scheme for nuclear spin 0 ion . . .	139
6.4	Qubit manipulations of a $^{172}\text{Yb}^+$ ion. . . . .	141
6.5	Raman spectrum and Rabi flopping between qubit levels of a $^{172}\text{Yb}^+$ ion. . . . .	143
7.1	A modular quantum system of trapped atomic ions . . . . .	145
7.2	Phase coherent $^{171}\text{Yb}^+$ qubit manipulations across the optical spectrum of a frequency comb . . . . .	146
7.3	Color photograph of a single barium atom . . . . .	148
A.1	Ion trap blades used in this thesis . . . . .	149
A.2	Ion trap blade holder used in this thesis . . . . .	150
A.3	Improved ion trap blade design . . . . .	151
A.4	Improved ion trap blade holder design . . . . .	152
A.5	Optical setup for single photon collection . . . . .	153

## Chapter 1: **Quantum information processors and modularity**

During the twentieth century, there were tremendous technological advances from the first quantum revolution. For example, the understanding of some solid state systems at the quantum level allowed for, among other technologies, the construction of the transistor and the laser which have revolutionized modern life. With the increases in computational power, researchers began investigating strongly-interacting, many-body quantum systems in pursuit of developing novel materials such as high temperature superconductors. Unfortunately, simulating quantum mechanical many-body systems quickly becomes intractable on classical computers. The number of bits needed generally grows as  $2^N$  where  $N$  is the number of two-level particles, prohibiting the use of classical computation to simulate some quantum systems. However, quantum information processors can take over, harnessing the parallel processing ability of quantum mechanics by making use of quantum entanglement, the central resource of a quantum computer [1, 2]. The construction of a quantum computer would have a profound impact on scientific advancement.

Despite the dream of a universal quantum computer, it was not obvious such a machine could realistically work. A brief history of some early developments in quantum information theory is given in [3], which I will paraphrase here. In a

1996 article titled “Quantum Computation: Dream or Nightmare,” Haroche and Raimond wrote [4]

Such a dream scenario would require a machine completely isolated from the outside world. But in fact, quantum coherence is exceedingly sensitive to the unavoidable coupling with the environment... A *single* relaxation event affecting an excited qubit state can destroy the coherence required by the computation.”

Landauer, one of the most prominent figures in information theory, explained in 1995 why quantum information processing seemed to face insurmountable road blocks [5]

There are manufacturing defects, i.e. the Hamiltonian will deviate slightly from its intended form. Furthermore, coupling to the rest of the world will manifest itself as friction and noise. This causes two problems... First of all there is the likelihood, resulting from the irregularities in the Hamiltonian, that the computation will be reflected in its progress along the [computational path], and turned around prematurely. This is familiar to condensed matter physicists... as localization. The second problem relates to... the restandardization ... not available in a Hamiltonian system. Therefore, errors will pile up, and the computation will go off track.

Issues surrounding calibration of a quantum system and the suppression of continuous phase and bit-flip errors made a quantum computer seem like an analog computer, a device with exponential accumulation of error [6]. Even with the promise

of fast factoring algorithms [7], it was not clear the power of a quantum information processor could be physically realized.

Progress in quantum information science continued. In 1995, Cirac and Zoller proposed that a quantum gate could be accomplished with trapped atomic ions [8], followed shortly by the first experimental demonstration of a quantum logic gate by Chris Monroe and David Wineland using trapped  $\text{Be}^+$  ions [9]. In the same year, Shor proved that decoherence could be handled by the use of quantum error correction [10]. However, as pointed out by Haroche and Raimond in 1996, even if error correction can be used to mitigate the effects of decoherence, the error correction would have to be done perfectly [4]. Without perfect error correction, the error correcting process will introduce decoherence and negate the utility of a quantum information processor.

Shor answered this challenge in 1996 by proving that fault-tolerant quantum computation is possible using error correction in the presence of decoherence and imperfect qubit manipulations [11]. With this paper, the idea of a useful quantum information processor was placed on solid theoretical footing. It would be possible to attain speedups on some algorithms using a quantum information processor built from noisy, faulty components and manipulated with imperfect controls. As pointed out by Deutsch [3], these theoretical breakthroughs give insight in to the nature of a quantum processor: a quantum information processor is both analog and digital. Even though imperfect logic gates and decoherence turn the desired quantum states in to statistical mixtures, error correction and fault-tolerance thresholds guarantee that these continuous errors can be discretized and the resulting output of a quantum

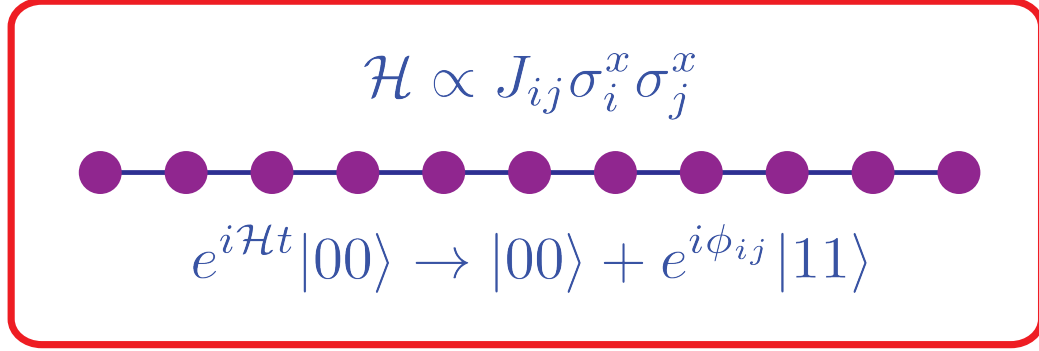


Figure 1.1: Scaling quantum systems. Entanglement, the central resource of quantum information processing, may be created between quantum bits (qubits). Generating entanglement between two qubits may be accomplished by applying a  $\sigma_i^x \sigma_j^x$  interaction with strength  $J_{ij}$  between qubits  $i$  and  $j$  to produce the entangled state  $|00\rangle + e^{i\phi_{ij}} |11\rangle$  with phase  $\phi_{ij}$ . Scaling up a two qubit system to a many-qubit system, as in the figure, introduces problems of qubit addressability in both space and frequency. The diffraction of electromagnetic fields limits the qubit density by limiting the spatial addressability of qubits. Addressing a particular entanglement mode of interacting qubits in the frequency domain becomes challenging as the number of qubits increases, introducing spectral crowding in the frequency domain. These limitations suggest that such a system may reach a maximum manageable size before cross talk limits the utility of adding more qubits.

algorithm can succeed with high probability [3].

With the dream of a quantum information processor backed up by theoretical work, experimental quantum information scientists are confronting the nightmare of scaling up small laboratory demonstrations to large scale information processing devices.

## 1.1 Scaling up quantum systems using modular architectures

Many different types of qubits are used as a means to store and process quantum information such as atoms, ions, superconducting circuits, quantum dots, and



nitrogen vacancy defects in diamond. The creation of entanglement between two qubits directly interacting with each other can be thought of generically as a  $J_{ij}\sigma_x\sigma_x$  interaction with strength  $J_{ij}$  between qubits  $i$  and  $j$ . The application of this interaction to two qubits prepared in the state  $|00\rangle$  in the  $z$ -basis will evolve the system to an entangled state  $|00\rangle + e^{i\phi_{ij}}|11\rangle$  with entangled state phase  $\phi_{ij}$  (generally determined by the time-dependent fields used to entangle the qubits). Scaling up such experiments involves the use of more qubits in proximity to each other. Entanglement between any arbitrary pair of qubits is accomplished by applying gated electromagnetic fields, and qubit control relies on addressing the qubits of interest. Addressing arbitrary pairs of qubits can involve both spatial and frequency selectivity; lasers can be focused down in space to address qubits while control fields can be used to tune individual qubit energy levels allowing for addressability in the frequency domain.

Scaling up these systems typically involves making more complex devices for the storage and the manipulation of many qubits [12–16]. As the number of qubits grow, the number of electromagnetic modes available to make entanglement between an arbitrary pair of qubits increases. Addressing one entanglement-generating mode without cross talk to other modes thus becomes more challenging. High-quality, fast optics can be used to focus a Gaussian laser beam down to diameter  $(4\lambda/\pi)(F/D)$  by using laser at wavelength  $\lambda$  with diameter  $D$  and lens with focal length  $F$ . The spatial addressability, and thus the qubit density, is therefore limited by the diffraction of electromagnetic fields. In addition, spontaneous emission of photons associated with initializing the qubits to a pure quantum state can impose severe limitations on

the qubit density (see Chapter 6). Addressing particular qubit entanglement modes in the frequency domain is limited by the finite frequency bandwidth over which the qubits can be tuned. Increasing the number of qubits increases the entanglement mode spectral density, resulting in off-resonant cross talk between different entanglement modes from the gated electromagnetic control fields. This may be overcome by decreasing the intensity of the electromagnetic fields used to create entanglement at the cost of entangling gate speed, potentially giving back algorithmic speedups associated with increasing numbers of qubits.

These significant challenges suggest implementations of large scale quantum information processors may reach a maximum “manageable” number of qubits before spectral crowding and cross talk limit further scaling. It will likely be useful to limit the interactions between qubits by placing a manageable number of qubits into elementary logic modules. Each module could then be connected by a flexible and re-configurable quantum network as shown in Fig. 1.2. The number of qubits could then be increased by adding more modules without increasing spectral crowding or cross talk between qubits in different modules. The reduced qubit connectivity will result in overhead, but the ability to reconfigure the connectivity may prove useful [17].

Trapped atomic ions confined in multi-zone ion traps provide one type of modular architecture. Large collections of qubits may be shuttled to different interaction zones and re-arranged in complex, junction ion traps [9, 18, 19]. Limiting cross talk and spectral crowding may be accomplished by shuttling ions away from interaction zones in the ion trap array. The elementary modules of multizone ion traps are

different trapping zones, and the reconfigurable interactions are realized by adiabatically moving the qubits throughout the ion trap. Physically adjacent trapped ion qubits may be entangled using laser fields and the coulomb interaction. In addition to using the coulomb interaction between ion qubits, the interference of photons on a beam splitter and subsequent photon detection can herald entanglement between remote ion qubits in different vacuum chamber modules. Though this second type of entanglement generation is necessarily probabilistic, the remote entanglement rate may be faster than the decoherence rate of the qubits [20]. In this architecture, each ion trap serves as an elementary module. The modules are connected through photon interference, and this network may be reconfigured with the aid of photonic interconnect switches (see Fig. 1.2).

This thesis presents some experimental work on realizing a modular architecture composed of trapped  $^{171}\text{Yb}^+$  ions in separate, remote ion trap modules. Chapter 2 of this thesis summarizes work on designing a segmented, four blade ion trap that is both small (facilitating quantum gates between proximate qubits) and optically open (facilitating efficient light collection for fast entanglement of remote qubits). In addition, Chapter 2 reviews some coherent manipulations of  $^{171}\text{Yb}^+$  ions in this ion trap. Chapter 3 shows experimental progress on increasing the remote entanglement rate between distant  $^{171}\text{Yb}^+$  ions by orders of magnitude to nearly  $5 \text{ sec}^{-1}$ . This is the first experimental demonstration where the remote entanglement rate exceeds the decoherence rate of the entangled qubits [20]. The flexibility of quantum networks for creating remote entanglement through photon interference is demonstrated by using the interference of distinguishable, non-identical photons to

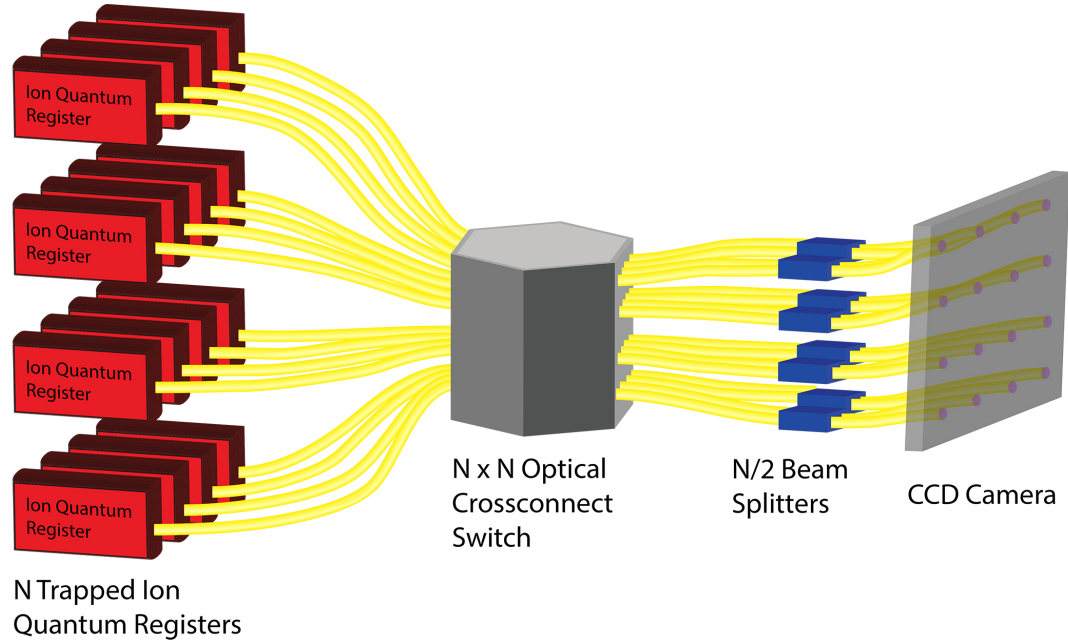


Figure 1.2: Modular network for large scale quantum information processing systems. Cross talk in both space and the frequency domain may limit the maximum number of manageable proximate qubits in a quantum system. Quantum systems may still be scaled up to encompass more qubits by making use of modular architectures. Interactions between qubits in different modules may be limited by separating and isolating the qubits. Qubits in different modules may still be entangled by making use of heralded photon interference. Single photons emitted from qubits in different modules can interfere on a beam splitter, and subsequent measurement of the single photons can project qubits in remote modules into an entangled state. The use of a reconfigurable photonic interconnect switch allows different modules to be entangled in a quantum network with a flexible architecture.

create entanglement between remote qubits without sacrificing remote entanglement rate or fidelity. Chapter 4 shows experimental work on locking the entangled state phases throughout a modular architecture to a single, high quality master clock despite using two different entanglement buses (lasers and spontaneously emitted photons) for entanglement. Chapter 5 shows experimental work done on combining both photon and phonon interactions to create entanglement within and between ion trap modules to create a small quantum network. Chapter 6 shows early experimental work on combining two different types of qubits in a modular architecture

to avoid cross talk between the two different entanglement buses. One type of qubit serves as the photonic link qubit for generating entanglement between modules while the other serves as quantum memory for information processing within each module.

## Chapter 2: **Experimental considerations**

### 2.1 **Experimental system considerations**

Operating a modular quantum information processor using trapped ions requires special attention to ion trap and vacuum chamber design as an integrated system. This kind of architecture has two competing requirements; the ion trap should be small, facilitating high secular frequencies, and the ion trap should be optically open to collect single photons with high efficiency. Trapped ions with high secular frequencies result in lower mean vibrational number  $\bar{n}$ , making entangling gates using the Mølmer-Sørensen interaction less sensitive to noise [21]. The relative stability to noise is important given the time-scales involved in the experiment; the Mølmer-Sørensen entangling gate between proximal qubits must be stable to typical laboratory noise sources, such as slow drifts of the ion transverse motional modes while remote qubits are being entangled through probabilistic photon interference. In addition to efficient light collection, optically open ion traps facilitate flexible laser access from multiple directions, allowing for the variety of qubit manipulations necessary in modular architectures, particularly with multiple qubit species within each module (see Chapter 6).

The work in this thesis makes use of high numerical aperture, free space col-

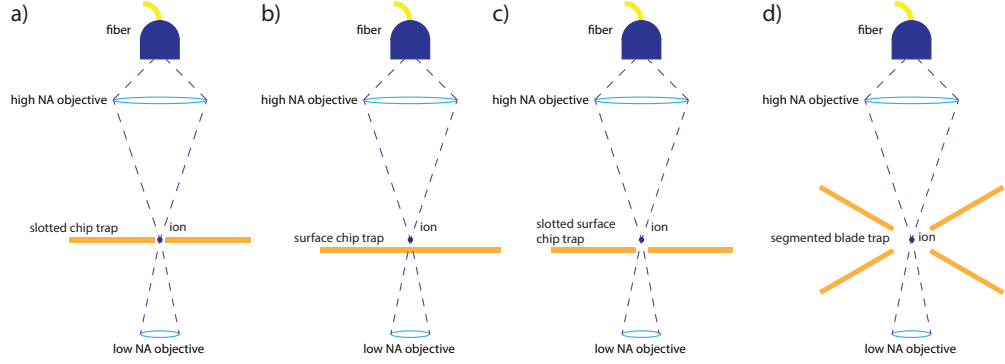


Figure 2.1: Ion trap geometries for a modular quantum system. Alignment of a single mode optical fiber to an atom through a high numerical aperture microscope objective is challenging. With a  $\text{NA} = 0.6$  objective, displacing the ion by  $\sim 200$  nm decreases the total photon flux through the fiber by  $\sim 50\%$ . A geometry with optical access through the ion trap to a lower NA objective is very useful for alignment of a trapped ion to a fiber. Light can be sent through the fiber where it is focused near the trapped ion. The low NA objective then images the fiber and the ion on a CCD camera so that the fiber may be overlapped with the ion. **(a)** A slotted chip trap geometry with a trapped ion. While there is optical access for initial alignment of a fiber to an ion, laser access for qubit manipulations is severely hampered by the large dimensions of the high NA collection optics. Laser access orthogonal to the single photon collection axis is restricted by the ion trap substrate. **(b)** Surface chip traps without a slot provide optical access for laser by skimming the trap surface, but lack of a slot makes alignment of the optical fiber to the ion challenging. **(c)** A slotted surface trap provides laser access orthogonal to the single photon collection axis. The slotted design of the ion trap simplifies alignment of the fiber to the ion. Care must be taken in the chip and chip carrier design to accommodate highly converging and diverging laser beams for individual addressing of trapped ions. **(d)** Three dimensional, segmented blade trap consisting of four blades (side on view in figure). There is ample optical access along the single photon collection access. In addition, there is ample room for laser access orthogonal to the single photon collection axis.

lection optics that focus light into single mode optical fibers. The requirements for aligning the single photon collection optics so that the photons are efficiently coupled in to an optical fiber are challenging; alignment requires adjusting 10 degrees of freedom (3-D translation, pitch, and yaw of the optical fiber and the high NA objective) per ion trap. Making use of an ion trap with optical access for two imaging systems sharing a common axis facilitates alignment of the high NA objective to the fiber. Using this type of geometry places important restrictions on the classes of ion traps useful for modular architectures (see Fig. 2.1). Ion traps without optical access in one direction make alignment of the high NA objectives challenging. The use of a high NA objective (single photon collection) and a low NA objective (for alignment of the high NA objective) along a common axis severely restricts laser access along this axis. Transverse laser access to this imaging axis is important for addressing the ions' modes of motion with Raman transitions to realize an entangling interaction. Additionally, each ion trap should be able to control chains of ions necessitating a segmented ion trap.

A large effort to fabricate scalable ion traps on chips has produced a wide variety of ion trap designs that can be broadly broken down in to several classes. Slotted planar traps (see Fig. 2.1a) confine ions in a slot of a surface electrode structure. Though this geometry provides an open optical axis, there is no azimuthal laser access and laser access along the collection direction is highly restricted by the objective optics. Non-slotted surface traps confine ions above a surface patterned with electrodes. Non-slotted traps will be challenging to use in this architecture due to lack of optical access along the single photon collection axis. The final class



of traps is a slotted surface trap where the ion is trapped above a slotted chip. This geometry provides through access and azimuthal laser access, but care must be made to account for the free space propagation of a Gaussian laser beam. The chip carrier must be etched back significantly to allow clearance for tightly focused beams. At the commencement of this research, such an ion trap did not exist.

A natural solution to these design requirements is to use a variation on a four rod ion trap: a segmented blade trap design. This geometry is optically open, can be made small, and has optical access for a single photon collection system as well as azimuthal access for laser beams to carry out physics experiments. Because the electrode structure is three dimensional, the trap depth can be several electronvolts and trapping lifetime is measured in days. However, this ion trap is hand assembled and scaling up to many modules will be challenging. Further development of chip-based ion traps with appropriate geometries will be crucial for realizing a scalable version of the architecture presented in this thesis.

## 2.2 Design of a segmented blade trap

Each blade is made out of alumina and was laser machined by Laser Micro Machining Lt'd. There are four cuts in each blade to define five segments for controlling the confining pseudopotential. Two of the blades are for application of RF and are completely gold coated so each segment is electrically shorted. The other two blades have a patterned gold coating so each segment is electrically isolated. The gaps between electrodes is  $50\text{ }\mu\text{m}$  and was limited by the smallest slot available

from the laser machining company.

The blades were gold coated by Sandia National Labs. A thin titanium layer was applied to the ceramic blades followed by a  $1\text{ }\mu\text{m}$  layer of evaporated gold. Harsh cleaning of the blades at high temperatures was necessary because of a surface finish applied to the ceramic substrate during the laser machining process.

The blade trap used in the experiments in this thesis could have been improved by lengthening the outer segments on each blade to reduce stray RF fields along the axial direction of the ion chains. An updated design was constructed and is currently being used (see Appendix).

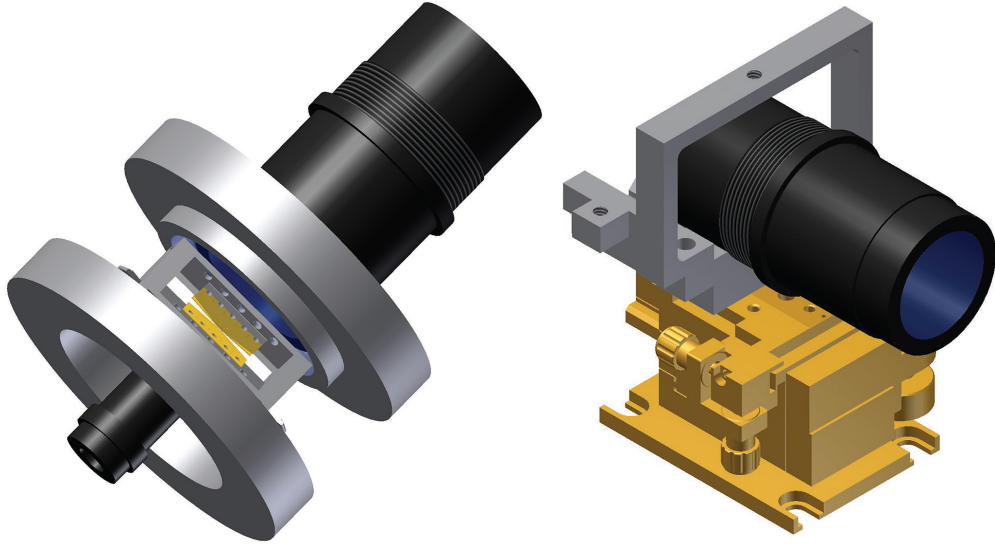


Figure 2.2: Ion trap collection optics and geometry. The common axis shared by the high NA microscope objective and the low NA objective are shown with their relationship to the ion trap and re-entrant vacuum viewports. Light from an optical fiber is focused by the high NA objective on to the ion, and the low NA objective simultaneously images the fiber and the ion to facilitate alignment. The high NA microscope objective is held in place by two ring clamps or by a single nylon tipped screw in a vee-block as shown in the figure. The high NA objective and free space collection objectives define an optical axis. Laser beams may be brought in orthogonal to this axis for manipulation of trapped ions.

## 2.3 Vacuum system pump down and non-evaporable getters

The use of non-evaporable getters (NEGs) for achieving ultra high vacuum has proved useful in ion trap chambers as a replacement for tradition titanium sublimation pumps. TiSub pumps are activated by heating a titanium filament, spraying titanium in the vacuum chamber. Gases like molecular hydrogen stick to the surface of titanium, and the hydrogen can be buried by subsequent heating of the titanium filament. High pumping speeds are achieved by covering a large surface area with the metal. The pumping speed and capacity are determined by the surface area. In order to maintain high pumping speeds, the sublimation pump filament needs to be heated several times per year, resulting in down time of order one day as the pressure recovers.

NEGs are typically made of metal alloys containing zirconium, vanadium, and iron. The getter material is activated by heating the material. Gas is ejected from the surface and the bulk of the material, and upon cooling, the NEG metal alloy acts as a pump. These materials have very high pumping speeds for molecular hydrogen, but the capacity of the material is given by the volume of the getter. The hydrogen molecular bond is broken when it comes in to contact with the metal surface, and the hydrogen atoms migrate into the bulk of the material. The pump speed remains roughly constant. Once activated, NEGs will need re-activation every few decades given the background pressure typical in ion trap experiments. The vacuum chambers used in experiments described in this thesis made use of Capacitorr D400 NEG cartridges from SAES. These NEGs have a hydrogen pumping speed of  $\sim 400$  liters

/ sec at pressures below 0.01 Torr at room temperature and a capacity of 900 Torr liters.

A test vacuum chamber was constructed for testing NEG cartridges. The test chamber had an NEG cartridge from SAES (Capacitorr D 400), an ion pump, and an ion gauge that could be valved off from the central part of the chamber with vacuum valves. The test chamber was heated to 200 C while being pumped with a turbo pump. The ion gauge was turned on at high temperature, and the chamber was baked at 200 C for 14 days to test the cartridge activation without further heating of the NEG element. Upon cooling the test chamber, the pressure fell to  $< 1.0 \times 10^{-11}$  Torr when the vacuum chamber temperature reached room temperature. The ion pump was switched off to allow only the NEG to pump the vacuum chamber. The pressure remained below  $1.0 \times 10^{-11}$  Torr for 48 hours before the experiment was terminated.

All pumping sources were valved off and the pressure inside the chamber was allowed to increase to  $\sim 2 \times 10^{-10}$  Torr. If the getter cartridge pumped the chamber and the ion pump was valved off, the pressure decreased below  $1 \times 10^{-11}$  Torr in about 3 min. If the getter cartridge was valved off and the ion pump was the allowed to pump the chamber, the pressure fell from  $1.8 \times 10^{-11}$  Torr to below  $1 \times 10^{-11}$  Torr in  $\sim 40$  seconds.

Full activation of the getter cartridge was attempted at UHV pressures by running current through the NEG material and using the ion pump to remove the ejected gas from the bulk of the getter material. The pressure spiked to  $10^{-3}$  Torr, and the vacuum pressure did not recover to UHV pressures for the next 72 hours.

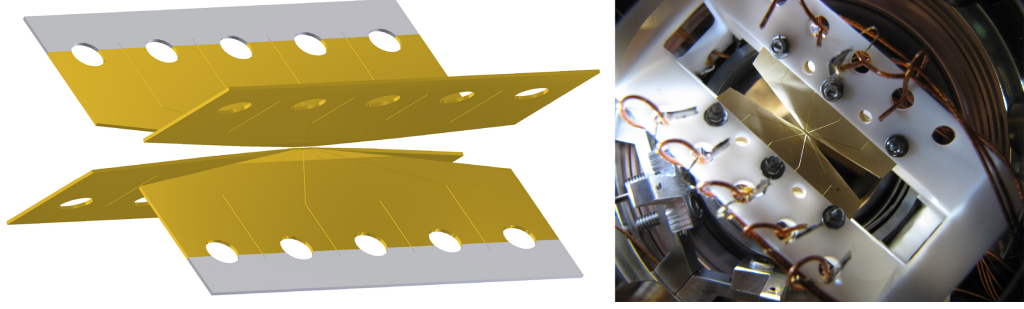


Figure 2.3: Segmented four blade geometry. This ion trap can have small dimensions for tightly confining the ions while being optically open. The photo shows the trap mounted in the vacuum chamber. Schematics with dimensions are in the appendix.

While fully activating the getter cartridge, a turbo pump should be used to pump out the gas ejected from the getter bulk material.

The vacuum chambers used for experimental work in this thesis did not have titanium sublimation pumps. NEG cartridges were used as an alternative. The cartridges were activated while the chamber was at room temperature and being pumped by a turbo pump. The getter cartridge was activated using 4 A of current for 60 min. The vacuum chambers were then slowly heated to 195 C over a period of 24 hours while being pumped with a turbo pump. After reaching 195 C, the chamber was switched over to an ion pump. After being baked for 10 days at 195 C, the chamber was allowed to slowly cool while the vacuum pressure was monitored. The resulting pressure decrease can be seen in Fig. 2.4. At  $\sim 65$  C, the pressure began to decrease sharply and fell below the  $10^{-11}$  Torr limit of the ion gauge.

## 2.4 The $^{171}\text{Yb}^+$ hyperfine qubit

The  $^{171}\text{Yb}^+$  isotope has nuclear spin  $\frac{1}{2}$  and thus has two hyperfine manifolds. The  $^2S_{1/2}$  ground state manifold has  $|F, m_F\rangle = |0, 0\rangle \equiv |0\rangle$  and  $|1, 0\rangle \equiv |1\rangle$  levels

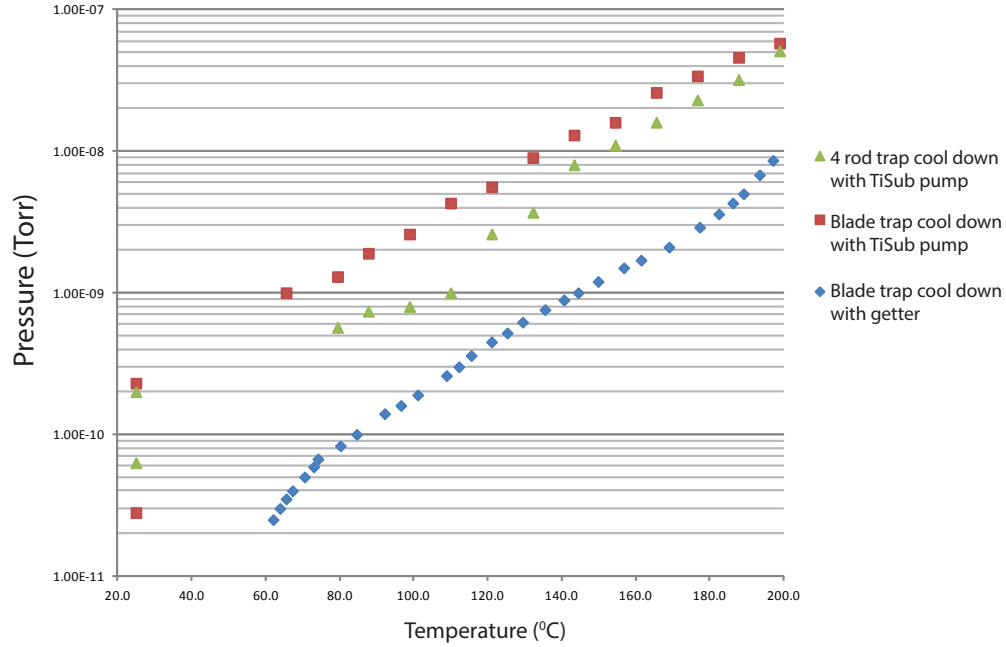


Figure 2.4: Ion trap vacuum chamber cool down with and without non-evaporable getters (NEG). The three data sets show the vacuum pressure as a function of cooling down of vacuum chambers of  $\sim 200$  C to room temperature with a titanium sublimation pump and with an NEG. The squares and triangles show the pressure of two vacuum chambers with an ion pump and a TiSub pump. After reaching room temperature, the TiSub pump is fired several times over the course of a few days to bring the pressure from  $10^{-10}$  Torr to  $10^{-11}$  Torr. A chamber with an NEG (no TiSub pump) starts with lower pressure and experiences a sudden drop in vacuum pressure around 65 C as the NEG begins to act as a pump. Although measuring pressures lower than  $2.0 \times 10^{-11}$  Torr was possible with this vacuum chamber, the pressure dropped faster than the ion gauge updated near the final diamond-shaped data point.

that are magnetic field independent at zero field and have a relatively small second-order Zeeman shift at finite magnetic field of  $311B^2$  Hz with the magnetic field measured in Gauss [22]. The hyperfine frequency of the two levels is 12.642812118 GHz.

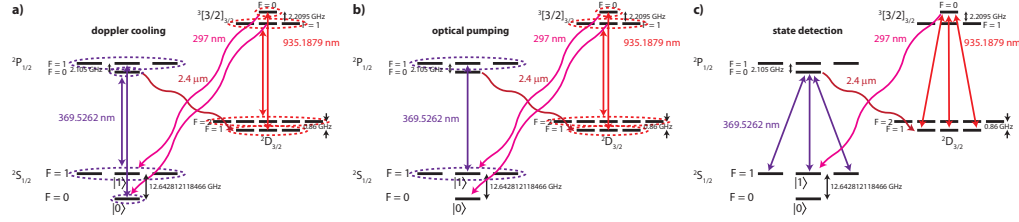


Figure 2.5: Doppler cooling, optical pumping, and state detection of  $^{171}\text{Yb}^+$  ions. **(a)** Doppler cooling of  $^{171}\text{Yb}^+$  ions. The dotted circles indicate  $\pi$  and  $\sigma^\pm$  laser light between the level manifolds. Doppler cooling drives all allowed transitions to maximize laser scatter from the trapped atom. **(b)** Optical pumping to the  $|0\rangle$  state is accomplished by exciting the  $F = 1$  to  $F = 1$  transition between the  $S_{1/2}$  and  $P_{1/2}$  manifolds. Each  $F = 1$  excited state level has probability  $1/3$  to decay to the  $|0\rangle$  state. Re-pump levels are indicated in the figure to account for the small branching ratio to the low lying  $D_{3/2}$  level. **(c)** State detection of an atom in the state  $|1\rangle$ . Laser light resonant with the  $F = 1$  to  $F = 0$  transition from the  $S_{1/2}$  to  $P_{1/2}$  states results in differential fluorescence between the  $|1\rangle$  and  $|0\rangle$  states.

This hyperfine qubit may be laser cooled using standard techniques by stabilizing a laser resonant with the  $F = 1 \leftrightarrow F = 0$  electronic transition between the  $S_{1/2}$  and  $P_{1/2}$  levels. The addition of frequency sidebands at  $12.6 + 2.1$  GHz are required to bridge the hyperfine splitting in the  $2S_{1/2}$  ground state and  $2P_{1/2}$  excited state so the trapped ion is not off resonantly pumped to the  $|0\rangle$  state. All laser polarizations are needed for laser cooling ( $\sigma^\pm$  and  $\pi$  polarization), and a finite magnetic field must be applied to avoid coherent population trapping [22, 23]. In addition, a laser near 935 nm is needed, along with frequency sidebands, to depopulate the  $2D_{3/2}$  state through the  $3[3/2]_{1/2}$  state. Decay from the  $|0,0\rangle$  state in the

$P_{1/2}$  excited state to the  $F = 1$  levels of the  $^2D_{3/2}$  state occurs with probability 0.005, so addition of light resonant with the  $F = 1 \leftrightarrow F = 0$  transition between the  $^2D_{3/2}$  and  $^3[3/2]_{1/2}$  is needed. The atom will decay from the  $^3[3/2]_{1/2}$   $F = 0$  state back to the  $F = 1$  levels in the  $S_{1/2}$  state. The population in the  $F = 1$  states of the  $P_{1/2}$  manifold can decay to the  $F = 2$  level of the  $^2D_{3/2}$  state, and this state can be transferred to the  $F = 1$  states in the  $^3[3/2]_{1/2}$  electronic state. These levels decay back to  $F = 1$  and  $F = 0$  levels in the  $S_{1/2}$  ground state.

State preparation of a pure quantum state  $|0\rangle$  is done by switching off the Doppler cooling laser sidebands at 14.7 GHz and switching on frequency sidebands at 2.105 GHz to excite the atom to the  $F = 1$  levels in the  $P_{1/2}$  manifold. These levels can decay to the  $|0\rangle$  state, and while in this state, the laser is detuned from the atom by 12.6 GHz. The atom remains in the state  $|0\rangle$  with high probability.

State detection makes use of differential fluorescence between the  $|0\rangle$  state and the  $F = 1$  levels, one of which is the qubit state  $|1\rangle$ . If a laser is resonant with the  $F = 1 \leftrightarrow F = 0$  electronic transition between the  $S_{1/2}$  and  $P_{1/2}$  levels, the  $F = 1$  levels scatter photons while the  $F = 0$  state is detuned by 12.6 GHz and scatters photons with low probability. Error in state detection is dominated by the off-resonant excitation of the  $F = 1$  levels in the  $S_{1/2}$  manifold to the  $F = 1$  levels in the  $P_{1/2}$  state, where the atom can decay to  $|0\rangle$ , mixing the qubit states. Many references discuss state detection based on differential fluorescence and errors associated with off-resonant excitation in great detail [13, 22, 24–26].

The probability the atom is in the  $|1\rangle$  state is measured by analyzing the histogram of number of photons detected over multiple experimental trials. Figure



2.6a shows the number of photons detected in 300  $\mu\text{s}$  after optically pumping the atom to  $|0\rangle$  and preparing the  $|1\rangle$  state with a resonant microwave  $\pi$  pulse. Zero photons are detected with high probability if the  $|0\rangle$  state is prepared. The minimum overlap of the two histograms occurs at two photons; if two or more photons are detected, the atom is in the state  $|1\rangle$ .

The work in this thesis used PMTs without spatial resolution for counting photons, so the two atom states  $|01\rangle$  and  $|10\rangle$  could not be distinguished from each other. In addition, there is significant overlap of the single atom  $|1\rangle$  state and the two atom  $|11\rangle$  state. The histograms are not Poisson distributions because of off-resonant scattering by coupling to the  $F = 1$  states in the  $^2P_{1/2}$  state [26]. The probability of correctly identifying the state  $|01\rangle$  or  $|10\rangle$  is measured as a function of discriminator value and is shown in the red data in Fig. 2.6b with a detection time of 300  $\mu\text{s}$ . The figure also shows the probability of incorrectly identifying the state  $|11\rangle$  as a function of discriminator value in blue. The optimum discriminator value for discerning  $|10\rangle$  or  $|01\rangle$  from  $|11\rangle$  is where the data meet. The discriminator value can be optimized for each detection time and is shown in Fig. 2.6c.

## 2.5 Coherent Manipulations in an ion trap

Resonant rotations of a qubit may be described by  $|\psi'\rangle = R(\theta, \phi)|\psi\rangle$  where the initial qubit wavefunction  $|\psi\rangle$  is multiplied by a rotation matrix  $R(\theta, \phi)$  to produce

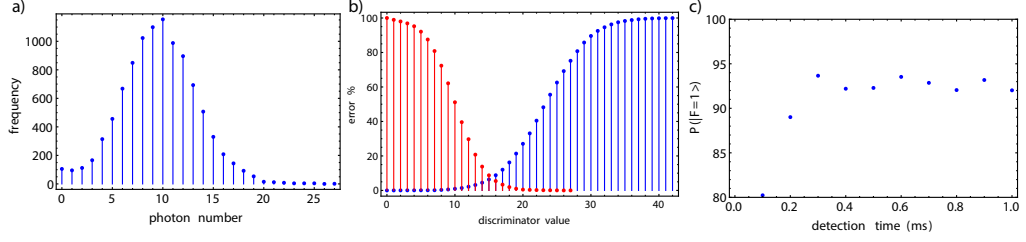


Figure 2.6: State detection of  $^{171}\text{Yb}^+$  ions. **(a)** State detection of a  $^{171}\text{Yb}^+$  ion after optical pumping to  $|0\rangle$  followed by a resonant  $\pi$  microwave rotation on the  $|0\rangle \rightarrow |1\rangle$  transition to prepare the state  $|1\rangle$ . The histogram shows the distribution of the number of photons detected in  $300\ \mu\text{s}$ . The  $|1\rangle$  state detection fidelity in the figure is 0.98. **(b)** Error associated with detecting one and two ions in the  $|1\rangle$  state. The red data shows the probability the  $|10\rangle$  state is correctly identified as a function of discriminator value. The blue data shows the probability the  $|11\rangle$  state is misidentified as a function of discriminator value. The error is equal at a discriminator value of 15 if the detection time is  $300\ \mu\text{s}$ . **(c)** Detection fidelity of  $|11\rangle$  as a function of detection time where the discriminator value is optimized to discriminate between  $|11\rangle$  and  $|01\rangle$  with maximum probability.

the rotated state  $|\psi'\rangle$ . The rotation matrix is

$$R(\theta, \phi) = \cos\left(\frac{\theta}{2}\right) \sigma_0 + i \sin\left(\frac{\theta}{2}\right) \cos(\phi) \sigma_x + i \sin\left(\frac{\theta}{2}\right) \sin(\phi) \sigma_y \quad (2.1)$$

where the angle  $\theta$  is the Rabi angle  $\Omega t$ , a product of the Rabi frequency  $\Omega$  and the time the rotation is applied  $t$ . The matrices  $\sigma_i$  are the usual Pauli matrices. The angle  $\phi$  is the phase angle of the applied electromagnetic field. When applying a rotation to a qubit, the phase may be defined to be zero, but all subsequent operations will depend on the phase relationship of the operations to the first rotation. With trapped  $^{171}\text{Yb}^+$  qubits distributed across spatially separated ion trap modules, maintaining the phase relationship of rotations requires the use of a master phase reference that is distributed across all ion trap modules. A system for doing this is shown in Chapter 4.

The qubit can also be manipulated using stimulated raman transitions. The atom can absorb a photon from one laser beam at frequency  $\omega$  and undergo stimulate emission in to the other laser beam at frequency  $\omega \pm \omega_{ij}$  where  $\omega_{ij}$  is the energy level difference between qubit state  $|i\rangle$  and state  $|j\rangle$ . The laser is detuned from an excited state by an amount  $\Delta$  where the excited state population is negligible, making the three-level “ $\lambda$ -system” behave like a two level system between qubit state  $|i\rangle$  and state  $|j\rangle$ . The Raman transitions in this thesis were carried out with a mode-locked pulsed laser, but the resulting frequency comb may be treated like a collection of coherent, continuous wave lasers. A complete treatment of  $^{171}\text{Yb}^+$  interactions with mode-locked pulsed lasers can be found in [27].

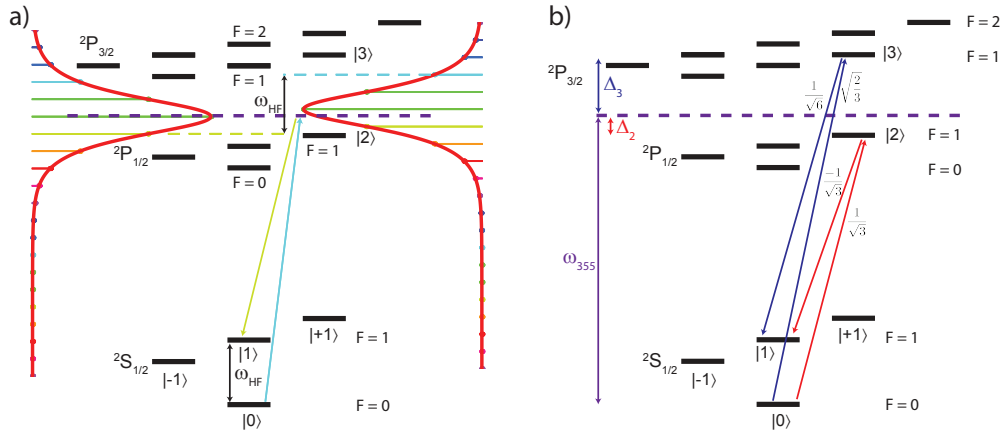


Figure 2.7: Two photon Raman transitions in  $^{171}\text{Yb}^+$ . **(a)** A mode-locked, tripled Nd:YVO<sub>4</sub> laser at 355 nm can be used to drive Raman transitions between qubit states  $|0\rangle$  and  $|1\rangle$  and can also be used to address the Stokes and anti-Stokes transitions. Transitions between the qubits states occur if the frequency difference of a pair of comb teeth match  $\omega_{HF}$ . The 355 nm laser couples to the  $P_{1/2}$  and  $P_{3/2}$  levels, resulting in constructive interference of the Rabi frequency and destructive interference of the differential Stark shift [28]. **(b)** Coupling coefficients defined by Eqn. 2.3.

The interaction Hamiltonian for an atom at position  $x = 0$  interacting with a laser pulse with time dependent envelope  $E(t)$  at frequency  $\omega$  with complex polar-

ization vector  $\epsilon$  is an electric dipole interaction [29]

$$H_{int} = -\mu \cdot \left( \frac{1}{2} \hat{\epsilon} E(t) e^{-i(\omega t + \phi_L)} + \frac{1}{2} \hat{\epsilon}^* E(t) e^{i(\omega t + \phi_L)} \right) \quad (2.2)$$

where the atom has electric dipole moment  $\mu$ . If the laser is purely  $\sigma^+$  polarized, it will induce stimulated Raman transitions between the states  $|0\rangle$  and  $|1\rangle$  through the  $|F, m_F\rangle = |1, 1\rangle \equiv |2\rangle$  level of the  $^2P_{1/2}$  excited state and the  $|1, 1\rangle$  level of the  $^2P_{3/2}$  excited state, denoted  $|3\rangle$ . (see Fig. 2.7). The single photon Rabi frequency of this process is simplifies to [27]

$$g_{ij} = \gamma \sqrt{\frac{I}{2I_{sat}}} \sqrt{2J' + 1} C_{ij} e^{i\phi_L} \quad (2.3)$$

where  $\phi_L$  is the optical phase of the laser field,  $I/I_{sat}$  is the saturation parameter,  $C_{ij}$  is the coupling coefficient for the single photon Rabi frequency between the states  $i$  and  $j$  (see Fig. 2.7b), and  $\gamma$  is the linewidth of the excited state. The Raman Rabi frequency for a transition between  $|0\rangle$  and  $|1\rangle$  is

$$\begin{aligned} \Omega &= \frac{g_{02}^* g_{12}}{2\Delta_2} + \frac{g_{03}^* g_{03}}{2\Delta_3} \\ &= \frac{\gamma_2^2}{2\Delta_2} \frac{I_2}{2I_{sat2}} C_{02} C_{12} + \frac{\gamma_3^2}{2\Delta_3} \frac{I_3}{2I_{sat3}} C_{03} C_{13} \end{aligned} \quad (2.4)$$

with detuning from each level  $\Delta_i = \omega_L - \omega_i$ . In the above equation, the coefficients  $C_{02} C_{12} = 1/\sqrt{3} \cdot -1/\sqrt{3}$  and  $C_{03} C_{13} = \sqrt{2/3} \cdot 1\sqrt{6}$ . Note that since the linewidth of the atom is proportional to  $\omega^3$  and the saturation intensity is proportional to  $\gamma\omega^3 \propto$

$\omega^6$ , the ratio  $\gamma_i^2/I_{sat,i}$  is independent of the dipole transition. If we assume both Raman laser fields have the same intensity, the Raman Rabi frequency simplifies to

$$\Omega = \frac{\gamma^2 s}{12} \left( \frac{-1}{\Delta_2} + \frac{1}{\Delta_3} \right) \quad (2.5)$$

where the linewidth  $\gamma$  and the saturation parameter  $s = I/I_{sat}$  both refer to either to  $P_{1/2}$  or the  $P_{3/2}$  level. Note that for Raman transitions at 355 nm in  $^{171}\text{Yb}^+$ , the detuning  $\Delta_2$  is positive ( $\sim +33$  THz) while the detuning  $\Delta_3$  is negative ( $\sim -66$  THz), resulting in constructive interference for the Rabi frequency. If a 532 nm laser is used, both detunings are positive, resulting in destructive interference of the Rabi frequency. The ratio of the Rabi frequencies  $\Omega_{355}/\Omega_{532} = 39$  assuming equal intensities from both laser fields. If 1064 nm light is used, the ratio of the Rabi frequencies  $\Omega_{355}/\Omega_{1064} = 208$ . In the far detuned limit where  $\Delta_3 = \Delta_2 - \omega_{FS}$  where  $\omega_{FS}$  is the fine structure splitting of the  $P_{1/2}$  and  $P_{3/2}$  states, the Raman Rabi frequency is

$$\Omega \approx \frac{\gamma^2 s \omega_{FS}}{12 \Delta_2^2} \quad (2.6)$$

and the Rabi frequency falls off as  $1/\Delta^2$ .

Raman transitions were observed using 532 nm light from a mode-locked Nd:YVO4 laser by driving  $|1\rangle \leftrightarrow |\pm 1\rangle$  transitions in  $^{171}\text{Yb}^+$ . A  $^{171}\text{Yb}^+$  ion was optically pumped to  $|0\rangle$  and transferred to  $|1\rangle$  by a microwave  $\pi$  pulse. A co-propagating Raman laser beam at 532 nm was directed through an acousto-optic modulator (AOM) where two different frequencies separated by  $\Delta\omega_{\text{Raman}}$  were ap-

plied. After application of the Raman laser, another microwave  $\pi$  pulse was applied to transfer any remaining population in the  $|1\rangle$  state back to  $|0\rangle$  followed by state detection to discriminate between population in the  $F = 1$  manifold and  $|0\rangle$ . A Raman spectrum of the  $|1\rangle \leftrightarrow |\pm 1\rangle$  transitions is shown in Fig. 2.8a. There are two peaks owing to the higher order corrections to the Zeeman shift of  $\sim 10$  kHz at an applied field of  $\sim 5.4$  Gauss. Fig. 2.8b shows Rabi flopping on one of the transitions. A Rabi of frequency of 5 kHz was achieved with  $\sim 300$  mW average power focused down to a waist of  $\sim 30$   $\mu\text{m}$  with a linear combination of  $\sigma^\pm$  and  $\pi$  polarization, consistent with the known laser detuning.

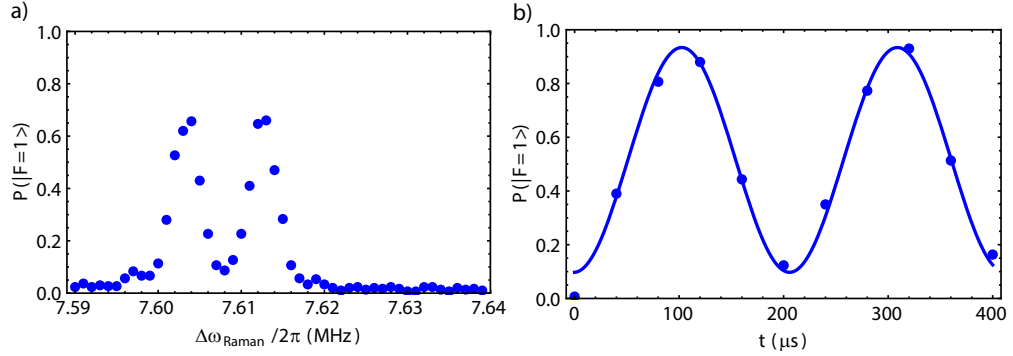


Figure 2.8: Raman transitions with a mode locked 532 nm laser. After optically pumping to  $|0\rangle$ , a microwave  $\pi$  pulse prepares the state  $|1\rangle$ . Copropagating Raman lasers with beatnote  $\Delta\omega/2\pi$  at 532 nm drive transitions between  $|0\rangle \leftrightarrow |1, \pm 1\rangle$  states. The two transitions are at different frequencies due to the non-linear Zeeman effect. Any remaining population in  $|1\rangle$  is transferred back to  $|0\rangle$  and state detection is performed. **(b)** Rabi flopping on a Zeeman transition. A Rabi frequency of  $\sim 5$  kHz was observed with  $\sim 300$  mW of average power focused down to a  $\sim 30$  micron waist. If 1064 nm light was used with equal intensity, the observed Rabi frequency would be approximately 1 kHz.

## Chapter 3: **Photon entanglement of remote qubits**

Cloning an unknown quantum state is forbidden by unitary evolution [30], so quantum networks rely on teleportation as a means to transmit quantum information over long distances [31]. Teleportation proceeds by creating entanglement between two quantum systems, one system prepared the specific superposition state  $\alpha|0\rangle + \beta|1\rangle$  while the second is prepared in a simple superposition state like  $|0\rangle + |1\rangle$ . After entangling the two systems, the first system is measured. The second system is rotated depending on the outcome of the measurement of the first system. The state of the second system is  $\alpha|0\rangle + \beta|1\rangle$ , thus teleporting the quantum state.

In classical communication networks, attenuation of information is overcome by the use of repeaters; information is measured, amplified, and re-transmitted. Quantum communication networks also suffer from attenuation of quantum information; single photons cannot be sent over arbitrary distances. In addition, the quantum state of single photons cannot be measured if entanglement between the photon and its parent qubit is to be maintained. However, like their classical counterpart, quantum repeaters may be used to extend the distance of a quantum network. Long distance communication may be broken up over shorter distances between modules with quantum memories. Entanglement between modules may be accom-

plished in parallel using photon interference, and entanglement swapping in each node can extend the distance between entangled systems [32, 33].

Entanglement over large distances involving many particles has many potential uses such as testing the non-locality of quantum mechanics [34], giving insight in to delayed choice experiments [35, 36], and even the creation of secure, distributed clocks [37]. There are many proposals for constructing quantum networks [38–41], but useful quantum networks have the commonality that the photons serve as means to generate entanglement between remote quantum memories with long coherence times.

Optical photons are natural carriers of quantum information as they can traverse large distances in room temperature optical fibers and through the atmosphere [42], and spontaneously emitted photonic degrees of freedom are naturally entangled with their parent qubit (see Fig. 3.1a). Photons have several degrees of freedom that may be entangled with its parent qubit including polarization, frequency, and arrival time, offering a flexible platform depending on the application [43]. Entanglement between emitted photons and qubits has been demonstrated in a wide variety of systems including trapped ions [44], quantum dots [45], nitrogen vacancy (NV) centers in diamond [46], and neutral atoms [47, 48].

Remote entanglement of qubits is typically accomplished by interfering the emitted photons on a beam splitter. By detecting the output states of the beam splitter, the photons can be detected in the Bell state basis, thus projecting the remote qubits into an entangled state. Remote entanglement between distant qubits has also been demonstrated in many systems including ions [49, 50], NV centers [51],



between remote atomic ensembles [52], and between remote neutral atoms [53]. Entanglement between adjacent qubits in the same cavity using photon interference has also been demonstrated [54]. In addition, the interference of non-identical, entangled single photons has been analyzed [55–57] and recently demonstrated [58]. This work has been extended to include the entanglement of distinguishable quantum memories through the interference of distinguishable photons [59], demonstrating the flexibility and utility of photons as an entanglement bus.

Generation of entanglement has lead to the successful demonstration of teleportation of quantum information between proximate qubits [60, 61] and remote qubits such as trapped ions [62, 63], neutral atoms [64, 65], and NV centers [66]. Though it is possible to teleport a quantum state deterministically [60], the crucial remote entanglement generation step is probabilistic due to the finite collection and detection efficiency of single photons. In order to enable quantum repeater networks and distributed information processing, the remote entanglement generation rate should be as fast as possible compared to the coherence time of the qubits or the remote entangled state coherence time. In order to operate a scalable quantum network at fault tolerant levels, even with perfect gates, the resource requirements depend on the ratio of the mean remote entanglement generation time  $\tau_E$  and the coherence time  $\tau_D$ . The resource scaling is super-exponential:  $(\tau_E/\tau_D)^{\tau_E/\tau_D}$  [17]. The first experiment to realize  $\tau_E/\tau_D < 1$  is one of the primary results of this thesis [20].

This chapter is organized as follows. Generating and measuring entanglement between a trapped  $^{171}\text{Yb}^+$  ion and photon polarization is discussed followed by prac-

tical considerations for aligning an interferometer for entangled photon interference on a beam splitter. The physics of photon interference on a beam splitter is reviewed, including the interference of distinguishable photons. Data showing fast entanglement between remote  $^{171}\text{Yb}^+$  ions is shown where the average remote entanglement rate is  $4.5 \text{ sec}^{-1}$  and the remote entangled state coherence time is 1.12 sec, resulting in  $\tau_E/\tau_D = 0.2$ . Finally, experiments using interference with photons whose frequency difference more than the photon linewidth are shown with the final result that distinguishable photons can be used to create high-fidelity entanglement without sacrificing entanglement rate.

### 3.1 Atom Photon Entanglement

An atom prepared in a pure state in its ground state manifold may be excited with an ultrafast laser pulse with duration much shorter than the excited state lifetime  $\tau$ , typically of order 10 ns for dipole allowed transitions of single atoms. The atomic excited state will undergo spontaneous emission and emit a single photon, and some degrees of freedom of the photon may be entangled with the resulting ground states to which the atom decays. The general form for the atom-photon state is

$$|\psi\rangle = \sum_{i,j,\Delta m} \alpha_{ij} |S_i\rangle |\gamma_{\Delta m}, \omega_j\rangle \quad (3.1)$$

where the sum is over the excited states  $j$  of the atom before emitting a photon of frequency  $\omega_j$  and returning the ground state  $|S_i\rangle$ . The photon state  $|\gamma_{\Delta m}, \omega_j\rangle$  depends on the decay channel of the radiation. For a  $\Delta m = 0$  transition, the

polarization state of the photon is  $-\sin\theta|\hat{\theta}\rangle$  and for a  $\Delta m = \pm 1$  transition, the polarization state of the photon is  $e^{\pm i\phi}(\cos\theta|\hat{\theta}\rangle \pm i|\hat{\phi}\rangle)$ . The angles  $\theta$  and  $\phi$  are the polar and azimuthal angles with respect to the quantization axis with unit vectors  $|\hat{\theta}\rangle$  and  $|\hat{\phi}\rangle$  [67]. If the atom and spontaneously emitted photon states can be measured in multiple bases, entanglement between the atom and the photon can be verified.

For example, Fig. 3.1a shows a  $^{171}\text{Yb}^+$  ion energy level diagram. If an ion is prepared in the  $|F, m_F\rangle = |0, 0\rangle \equiv |0\rangle$  of the  $S_{1/2}$  manifold and excited to the  $|1, 0\rangle$  state of the  $P_{1/2}$  manifold, the atom can decay to the states  $|1, -1\rangle \equiv |-1\rangle$ ,  $|1, -1\rangle \equiv |+1\rangle$ , and  $|0\rangle$  with equal probability. The resulting state has entanglement between the atom state and the photon polarization

$$|\psi\rangle = \frac{1}{\sqrt{3}}(-|\sigma^+\rangle|-1\rangle + |\sigma^-\rangle|+1\rangle + |\pi\rangle|0\rangle). \quad (3.2)$$

Tracing over the state of the photon results in classical mixed atomic state, so detecting the state of the photon and the atom is critical for probing entanglement. Detection of the photon is inherently probabilistic because of both the finite photon collection solid angle of the atom radiation field and the use of single photon detectors with quantum efficiency less than unity. It is possible to increase the photon collection efficiency by putting the atom in a cavity. However, in order to generate deterministic entanglement at fault-tolerant levels, the photon collection efficiency and the single photon detector efficiency will have to meet fault tolerant thresholds, typically higher than 0.9999 [68, 69].

Entanglement between the photon and its parent atom can be verified through

post selection upon detecting a single photon in two orthogonal photon bases and two orthogonal atom bases. Equation 3.2 has three terms, but the photon polarization emission pattern is not isotropic as shown in Fig. 3.2b. If the photon collection is directed along the quantization axis,  $\sigma^\pm$  polarization is more likely to be detected than  $\pi$  polarization. As the numerical aperture of the collection optics increases along the quantization axis, more  $\pi$  polarized light will be collected. As viewed along this axis,  $\pi$  polarized light has a toroidal intensity pattern (see Fig. 3.1c) with radial electric field polarization. This electric field mode will not couple to the  $\text{TEM}_{00}$  mode of a single mode optical fiber if the fiber is mutually aligned to the optical axis and to the quantization axis set by an externally applied magnetic field [70].

The ability of a single mode fiber to filter out  $\pi$  polarized light can be directly observed using a trapped  $^{171}\text{Yb}^+$  ion. An ultrafast laser pulse excites an ion prepared in  $|0\rangle$  to the  $|1,0\rangle$  state in the  $P_{1/2}$  manifold. The atom spontaneously decays to the states  $|-1\rangle$ ,  $|+1\rangle$ , and  $|0\rangle$  with probability  $1/3$  for each state. Performing state detection after spontaneous emission of a single photon without detecting the state of the photon results in detecting the atom in the  $F = 1$  manifold of the  $S_{1/2}$  ground state with probability  $2/3$ . If a resonant microwave pulse is performed on the  $|0\rangle$  to  $|1\rangle$  transition before state detection, Rabi flopping with contrast  $1/3$  should be observed, and the probability of detecting the atom in the  $F = 1$  state should oscillate between  $2/3$  and  $1$ . This behavior is shown in the red data in Fig. 3.2. The data drops below  $2/3$  because of the non-unit excitation probability of the ultrafast laser excitation pulse. Instead of performing a microwave pulse of variable

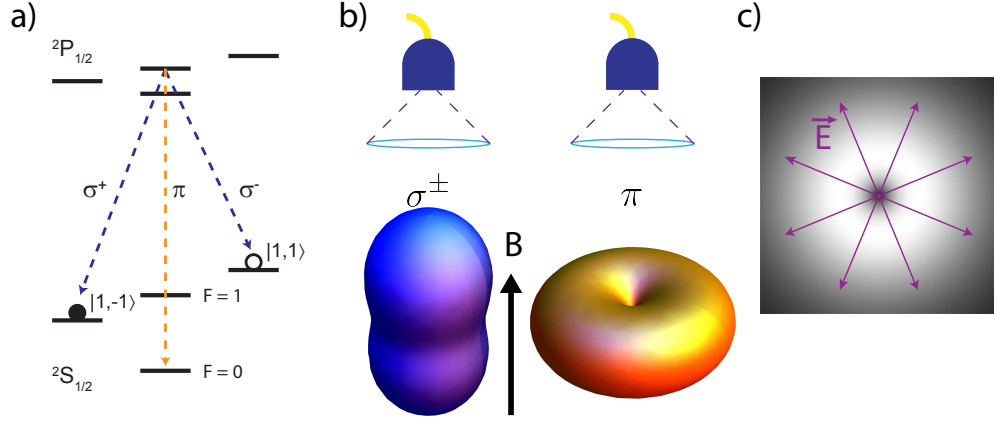


Figure 3.1: Fiber coupling single ions. **(a)** Energy level diagram of  $^{171}\text{Yb}^+$  ion. After optically pumping the ion to the  $|F, m_F\rangle = |0, 0\rangle$  state, an ultrafast laser pulse excites the ion to the  $|1, 0\rangle$  excited state in the  $P_{1/2}$  manifold. The atom undergoes spontaneous emission to  $|1, \pm 1\rangle$  levels by emitting a  $\sigma^\pm$  single photon and back to the  $|0, 0\rangle$  level by emitting a  $\pi$  polarized single photon. **(b)** If the magnetic field that defines the quantization axis points at a single mode fiber, the  $\sigma^\pm$  modes of light are directed toward and away from the fiber in a “peanut” shape. The  $\pi$  polarized light is toroidal shaped with a node along the optical axis. The light from the atom is collected with a high numerical aperture microscope that subtends approximately 10% of the total solid angle. **(c)** As the solid angle of the microscope objective increases, the power incident on the single mode fiber from all three photon modes increases. The intensity map shows the spatial distribution of the  $\pi$  polarized light on the fiber face. However, since the electric field is radially polarized, the  $\pi$ -polarized mode does not couple to a single mode fiber with cylindrical symmetry. The photon collection solid angle may be increased without mixing  $\sigma^\pm$  and  $\pi$  polarization in the optical fiber. The single mode fibers can be strained to map  $|\sigma^+\rangle \rightarrow |H\rangle$  and  $|\sigma^-\rangle \rightarrow |V\rangle$ .

duration after all ultrafast atomic excitations, the microwave pulse may be performed only after detecting a single photon that traverses a single mode optical fiber. The blue data shows the atom is in the  $F = 1$  state with high probability regardless of the polarization of the detected photon for variable application of the resonant microwave field. The detected photons are thus not  $\pi$  polarized and not correlated with the  $|0\rangle$  atomic state after the optical fiber. The amplitude of the oscillation of the blue data is  $< 1\%$ .

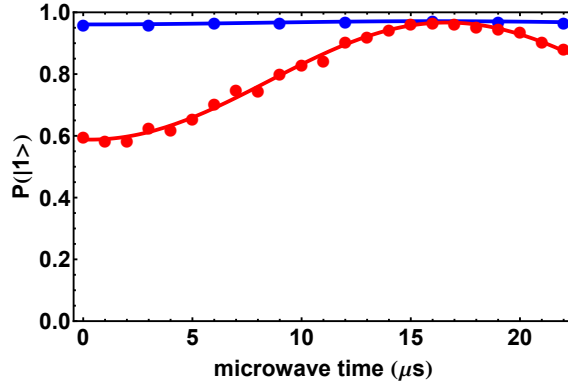


Figure 3.2: Filtering  $\pi$  polarized light with a single mode optical fiber. Excited  $^{171}\text{Yb}^+$  ions decay by emitting  $\sigma^\pm$  and  $\pi$  polarized photons (see Fig. 3.1a) with probability  $2/3$  and  $1/3$  respectively. If the ion is excited with unit probability, undergoes spontaneous emission, and subjected to a resonant microwave pulse on the  $|0\rangle$  to  $|1\rangle$  transition with variable duration, the probability the ion is in the  $F = 1$  manifold will oscillate between  $2/3$  and  $1$ . The red data and fit show this phenomenon clearly. If the microwave pulse is conditioned on detecting a photon of any polarization that passes through an optical fiber and is detected by a PMT, the atom is detected in the  $F = 1$  state with near unit probability. The optical fiber therefore filters out  $\pi$  polarized photons.

Entanglement between the photon  $\sigma^\pm$  polarization and the atom  $|\pm 1\rangle$  states may be probed with rotations of the photon polarization and the atom state. Correlations between the atom and the photon polarization state can be measured by performing a microwave  $\pi$  pulse on either the  $|-1\rangle \rightarrow |0\rangle$  or  $|+1\rangle \rightarrow |0\rangle$  tran-

sition after detecting the photon polarization in one basis. The phase coherence of the entangled state can be probed by rotating the photon polarization by  $\pi/4$  and measuring the photon in the  $|H\rangle + |V\rangle$  and  $|H\rangle - |V\rangle$  bases. After detecting the state of the photon, the qubit is manipulated with a microwave  $\pi$  pulse on the  $|-1\rangle \leftrightarrow |0\rangle$  transition followed by a  $\pi/2$  pulse with a phase shift  $\phi$  relative to the first microwave pulse. The probability of detecting the qubit in the state  $F = 1$  state is proportional to  $\cos(\Delta\omega\Delta t' + (\phi_1 - \phi_2) + \phi_D)$  where the phase difference between the two microwave pulses is  $\phi_1 - \phi_2$ ,  $\Delta\omega\Delta t'$  is the free evolution of the atom after the photon is detected at the frequency difference of the  $|-1\rangle$  and  $|+1\rangle$  states, and  $\phi_D$  is zero or  $\pi/2$ , depending on if the photon is detected in the  $|H\rangle \pm |V\rangle$  basis. Note that since the two microwave pulses are at different frequencies and the single photon is detected at random times, the phase difference between the two oscillators needs to be reset upon detecting the photon. A simple way to ensure this is to use a microwave oscillator mixed with an arbitrary waveform generator.

The results of these measurements can be used to place a lower bound on the atom-photon polarization entanglement [44, 67]. The results presented here give  $F \geq 0.93$ . The infidelity of the microwave pulses and state detection along with imperfect polarization filtering of the photons in the interferometer do not account for the observed infidelity. The measured atom-photon polarization correlations do not depend on phase stability of the entangled state, and these correlations were unexpectedly low ( $\sim 0.95$ ). Spatially inhomogeneous birefringence from stress on the vacuum viewport glass or misalignment of the photon collection axis orthogonal to the vacuum viewport glass may account for mixing of the polarization modes of

the photon. This is not a fundamental source of decoherence and could be corrected with a phase mask.

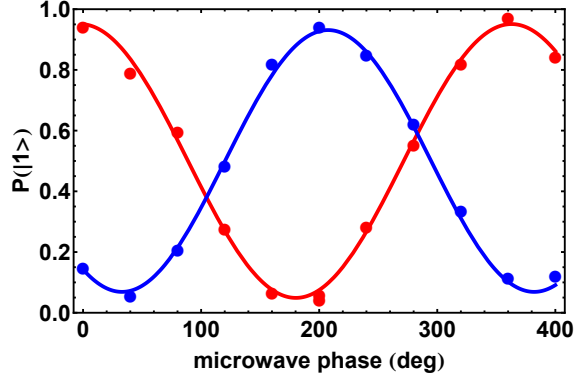


Figure 3.3: Ion photon polarization entanglement. A  $\lambda/2$  waveplate is inserted before the thin film polarizers as shown in Fig. 3.4. The waveplate rotates the horizontal and vertical polarization by 45 degrees so that measurement of a photon after the thin film polarizers is in the diagonal and anti-diagonal photon basis. Measurement of a photon projects the ion in to the state  $| -1 \rangle + | +1 \rangle$  and  $| -1 \rangle - | +1 \rangle$  respectively. A microwave  $\pi$  pulse moves population from the  $| -1 \rangle$  to the  $| 0 \rangle$  state, followed by a second microwave  $\pi/2$  rotation with variable phase  $\phi$  on the  $| 0 \rangle$  to  $| +1 \rangle$  transition. The interference of the quantum state with itself gives an oscillatory dependence on the probability of detecting the atom in the  $F = 1$  state that depends on the phase difference of the two microwave pulses. The contrast of the data shown in the plot combined with measurements without the second microwave pulse and without rotating the photon polarization bound the fidelity of the entanglement between the atom and the photon polarization.

### 3.2 Practical interferometer alignment considerations

A diagram of the interferometer used in the experiments in this thesis is shown in Fig. 3.4. Light from each atom is directed on to a 50/50 beam splitter. The incidence angle on the beam splitter is kept shallow. At large angles, beam splitters are not equal 50/50 beam splitters for all polarizations for ultraviolet light. After the photons interfere on the beam splitter, the photon polarization is sorted using thin film polarizers, denoted TFP1 and TFP2 in the figure. These polarizers transmit



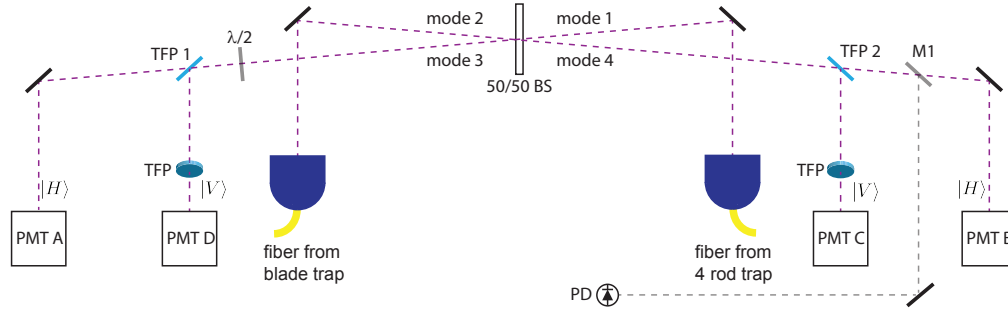


Figure 3.4: Single photon interferometer. Single photons entangled with its parent ion from a four blade and four rod ion trap are mode matched on a beam splitter where they interfere. The photons are converted to the horizontal and vertical polarization basis by straining the optical fibers. Thin film polarizers TFP 1 and TFP 2 are attached to motorized flip mounts. These thin film polarizers sort the photon polarization by reflecting vertical polarization and transmitting horizontal polarization. An additional thin film polarizer is added to each  $|V\rangle$  channel to filter out the small amount of  $|H\rangle$  photons reflected from TFP 1 and 2. A half wave plate  $\lambda/2$  is attached to a motorized flip mount for characterizing ion photon polarization entanglement. The mirror M1 may be inserted to direct beam splitter output port 4 to a photodiode PD for spatial mode matching on the beam splitter. The  $|\psi^+\rangle$  photonic Bell state results in coincidence measurement of single photons by PMTs A and D or C and B. The  $|\psi^-\rangle$  photonic Bell state results in coincidence measurement of single photons by PMTs A and C or D and B. If the photons are identical and the single photons are perfectly mode matched on the beam splitter, photon coincidence measurements by PMTs A and B or D and C should not occur.

polarization in the plane of the page ( $|H\rangle$ ) and reflect vertical polarization ( $|V\rangle$ ). The transmitted horizontal polarization is well polarized, but the reflected vertical polarization has a small horizontal component. A second thin film polarizer is used to purify the vertical polarization channel.

Alignment of thin film polarizers must be set consistently in the interferometer. After placing TFP1, TFP2 and the vertical channel thin film polarizers, all TFPs should be set self consistently; rotating the polarization of the light exiting each optical fiber should produce high extinction ratios between polarization channels. After mutual alignment of all polarization detection channels, the polarization axes of the interferometer are fixed. Any difference between the atom quantization axis and the interferometer polarization axis can be corrected with fiber strain or wave plates while monitoring state dependent detection of the atom as a function of detected photon polarization.

Optimal fiber coupling is achieved by aligning the optical axis of the collection optics perpendicular to the vacuum viewport. Aligning the pitch and yaw of the collection optics can be accomplished in a variety of ways such as the use of an autocollimator. After alignment of the collection optics is complete, the magnetic field must be aligned to the quantization axis. The field may be grossly aligned by adjustment of the magnetic field perpendicular to the optical axis and minimizing the Zeeman shift of the atom. Final alignment of the quantization axis and the fiber strain axis is accomplished directly by measuring the correlation of the atom state with the photon polarization state.

### 3.2.1 Micromotion compensation

Micromotion compensation along the optical axis is crucial for high fidelity interference of the photons emitted by the atoms. Micromotion alters the photon spectrum at the frequency used for RF confinement, and different ion traps typically have different RF drives. In addition, differential micromotion amplitude between modules alters the photon spectral density. Compensation of micromotion along the optical axis necessitates the use of a laser along the photon collection axis. If laser light is directed through the low NA, free space collection optics (See Fig. 2.1), the laser light can saturate the single photon detectors in the interferometer, prohibiting detection of photons from the atom. Reflections off of surfaces in the low NA objective were directed back in to the free space PMT and camera, preventing measurement of the atom. Light can instead be directed off of a 50/50 beam splitter through the high NA objective as shown in Fig. 3.5. The alignment of the light from the micromotion fiber to the atom is accomplished by imaging the atom and the light from the fiber through the low NA free space collection optics on to an intensified CCD camera. The 50/50 BS also displaces the scattered light from the atom relative to the fiber to the interferometer. The interferometer fiber can be re-aligned to the atom by sending light back through the interferometer fiber where it is imaged by the high NA objective on the ion. This is re-imaged by the low NA free space collection optics on an intensified CCD camera. Simultaneous visualization of light exiting the fiber to the interferometer, the micromotion fiber, and light scattered from the atom on a CCD camera facilitates easy alignment of the micromotion optics. The

light scattered from the atom is collected by the high NA objective and is focused through the 50/50 BS into the fiber leading to the interferometer. Reflections of the light from the micromotion fiber on the glass surfaces of the imaging optics do not couple well to the small fiber core. Micromotion may be minimized by correlating the photon arrival time of scattered light with the ion trap RF drive phase [71].

### 3.2.2 Interferometer mode matching

Spatial alignment of the interferometer mode is crucial for entangled state fidelity; the entangled state fidelity is equal to  $1/(2 - V^2)$  where  $V$  is the interferometer visibility [24]. Currently, there are no commercially available 50/50 fiber beam splitters available at 369 nm, so spatial mode matching must be done in free space. Spatial overlap may be accomplished by locking a resonant laser to an atomic source and fiber coupling the laser light in to both interferometer inputs. The fiber strain should be set to give a well defined polarization and may be easily verified by observing the transmission and reflection of light from the thin film polarizers TFP1 and TFP2. With the polarization set, the mirror M1 may be inserted and the optical power exiting each fiber can be equalized by measuring the light on the photodiode PD. With polarization and power equalized, the interference fringes of the light may be observed when the fiber modes overlap on the beam splitter. It is useful to attach the tilt adjustment of the optical fiber input stage (end of a fiber not shown in Fig. 3.4) to a piezoelectric material driven by a high voltage sawtooth wave. Time dependent interference fringes at the piezoelectric drive frequency may

be observed, and the interferometer visibility may be maximized by adjusting the overlap of the laser modes on the beam splitter. The interferometer visibility was aligned to  $>0.97$ , and misalignment of the spatial mode overlap to  $V \sim 0.95$  was observed on time scales of order one day. This imperfect spatial mode matching contributes  $\sim 5\text{-}9\%$  to the infidelity of the remote atom entangled state.

### 3.2.3 Setting fiber strain

An optical fiber may be strained to induce birefringence. This feature of single mode, non polarization maintaining fibers allows for control over the polarization of a single photon exiting the fiber and entering the interferometer. The fiber strain can be set individually for each ion trap, and the fiber strain can induce a phase on the atom-photon polarization entangled state. After photon interference, the fiber strain phase appears on the remote atom entangled state. When performing experiments to entangle remote atoms, the fiber strain phase must be set consistently while acquiring remote entanglement data. The phase imparted from fiber strain is observed to drift on slow, presumably thermal, time-scales.

Fiber strain can be modeled by linear optics as a quarter-wave plate followed by a half wave plate followed by a quarter wave plate. This model allows any input photon polarization to be converted to any output polarization. A quarter and half

wave plate at angle  $\theta$  with respect to vertical can be modeled with matrices

$$\begin{aligned}\text{HWP}(\theta) &= \begin{pmatrix} \cos 2\theta & \sin 2\theta \\ \sin 2\theta & -\cos 2\theta \end{pmatrix} \\ \text{QWP}(\theta) &= \begin{pmatrix} \cos^2 \theta + i \sin^2 \theta & (1-i) \sin \theta \cos \theta \\ (1-i) \sin \theta \cos \theta & \sin^2 \theta + i \cos^2 \theta \end{pmatrix}\end{aligned}\quad (3.3)$$

and the photon polarization states can be modeled with the Jones vectors

$$h = \begin{pmatrix} 1 \\ 0 \end{pmatrix} \quad v = \begin{pmatrix} 0 \\ 1 \end{pmatrix} . \quad (3.4)$$

The right circular, left circular, diagonal and anti-diagonal photon polarizations expressed in the  $\{h, v\}$  basis are  $r = h - iv$ ,  $\ell = h + iv$ ,  $d = h + v$ , and  $a = h - v$ . If right circular polarization is put in to an optical fiber, multiple fiber strain settings can map the photon polarization to vertical polarization, but with a different phase values

$$\begin{aligned}\text{QWP}(0)\text{HWP}(0)\text{QWP}(\pi/4)r &= -e^{i\pi/4}v \\ \text{QWP}(0)\text{HWP}(\pi/2)\text{QWP}(\pi/4)r &= e^{i\pi/4}v \\ \text{QWP}(0)\text{HWP}(0)\text{QWP}(3\pi/4)r &= e^{i\pi/4}v.\end{aligned}\quad (3.5)$$

If this phase difference is not accounted for while correcting fiber strain, the phase of atom-photon entangled state will change, affecting the phase of the remote atom

entangled state. Correcting for small drifts in fiber birefringence while acquiring remote entanglement data can result in averaging over the fiber strain phase.

The phase of the atom-photon entanglement may be set by measuring the polarization of the well polarized, test laser beam in two, non-orthogonal bases. If the desired fiber strain is  $\text{QWP}(0)\text{HWP}(0)\text{QWP}(\pi/4)$ , the fiber will map right and left circular polarization to  $-e^{i\pi/4}v$  and  $e^{i\pi/4}h$  respectively. By changing the input polarization of the test beam to  $h$  or  $v$ , the fiber strain will map the polarization to  $e^{i\pi/4}a$  and  $e^{3\pi/4}d$  respectively. Inserting a half wave plate after the beam splitter as shown in Fig. 3.4 rotates diagonal and anti-diagonal polarization to the  $\{h, v\}$  basis. Setting each ion trap module to map left or right polarization and horizontal or vertical polarization (with a half wave plate inserted) to the same photon detectors from each ion trap module ensures consistent atom-photon entangled state phases across different modules.

### 3.3 Photon interference on a beam splitter

Photon interference on a beam splitter is the important ingredient in entangling remote qubits. In 1987, Hong, Ou, and Mandel observed when identical photons interfere on a beam splitter, both photons exit the same port of a 50/50 beam-splitter. The detection of “antibunched” photons, photons exiting different ports of a beam splitter, are suppressed by quantum interference. The bunching of identical photons through a beam splitter is referred to as Hong-Ou-Mandel interference. Figure 3.6 shows a 50/50 beam splitter with two input (mode 1 and mode 2) and two

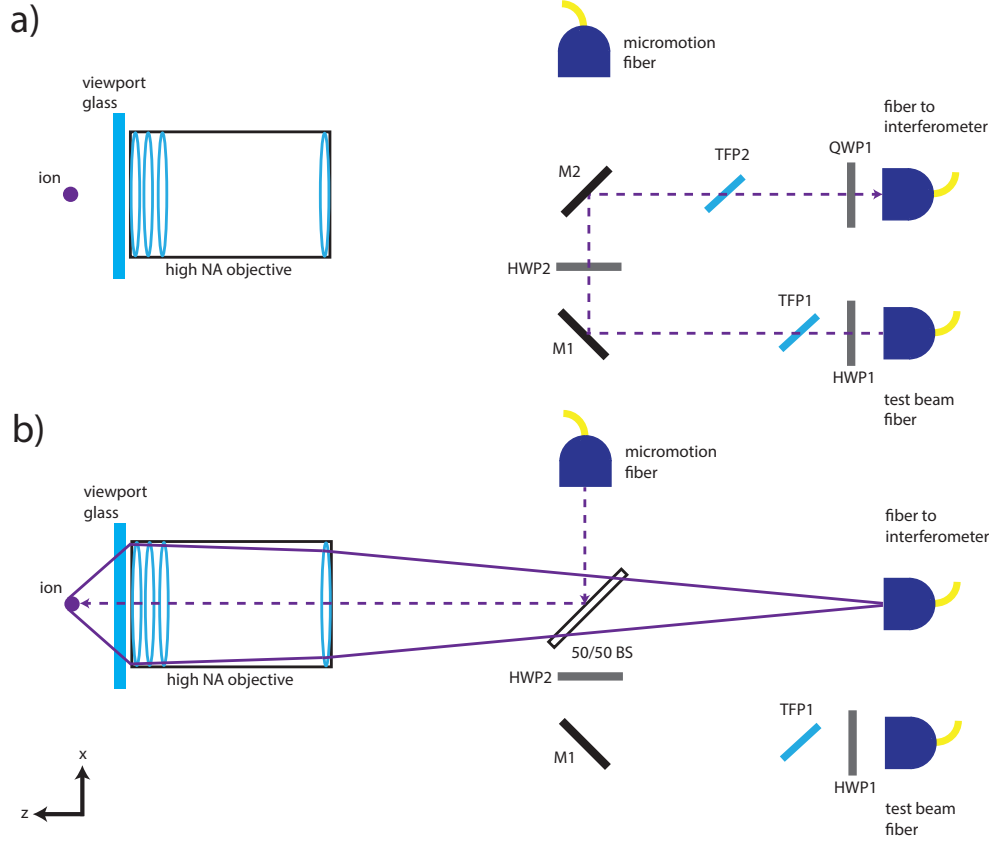


Figure 3.5: Fiber strain and micromotion compensation optics. **(a)** Fiber strain optics. A well polarized, test laser beam is used to set the fiber strain in the lab frame. The half waveplate HWP1 is used to adjust the amount of horizontally polarized light ( $x$  direction in the figure) passing through thin film polarizer TFP1. Mirrors M1 and M2 direct the test beam toward the fiber leading to the interferometer. TFP2 is set by adjusting its angle in combination with HWP2 as a second stage polarization purification. The quarter wave plate QWP1 is set to turn the polarized light into to circular light. The fiber may be strained to map this polarization to one set of PMT detectors in the interferometer (see Fig. 3.4). QWP1 was mounted on a magnetic mount so it can be removed, and the halfwave plate in the interferometer may be flipped in to beam path to measure the light in the diagonal and antidiagonal basis to set the entangled state phase. **(b)** Micromotion compensation optics along photon collection axis. M2, TFP2 and QWP1, all attached to magnetic or flip mounts, are removed from the beam path. A 50/50 beam splitter is inserted on the M2 magnetic mount. The fiber to the interferometer is displaced along  $x$  to compensate for the displacement in the optical path due to the 50/50 BS. Light from the micromotion fiber is aligned on to the atom with the magnetic field is rotated orthogonal to the  $z$  direction to avoid coherent population trapping [23]. The scattered atom light is collected by the high NA objective and imaged through the BS in to the fiber to the interferometer. The fluorescence may be correlated with the RF phase to measure and minimize micromotion.



output modes (mode 3 and mode 4). We consider the case where a single, identical photon enters each input mode 1 and 2. The operation of a beam splitter is

$$a_3^\dagger = a_1^\dagger - a_2^\dagger \quad a_4^\dagger = a_1^\dagger + a_2^\dagger \quad (3.6)$$

where the minus sign comes from a photon in mode 2 reflecting off of a surface where the index of refraction changes from low to high [72]. Written in terms of the incoming photons in mode 1 and 2 as a function of the outgoing photons in mode 3 and 4, the field operators are

$$a_1^\dagger = a_3^\dagger + a_4^\dagger \quad a_2^\dagger = -a_3^\dagger + a_4^\dagger. \quad (3.7)$$

Photon bunching can be seen by considering an identical photon impinging on modes 1 and 2

$$\begin{aligned} |1_1 1_2\rangle &= a_1^\dagger a_2^\dagger |0\rangle \\ &= (a_3^\dagger + a_4^\dagger)(-a_3^\dagger + a_4^\dagger) |0\rangle \\ &= (a_4^\dagger a_4^\dagger - a_3^\dagger a_3^\dagger) |0\rangle \\ &= |0_3 2_4\rangle - |2_3 0_4\rangle \end{aligned} \quad (3.8)$$

The two photons exit the same port with 50/50 probability, but the photons never simultaneously emerge from opposite beam splitter ports. Coincidence measurements of photons exiting different beam splitter ports will be perfectly suppressed

by the interference of the identical photons. Measuring photon bunching (or lack of photon anti-bunching) is a way to test if photons are identical. This analysis makes the assumption that the identical photons are not entangled with any other system, such as an atom. If identical photons are entangled with another system, the identical photons will not exclusively display bunching upon exiting the beam splitter. As will be shown, photon anti-bunching will occur with probability  $1/4$  if the identical photons are perfectly mode matched to a 50/50 beam splitter.

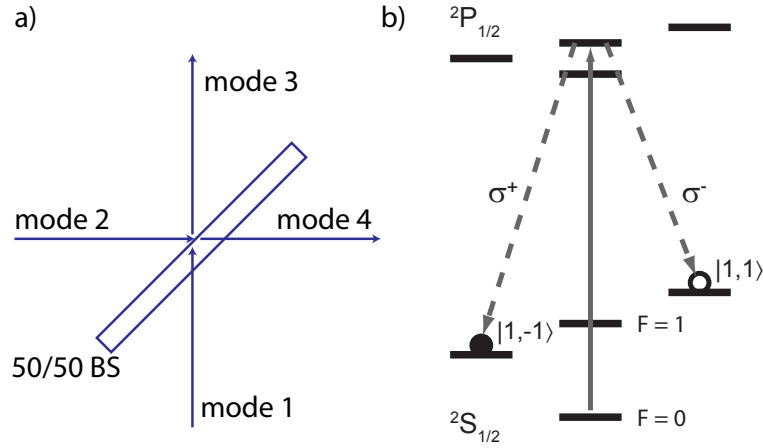


Figure 3.6: Photonic modes on a beam splitter. **(a)** A 50/50, non-polarizing beam splitter has input modes 1 and 2 and output modes 3 and 4. The photons are assumed to reflect off of the glass air interface as shown. Since the index of refraction changes from low to high when a photon is reflected from mode 2 into mode 3, a  $\pi$  phase shift results. **(b)** Excitation and decay of a  $^{171}\text{Yb}^+$  qubit. After spontaneously emitting a photon, the state of the atom is entangled with the polarization state of the photon. This entanglement results in rich behavior when the photons interfere on the beam splitter.

Consider an two atoms undergoing spontaneous decay and each emitting a single photon as is depicted in Fig. 3.6b. The state of the atom 1 and atom 2 is entangled with the polarization state of photon 1 and photon 2. Atom 1 is coupled to beam splitter input port 1 while atom 2 is coupled to beam splitter input port 2.

The photon polarization states are denoted  $|H\rangle = a_i^\dagger|0\rangle$  and  $|V\rangle = b_i^\dagger|0\rangle$  for input ports  $i = 1, 2$ . The joint atom-photon state is

$$\begin{aligned} |\psi_1\psi_2\gamma_1\gamma_2\rangle &= (\alpha|0H\rangle + \beta|1V\rangle)_1 \otimes (\gamma|0H\rangle + \delta|1V\rangle)_2 \\ &= \alpha\gamma|00HH\rangle + \alpha\delta|01HV\rangle + \beta\gamma|10VH\rangle + \beta\delta|11VV\rangle \end{aligned} \quad (3.9)$$

where the kets define the state of qubit 1, the state of qubit 2, the state of photon 1 (entangled with qubit 1), and the state of photon 2 (entangled with atom 2) respectively. This state can be re-arranged in terms of the Bell states of photons, defined by

$$\begin{aligned} |\psi^+\rangle &= |HV\rangle + |VH\rangle & |\phi^+\rangle &= |HH\rangle + |VV\rangle \\ |\psi^-\rangle &= |HV\rangle - |VH\rangle & |\phi^-\rangle &= |HH\rangle - |VV\rangle \end{aligned} \quad (3.10)$$

which results in the joint atom-photon state

$$\begin{aligned} |\psi\rangle &= \alpha\gamma|00\rangle(|\phi^+\rangle + |\phi^-\rangle) + \beta\gamma|10\rangle(|\psi^+\rangle - |\psi^-\rangle) \\ &+ \alpha\delta|01\rangle(|\psi^+\rangle + |\psi^-\rangle) + \beta\delta|11\rangle(|\phi^+\rangle - |\phi^-\rangle) \\ &= |\phi^+\rangle(\alpha\gamma|00\rangle + \beta\delta|11\rangle) + |\phi^-\rangle(\alpha\gamma|00\rangle - \beta\delta|11\rangle) \\ &+ |\psi^+\rangle(\beta\gamma|10\rangle + \alpha\delta|01\rangle) + |\psi^-\rangle(\alpha\delta|01\rangle - \beta\gamma|10\rangle) \end{aligned} \quad (3.11)$$

The photon states impinging on the beam splitter input ports 1 and 2 can be rewritten in terms of the output modes of the beam splitter for both polarizations using

Eqn. 3.7.

$$\begin{aligned}
|\phi^\pm\rangle &= \left(a_1^\dagger a_2^\dagger \pm b_1^\dagger b_2^\dagger\right) |0\rangle \\
&= \left(a_4^\dagger a_4^\dagger - a_3^\dagger a_3^\dagger \pm b_4^\dagger b_4^\dagger \mp b_3^\dagger b_3^\dagger\right) |0\rangle \\
&= |0_3(HH)_4\rangle - |(HH)_3 0_4\rangle \pm |0_3(VV)_4\rangle \mp |(VV)_3 0_4\rangle.
\end{aligned} \tag{3.12}$$

The  $|\phi^\pm\rangle$  photonic Bell states differ only by a minus sign and involve two photons with identical polarizations in the same mode, making detection in the linear  $\{|H\rangle, |V\rangle\}$  basis difficult using detectors without photon number resolution. The  $|\psi^+\rangle$  state also displays photon bunching

$$\begin{aligned}
|\psi^+\rangle &= \left(a_1^\dagger b_2^\dagger + b_1^\dagger a_2^\dagger\right) |0\rangle \\
&= \left(a_4^\dagger b_4^\dagger - a_3^\dagger b_3^\dagger\right) |0\rangle \\
&= |0_3(HV)_4\rangle - |(HV)_3 0_4\rangle.
\end{aligned} \tag{3.13}$$

The  $|\psi^-\rangle$  state is composed of antibunched photons

$$\begin{aligned}
|\psi^-\rangle &= \left(a_1^\dagger b_2^\dagger - b_1^\dagger a_2^\dagger\right) |0\rangle \\
&= \left(a_3^\dagger b_4^\dagger - b_3^\dagger a_4^\dagger\right) |0\rangle \\
&= |H_3 V_4\rangle - |V_3 H_4\rangle.
\end{aligned} \tag{3.14}$$

When rewriting each Bell state input mode of the beam splitter in terms of the output modes of the beam splitter, interference of the photon creation operators occur

for each Bell state. However, despite the perfect interference of identical photons entangled with an atom, the photons exiting the beam splitter are antibunched with probability  $1/4$ . This behavior differs from the interference of identical photons on a beam splitter that are not entangled with another system.

By using polarizing beam splitters, it is easy to detect both the  $|\psi^\pm\rangle$  photonic Bell states after photon interference at the beam splitter; the  $|\psi^+\rangle$  photonic states are composed of photons with opposite polarizations exiting the same port of the beam splitter while the  $|\psi^-\rangle$  state is composed of photons exiting opposite ports of the beam splitter with opposite polarizations. It is theoretically possible to measure all four photonic Bell states with additional waveplates, photon-number resolving detectors, and strongly birefringent materials to create delays between orthogonal polarizations. The birefringent material would need to induce a relative delay between photon polarizations by more than the excited state lifetime (8 ns for  $^{171}\text{Yb}^+$ ) and is not currently commercially available. Note that detecting all four photonic Bell states is generally possible by coupling a photon degree of freedom to a time delay [73]. Detecting a Bell state of light heralds entanglement between remote atoms by projecting the remote atoms into a Bell state.

This treatment of photon interference makes an important assumption: the photons are assumed to be identical. Even though the horizontally polarized photons and the vertically polarized photons may have a frequency difference (see Fig. 3.6b), these polarizations are orthogonal and do not interfere on the beam splitter. Interference only occurs between photons of identical polarization. If photons with identical polarization have a frequency difference, the photon creation operators can

be modified to include a time dependent phase factor. Consider two otherwise identical photons with frequencies  $\omega_{1,2}$  impinging on beam splitter input ports 1 and 2. The joint detection probability of anti-bunched photons at time  $t$  and  $t_0$  can be calculated using the normal-ordered field operators for creation of a photon in beam splitter output modes 3 and 4 [55].

$$\begin{aligned}
P_{34}(t, t_0) &= \langle 0 | a_1 a_2 a_4^\dagger(t) a_3^\dagger(t + t_0) a_3(t + t_0) a_4(t) a_1^\dagger a_2^\dagger | 0 \rangle \\
&= \langle 0 | a_1 a_2 \left( a_1^\dagger(t) + a_2^\dagger(t) \right) \left( a_1^\dagger(t + t_0) - a_2^\dagger(t + t_0) \right) \\
&\quad \times \left( a_1(t + t_0) - a_2(t + t_0) \right) \left( a_1(t) + a_2(t) \right) a_1^\dagger a_2^\dagger | 0 \rangle \quad (3.15)
\end{aligned}$$

The time dependence of the field operators can be arbitrary functions  $a_i^\dagger(t) = a_i^\dagger f_i(t)$ , but here the lineshape of the photons will be assumed identical but with different center frequency  $\omega_{1,2}$ . The time dependent field operators are  $a_i^\dagger(t) = a_i^\dagger e^{-i\omega_i t}$  and  $a_i(t) = a_i e^{i\omega_i t}$ . The normalized joint detection probability is then

$$P_{34}(t, t_0) = \frac{1}{4} |f_1(t + t_0) f_2(t) - f_2(t + t_0) f_1(t)|^2 \quad (3.16)$$

$$= e^{-\Delta t/\tau} \left( \frac{1}{2} - \frac{1}{2} \cos(\Delta\omega \Delta t) \right) \quad (3.17)$$

where the frequency difference between the two photons is  $\Delta\omega = \omega_2 - \omega_1$ , the photon detection time difference is  $\Delta t$ , and the photon exponential lineshape with time constant  $\tau$  has been included. Note that the probability of detecting antibunched photons approaches zero for photon detection time differences  $\Delta t \ll 1/\Delta\omega$ .

Analyzing the photons prior to detection can be accomplished in a similar

manner. For example, the probability to find a photon in output port 3 is

$$\begin{aligned}
P_3(t) &= \langle 0 | a_1 a_2 a_3^\dagger(t) a_3(t) a_1^\dagger a_2^\dagger | 0 \rangle \\
&= \langle 1_1 1_2 | (a_1^\dagger f_1^*(t) - a_2^\dagger f_2^*(t)) (a_1 f_1(t) - a_2 f_2(t)) | 1_1 1_2 \rangle \\
&= \frac{|f_1(t)|^2 + |f_2(t)|^2}{2} \tag{3.18}
\end{aligned}$$

$$= \frac{1}{2} e^{-t/\tau} \tag{3.19}$$

The probability of detecting a single photon in an output port of a beam splitter depends only on the probability distribution of a single photon; there is no beating of photon statistics prior to detecting a single photon. The time dependent photon interference only appears upon detection of a single photon.

These facts can be used to simplify the above description of two non-identical photons impinging on a beam splitter to avoid taking expectation values of long products of photon field operators. The field operators can be modified to keep track of the different frequency photons. One photon is denoted  $\tilde{a}_1^\dagger |0\rangle = |\tilde{1}_1\rangle$  while the other photon retains the notation  $a_1^\dagger |0\rangle = |1_1\rangle$ . Two photons of different frequency impinging on a beam splitter can be described by

$$\begin{aligned}
&= \tilde{a}_1^\dagger a_2^\dagger |0\rangle \\
&= (\tilde{a}_3^\dagger + \tilde{a}_4^\dagger) (-a_3^\dagger + a_4^\dagger) |0\rangle \\
&= (\tilde{a}_4^\dagger a_4^\dagger - \tilde{a}_3^\dagger a_3^\dagger + \tilde{a}_3^\dagger a_4^\dagger - a_3^\dagger \tilde{a}_4^\dagger) |0\rangle \\
&= |(1\tilde{1})_4\rangle - |(1\tilde{1})_3\rangle + |\tilde{1}_3 1_4\rangle - |1_3 \tilde{1}_4\rangle \tag{3.20}
\end{aligned}$$

The probability detecting an antibunched pair of photons can be directly calculated by considering a measurement on the last two state vectors at time  $t = 0$ , followed by free evolution of the remaining photon for time  $\Delta t$ , followed by detection of the second photon. For example, if a photon is detected in port 3, then the remaining state vector with a photon in port 4 undergoes free evolution.

$$\begin{aligned} |\psi, t\rangle &= e^{-i\omega_1\Delta t}|1_4\rangle - e^{-i\omega_2\Delta t}|\tilde{1}_4\rangle \\ &= (e^{-i\omega_1 t} - e^{-i\omega_2 t}) a_4^\dagger |0\rangle \end{aligned} \quad (3.21)$$

The probability of measuring a photon in port 4 after measuring a photon in port 3 is then  $1/2 - 1/2 \cos(\Delta\omega\Delta t)$ , agreeing with the more formal approach from [55]. The probability of detecting a photon in port 3 is time independent because the square of the phase factors in front of each state vector is time independent. This simplified, state vector picture will be useful when considering non-identical photons, each entangled with a qubit, interfering on a beam splitter.

Consider two different  $^{171}\text{Yb}^+$  atoms in large, identical magnetic fields where the Zeeman shift of the  $|1, \pm 1\rangle$  states are separated by more than the  $S_{1/2} \rightarrow P_{1/2}$  transition linewidth. As before, a quarter waveplate is used to map the photon state from atom A from  $|\sigma^+\rangle \rightarrow |H\rangle$  and  $|\sigma^-\rangle \rightarrow |V\rangle$ . However, atom B has the opposite mapping:  $|\sigma^+\rangle \rightarrow |V\rangle$  and  $|\sigma^-\rangle \rightarrow |H\rangle$ . The interfering photons now differ in frequency by  $2\omega_B \equiv \Delta\omega$  and interfere with each other on a beam splitter. Each photon, and its parent atom are spectroscopically distinguishable from each other. Intuition about the subsequent time evolution of the joint atom-photon state may



be gained by examining an energy level diagram of  $^{171}\text{Yb}^+$  (see Fig. 3.7). The sum of the energy of the  $|1, -1\rangle$  and the photon energy connecting the  $|1, -1\rangle$  state to the  $P_{1/2}, |1, 0\rangle$  excited state is equal to the sum of the energy of the  $|1, 1\rangle$  state and the photon state connecting the  $|1, 1\rangle$  state to the  $P_{1/2}, |1, 0\rangle$  excited state for any applied magnetic field in the linear Zeeman regime. The wavefunction of each individual atom-photon pair therefore has a common time-dependent phase factor which can be ignored. Each atom-photon state therefore does not undergo phase evolution, and the product of two such pairs also undergoes no time-dependent phase accumulation. The photons from these atoms impinge on the beam splitter as before and interfere, and the single photon Fock states undergo no phase evolution as before. After exiting the beam splitter, a single photon may be detected. This single photon detection breaks the energy symmetry of the atom-photon states, resulting in time-dependent phase evolution at the photon frequency difference. After the second photon is detected, only the entangled atom states remain and the atomic entangled state undergoes free evolution.

This analysis can be verified by considering the remote atom-photon state  $(|1V\rangle - i|0H\rangle) \otimes (|1\tilde{H}\rangle - i|0\tilde{V}\rangle)$ . The photons interfere on a beam splitter, and as before, the output modes of the beam splitter may be written in terms of the input

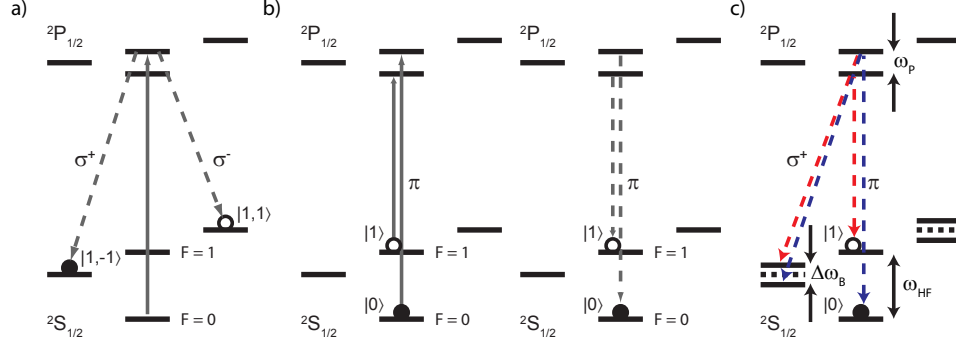


Figure 3.7: Phase evolution of ion photon and ion ion entanglement. The phase evolution of an atom entangled with a photon may be read off by examining the excitation and decay of the the atom. **(a)** When a  $^{171}\text{Yb}^+$  is prepared in the  $|0\rangle$  state and excited to the  $|1,0\rangle$  state of the  $P_{1/2}$  manifold, the photon can decay to the Zeeman states  $|1,\pm 1\rangle$  while emitting a  $\sigma^\pm$  polarized photon. Other than a common phase factor which may be ignored, there is no phase evolution of such a system because the sum of the energies from the  $|0\rangle$  state to the  $|1,-1\rangle$  state to the  $|1,0\rangle P_{1/2}$  state is equal to the sum of the energy from the  $|0\rangle$  state to the  $|1,1\rangle$  state to the  $|1,0\rangle P_{1/2}$  state. **(b)** When encoding atom-photon entanglement in the frequency degree of freedom, a  $^{171}\text{Yb}^+$  atom is prepared in a superposition of the  $|0\rangle$  and  $|1\rangle$  states. An ultrafast laser pulse excites the  $|0\rangle$  state to the  $|1,0\rangle$  state in the  $P_{1/2}$  manifold while the  $|1\rangle$  state is excited to the  $|0,0\rangle$  state in the  $P_{1/2}$  manifold. The sum of the energies of the atom and photon decays paths differ by the  $P_{1/2}$  hyperfine splitting, so the joint two-atom, two-photon state undergoes phase evolution while the photons are in flight. **(c)** Upon detection of a single photon after the beam splitter, the disappearance of a photon breaks the energy symmetry of the decay paths of the photons. If the photon degree of freedom entangled with the atom is polarization, a frequency difference between the  $\sigma^+$  or  $\sigma^-$  photons will turn in to phase evolution of the atom entangled state after a single photon is detected. If the frequency degree of freedom is used, there is phase accumulation at frequency  $\omega_{P_{1/2}} + \omega_{HF}$ .

modes of the beam splitter

$$\begin{aligned}
|H_1\tilde{V}_2\rangle &= a_1^\dagger \tilde{b}_2^\dagger |0\rangle \\
&= \left( -a_3^\dagger \tilde{b}_3^\dagger - a_4^\dagger \tilde{b}_3^\dagger + a_3^\dagger \tilde{b}_4^\dagger + a_4^\dagger \tilde{b}_4^\dagger \right) |0\rangle \\
&= -|(H\tilde{V})_3 0_4\rangle - |\tilde{V}_3 H_4\rangle + |H_3 \tilde{V}_4\rangle + |0_3(H\tilde{V})_4\rangle
\end{aligned} \tag{3.22}$$

where the tilde differentiates the photon from atom 2 that was rotated by the half wave plate and impinges on beam splitter input port 2. Similar analysis on the remaining input states yields

$$\begin{aligned}
|V_1\tilde{V}_2\rangle &= -\left( -b_3^\dagger \tilde{b}_3^\dagger - b_4^\dagger \tilde{b}_3^\dagger + b_3^\dagger \tilde{b}_4^\dagger + b_4^\dagger \tilde{b}_4^\dagger \right) |0\rangle \\
&= -|(V\tilde{V})_3 0_4\rangle - |\tilde{V}_4 V_4\rangle + |V_3 \tilde{V}_4\rangle + |0_3(V\tilde{V})_4\rangle \\
|\tilde{H}_1 H_2\rangle &= -|(H\tilde{H})_3 0_4\rangle - |\tilde{H}_3 H_4\rangle + |H_3 \tilde{H}_4\rangle + |0_3(H\tilde{H})_4\rangle \\
|V\tilde{H}\rangle &= -|(V\tilde{H})_3 0_4\rangle - |\tilde{H}_3 V_4\rangle + |V_3 \tilde{H}_4\rangle + |0_3(V\tilde{H})_4\rangle
\end{aligned} \tag{3.23}$$

The entangled state between the remote atoms and their emitted photons is

$$\begin{aligned}
|\psi\rangle &= |11\rangle \left( -|(V\tilde{H})_3 0_4\rangle - |\tilde{H}_3 V_4\rangle + |V_3 \tilde{H}_4\rangle + |0_3(V\tilde{H})_4\rangle \right) \\
&\quad - |00\rangle \left( -|(H\tilde{V})_3 0_4\rangle - |\tilde{V}_3 H_4\rangle + |H_3 \tilde{V}_4\rangle + |0_3(H\tilde{V})_4\rangle \right) \\
&\quad - i|01\rangle \left( -|(H\tilde{H})_3 0_4\rangle - |\tilde{H}_3 H_4\rangle + |H_3 \tilde{H}_4\rangle + |0_3(H\tilde{H})_4\rangle \right) \\
&\quad - i|10\rangle \left( -|(V\tilde{V})_3 0_4\rangle - |\tilde{V}_4 V_4\rangle + |V_3 \tilde{V}_4\rangle + |0_3(V\tilde{V})_4\rangle \right)
\end{aligned} \tag{3.24}$$

By examining each term in Eqn. 3.24, the total energy of each term is equal to

twice the sum of the energy of the  $|1, -1\rangle$  state and the photon connecting the  $|1, -1\rangle$  to the  $|1, 0\rangle$  state of the  $P_{1/2}$  excited state manifold. The time evolution of this wavefunction has a common phase in front of each term and may be neglected. Assuming single photon detectors without photon number resolution, only photon states with opposite polarizations will be heralded. If a horizontally polarized photon is detected out of port 3, the two-atom one-photon state when the detector fires ( $t = 0$ ) is

$$\begin{aligned}
|\psi\rangle &= |11\rangle (-|V_3\rangle - |V_4\rangle) - |00\rangle (-|\tilde{V}_3\rangle + |\tilde{V}_4\rangle) \\
&- i|01\rangle (-|H_4\rangle + |\tilde{H}_4\rangle)
\end{aligned} \tag{3.25}$$

This state undergoes time evolution which may be computed from the free evolution of the atoms and the remaining photon.

$$\begin{aligned}
|\psi, \Delta t\rangle &= -e^{-i\omega_2\Delta t}e^{-2\omega_B\Delta t}|11\rangle (|V_3\rangle + |V_4\rangle) - e^{-i\omega_1\Delta t}|00\rangle (-|\tilde{V}_3\rangle + |\tilde{V}_4\rangle) \\
&- ie^{-i\omega_B\Delta t}|01\rangle \left(-e^{-i\omega_1\Delta t}|H_4\rangle + e^{-i\omega_2\Delta t}|\tilde{H}_4\rangle\right) \\
&= -b_3^\dagger|0\rangle (|00\rangle + e^{-i\Delta\omega\Delta t}|11\rangle) - b_4^\dagger|0\rangle (|00\rangle - e^{-i\Delta\omega\Delta t}|11\rangle) \\
&+ -ie^{-i(\omega_B+\omega_1)\Delta t}|01\rangle (e^{-i\Delta\omega\Delta t} + 1) a_4^\dagger|0\rangle
\end{aligned} \tag{3.26}$$

While waiting for the second photon, the wavefunction accumulates phase at the photon frequency difference  $(\omega_1 - \omega_2)\Delta t = \Delta\omega\Delta t$ . The probability of detecting a horizontally polarized photon out of port 4 of the beam splitter is  $1/2 - 1/2 \cos(\Delta\omega\Delta t)$ , resulting in the atoms being projected in to the state  $|01\rangle$ , a state with no entan-

glement. If the second photon detected is vertically polarized out of port 4, the resulting atom state is entangled:  $|00\rangle - e^{-i\Delta\omega\Delta t}|11\rangle$ . If the second detected photon is vertically polarized out of port 3 of the beam splitter, the resulting atom state is also entangled:  $|00\rangle + e^{-i\Delta\omega\Delta t}|11\rangle$ . Both of these entangled states acquire a phase that depends on the photon frequency difference  $\Delta\omega$  and detection time difference  $\Delta t$ . The decoherence mechanism from non-identical photons interfering on a beam splitter becomes clear. If the photon detection time difference cannot be well determined compared to  $1/\Delta\omega$ , repeated measurements result in averaging over the entangled state phase. This averaging process is decoherence.

### 3.3.1 **Heralded entanglement using photon frequency qubits**

Photon polarization need not be used as the photon degree of freedom entangled with the atom state. Atoms may be entangled with the frequency of an emitted photon (see Fig. 3.7c), and the resulting photons can interfere on a beam splitter. Entangling the photon frequency degree with a quantum memory is inherently more resistant to decoherence than entangling a quantum memory with photon polarization. The polarization degree of freedom of the photon interacts with transparent material which in general has spatially inhomogeneous birefringence. Photon frequency is shifted by nonlinear processes and is highly suppressed at the single photon level. As in the case of entanglement between atom spin and photon polarization, detection of the  $|\psi^-\rangle$  photon state heralds entanglement between remote atoms [33, 62, 63]. Previous experiments have treated the two photon colors as separate,

non-interfering field modes on a beam splitter. However, since both photons have the same polarization, the “red” and “blue” photons do interfere because they have the same polarization, producing time dependent phase accumulation. In addition, the sum of the energy of the atomic  $|0\rangle$  state and the photon energy connecting the  $|0\rangle$  state to the  $|1, 0\rangle$  state of the  $P_{1/2}$  manifold is not equal to the sum of the energy of the  $|1\rangle$  state and the photon energy connecting the  $|1\rangle$  state to the  $|0, 0\rangle$  excited state in the  $P_{1/2}$  manifold. Since these energies differ by the hyperfine splitting  $\omega_P$  of the  $P_{1/2}$  manifold, each atom-photon state will undergo phase evolution at this frequency while the photons are in flight. In [62, 63], the single photon counting PMTs did not have the bandwidth to track this phase evolution, but the heralding of the  $|\psi^-\rangle$  remote atom state in these experiments makes all phase accumulation cancel. This occurs, as will be shown below, because the  $|\Psi^-\rangle$  remote atom state has common phase evolution at  $\omega_P$  as the photons are in flight, and heralding of this remote atom state involves detection of the  $|\psi^-\rangle$  photonic Bell state. This state is a superposition of “red” and “blue” photons exiting opposite beam splitter ports, providing common phase accumulation between photon detection events.

Consider two  $^{171}\text{Yb}^+$  ions may be prepared in the state  $(\alpha|0\rangle + \beta|1\rangle) \otimes (\gamma|0\rangle + \delta|1\rangle)$  and excited by an ultrafast  $\pi$ -polarized laser pulse. The  $|0\rangle$  and  $|1\rangle$  qubit states are excited to the  $|1, 0\rangle$  and  $|0, 0\rangle$  levels in the  $P_{1/2}$  manifold respectively where they undergo spontaneous emission. If an experiment post selects on the  $\pi$ -polarized emitted radiation, only the  $\pi$  radiation need be considered. The photons of differing frequency are denoted  $|r\rangle = a_r^\dagger|0\rangle$  for the lower energy (red) photon from the spontaneous decay of the  $|0, 0\rangle$   $P_{1/2}$  level and  $|b\rangle = a_b^\dagger|0\rangle$  from the spontaneous decay of

the  $|1, 0\rangle$   $P_{1/2}$  level (see Fig. 3.7). The resulting atom-photon frequency entangled state is

$$\begin{aligned} |\psi\rangle &= (\alpha|0\rangle|b\rangle + \beta|1\rangle|r\rangle) \otimes (\gamma|0\rangle|b\rangle + \delta|1\rangle|r\rangle) \\ &= \alpha\gamma|00\rangle|bb\rangle + \beta\delta|11\rangle|rr\rangle + \beta\gamma|10\rangle|rb\rangle + \alpha\delta|01\rangle|br\rangle. \end{aligned} \quad (3.27)$$

Note that while the photons are in flight, there is time evolution of the joint atom-photon entangled state at the  $P_{1/2}$  hyperfine splitting because the sum of each atomic energy level and its associated photon energy up to the  $P_{1/2}$  energy level differs by the excited state hyperfine splitting. The time evolution of the atom photon state is

$$|\psi, t\rangle = \alpha\gamma|00bb\rangle + \beta\delta e^{2i\omega_p t}|11rr\rangle + e^{i\omega_p t}(\beta\gamma|10rb\rangle + \alpha\delta|01br\rangle) \quad (3.28)$$

where the joint atom-photon wave function accumulates positive phase as time progresses. The beam splitter output modes written in terms of the input modes are

$$\begin{aligned} a_{1b}^\dagger a_{2b}^\dagger |00\rangle &= -|(bb)_3 0_4\rangle + |0_3(bb)_4\rangle \\ a_{1r}^\dagger a_{2r}^\dagger |00\rangle &= -|(rr)_3 0_4\rangle + |0_3(rr)_4\rangle \\ a_{1r}^\dagger a_{2b}^\dagger |00\rangle &= -|(rb)_3 0_4\rangle - |b_3 r_4\rangle + |r_3 b_4\rangle + |0_4(rb)_4\rangle \\ a_{1b}^\dagger a_{2r}^\dagger |00\rangle &= -|(rb)_3 0_4\rangle - |r_3 b_4\rangle + |b_3 r_4\rangle + |0_4(rb)_4\rangle \end{aligned} \quad (3.29)$$

where the two photon modes  $\{|r\rangle, |b\rangle\}$  are not orthogonal but are separated in

frequency by  $\omega_{HF} + \omega_P$ . After the 50/50 beam splitter, the resulting state is

$$\begin{aligned}
|\psi, t\rangle &= \alpha\gamma|00\rangle (-|(bb)_3 0_4\rangle - |0_3(bb)_4\rangle) \\
&+ \beta\delta e^{2i\omega_P t}|11\rangle (-|(rr)_3 0_4\rangle + |0_3(rr)_4\rangle) \\
&+ \beta\gamma|10\rangle e^{i\omega_P t} (-|(rb)_3 0_4\rangle - |b_3 r_4\rangle + |r_3 b_4\rangle + |0_3(rb)_4\rangle) \\
&+ \alpha\delta|01\rangle e^{i\omega_P t} (-|(br)_3 0_4\rangle - |r_3 b_4\rangle + |b_3 r_4\rangle + |0_3(br)_4\rangle) \quad (3.30)
\end{aligned}$$

Detecting the  $|\psi^-\rangle$  photon state corresponds to detecting photons exiting opposite beam splitter output ports. Post selecting on these antibunched photon events, Eqn. 3.30 shows there is no differential time evolution of the  $|01\rangle$  and  $|10\rangle$  terms while the photons are in flight: both terms have the same phase evolution at the  $P_{1/2}$  hyperfine frequency. After one photon is detected, both terms have the same energy, so there is no phase evolution while waiting for the detection of the second photon. Despite the interference of photons of different color separated by  $\omega_{HF} + \omega_P$ , the phase cancels upon detection of the  $|\psi^-\rangle$  photon state. This cancellation while the photons are in flight and after detection of one of the two photons enabled early experiments with remote entanglement with frequency qubits using PMTs with bandwidth of  $\sim 500$  MHz, less than the difference frequency scales of the photons and atoms [62, 63].

### 3.4 Fast remote entanglement of trapped ions

In order to generate remote entanglement between atoms in physically separated ion traps, we optically pump both atoms to the  $|0, 0\rangle$  state. A picosecond laser



pulse resonant with the  $^2S_{1/2} \rightarrow ^2P_{1/2}$  transition excites trapped atoms in different modules [49]. The atoms spontaneously emit photons, resulting in the entangled photon-polarization, atom-spin state  $\frac{1}{2}(|1, 1\rangle|\sigma^-\rangle - |1, -1\rangle|\sigma^+\rangle)^{\otimes 2}$  due to atomic selection rules (Fig. 5.2a). A large NA = 0.6 single atom microscope objective collects  $\sim 10\%$  of the emitted photons, and the emitted photons pass through  $\lambda/4$  waveplates to convert the photon polarization to linear horizontal (H) or linear vertical (V) ( $\sigma^+ \rightarrow H$  and  $\sigma^- \rightarrow V$ ), resulting in the atom photon state

$$\begin{aligned} |\psi\rangle &= (|1, 1\rangle|V\rangle - i|1, -1\rangle|H\rangle)^{\otimes 2} \\ &= |\Phi^+\rangle_\gamma|\Phi^-\rangle_{\text{ions}} - |\Phi^-\rangle_\gamma|\Phi^+\rangle_{\text{ions}} - i|\Psi^+\rangle_\gamma|\Psi^+\rangle_{\text{ions}} - i|\Psi^-\rangle_\gamma|\Psi^-\rangle_{\text{ions}} \end{aligned} \quad (3.31)$$

with  $|\Psi^\pm\rangle_{\text{ions}} = |-1\rangle|+1\rangle \pm |+1\rangle|-1\rangle$ . Each objective is mode matched to a single-mode optical fiber which delivers the photons to an interferometer with a 50/50 beam-splitter as the central element. The interferometer effects a Bell state measurement of the photon state, and we detect two out of the four possible Bell states of light exiting the beam-splitter to herald the entanglement of the remote atoms' spins [33, 50]. We select the two-photon Bell states of light  $|HV\rangle + e^{i\phi_D}|VH\rangle$ , where  $\phi_D$  is 0 or  $\pi$  depending on which pair of detectors registers the photons. The phase  $\phi_D$  is 0 if coincident photons are detected on PMTs 1 and 2 or 3 and 4 (see Fig. 5.1a). The phase  $\phi_D$  is  $\pi$  if coincident photons are detected on PMTs 1 and 3 or 2 and 4. Finally, a series of three microwave pulses transfers the atoms into the  $\{|0\rangle, |1\rangle\}$  basis (Fig. 5.2b), ideally resulting in the heralded entangled state of the

two remote atomic qubits

$$\begin{aligned}
|\psi\rangle &= |01\rangle - ie^{-i(\phi_{1b}-\phi_{1a}+\phi_{2a}-\phi_{2b}+\phi_{3b}-\phi_{3a}-\Delta\omega_B t'+\phi_D)}|10\rangle \\
&= |01\rangle - e^{i\phi_{AB}}|10\rangle
\end{aligned} \tag{3.32}$$

with the intermodule phase  $\phi_{AB}$ . In addition to the phase differences from the microwave transfer pulses and the photon detector pair phase  $\phi_D$ , several static geometric factors determine the intermodule phase

$$\phi_{AB} = \phi_D + \Delta\omega_{AB}t + kc\Delta\tau + k\Delta x + \Delta\phi_T. \tag{3.33}$$

In this equation, the phase evolves with the difference in qubit splittings between module A and B,  $\Delta\omega_{AB} = \omega_{0,A} - \omega_{0,B} \approx 2\pi \times 2.5$  kHz, owing to controlled Zeeman shifts [22]. The stable geometric phase factors  $kc\Delta\tau < 10^{-2}$  and  $k\Delta x < 10^{-2}$  result from the difference in excitation time  $\Delta\tau < 100$  ps and difference in path length  $\Delta x < 3$  cm between each atom and the beam-splitter. Here  $c$  is the speed of light and  $k \sim 0.33 \text{ m}^{-1}$  is the wavenumber associated with the energy difference of the photon decay modes (here, the energy difference between  $\sigma^+$  and  $\sigma^-$  photons). The final contribution is the stable phase difference of the microwave transfer pulses  $\Delta\phi_T$  across the modules.

Given a heralded photon coincidence event, we verify entanglement between ion trap modules by measuring atomic state populations and coherences following standard 2-qubit tomography protocols [74]. Note that because the post-selected,

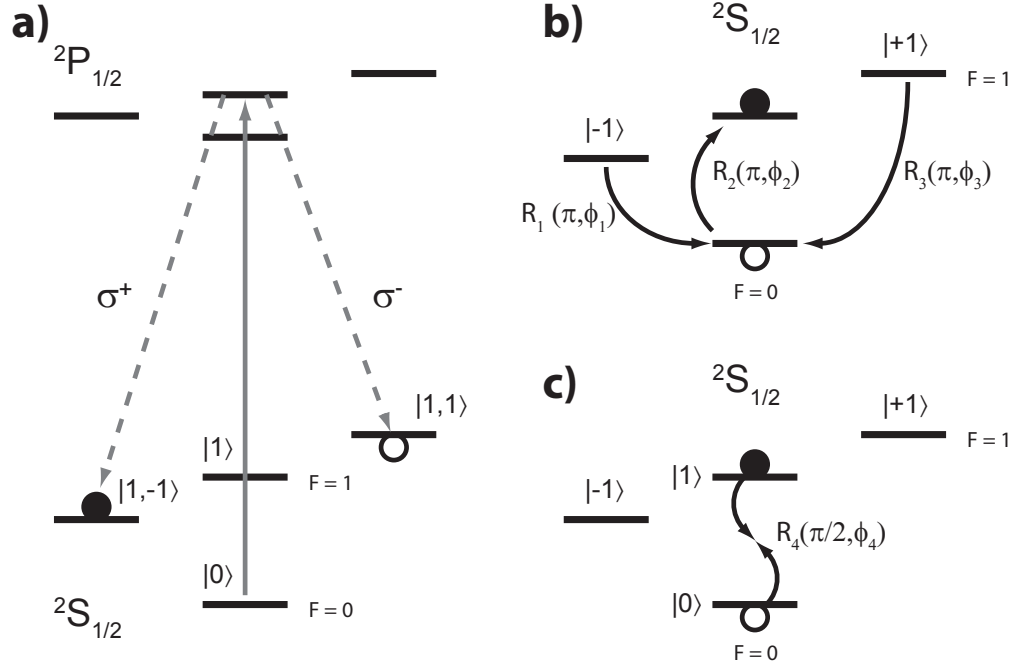


Figure 3.8: Qubit manipulations for generating entanglement between and within modules. **a)** Resonant excitation scheme and single photon emission in  $\text{Yb}^+$  atom system. After optically pumping the atoms to the  $|F, m_F\rangle = |0, 0\rangle$  state of the  $^2S_{1/2}$  manifold, a frequency-doubled, mode-locked Ti:sapphire laser excites the atom to the  $|1, 0\rangle$  state of the  $^2P_{1/2}$  manifold whereby the atom decays to the  $|1, \pm 1\rangle$  states via emission of  $\sigma^\mp$  polarized photons into optical fibers. **b).** After interference of the two photons on a 50/50 non-polarizing beam-splitter, we apply a series of three microwave transfer  $\pi$  pulses to transfer the entangled state to the clock basis, resulting in the state  $|01\rangle + e^{i\phi_{AB}}|10\rangle$  where  $\phi_{AB}$  is the intermodular phase. **(c)** The entangled state is analyzed with a fourth microwave  $\pi/2$  pulse.

two photon detection events are composed of two photons with opposite polarization, the remote atoms will be anti-correlated even if the photons do not interfere on the 50/50 beam splitter. The resulting fidelity assuming perfect entanglement between the photon-polarization and the ion spin would be 0.5. Verifying the phase coherence of the two atom state is crucial to proving remote entanglement.

The fidelity of the entangled state is  $(\rho_{01,01} + \rho_{10,10})/2 + |\rho_{01,10}|$  where  $\rho_{ij,kl} = \langle ij|\rho|kl\rangle$  with  $i, j, k, l \in (0, 1)$ . The elements  $\rho_{00,00}$ ,  $\rho_{10,10}$ ,  $\rho_{01,01}$ , and  $\rho_{11,11}$  are from direct measurements of the entangled state after the microwave pulses transfer the state to the  $\{|0\rangle, |1\rangle\}$  basis. The elements  $\tilde{\rho}_{ij,kl}$  come from measurements after the  $\pi/2$  analysis pulse with phases  $\phi_{4a}$  and  $\phi_{4b}$ .

$$\tilde{\rho}_{00,00} + \tilde{\rho}_{11,11} - \tilde{\rho}_{10,10} - \tilde{\rho}_{01,01} = 2|\rho_{01,10}| \cos(\phi_{4a} - \phi_{4b}) + 2|\rho_{00,11}| \cos(\phi_{4a} + \phi_{4b}) \quad (3.34)$$

In this experiment, we control the relative phase difference of the analysis pulse  $\phi_{4a} - \phi_{4b}$ , but have no control over the absolute phase sum  $\phi_{4a} + \phi_{4b}$  from shot to shot. Therefore, the  $|\rho_{00,11}|$  terms averages out and the measured parity oscillation contrast comes entirely from the  $\rho_{01,01}$  term. The remote entangled state fidelity is therefore  $F = (\rho_{01,01} + \rho_{10,10} + |\rho_{01,10}|)/2$  [49].

The probability of detecting odd parity after the three microwave transfer pulses and the fourth,  $\pi/2$  analysis pulse is

$$P_{\text{odd}} = \frac{1}{2} + \frac{\Pi_c}{2} \cos \left( (\phi_{1b} - \phi_{1a}) + (\phi_{2b} - \phi_{2a}) + (\phi_{3a} - \phi_{3b}) + (\phi_{4b} - \phi_{4a}) - \Delta\omega_B t' \right) \quad (3.35)$$

where the phase  $\phi_{ia} - \phi_{ib}$  is the microwave phase difference of the  $i$ -th microwave pulse on ion a and ion b, and  $\Delta\omega_B t'$  is the phase accumulation of the entangled state from a magnetic field gradient for duration  $t'$  before the microwave transfer and analysis pulses. Fitting the observed parity oscillation with contrast  $\Pi_c$  upon varying the phase of one of the microwave pulses on one ion results in a measured average entangled Bell state fidelity of  $0.78 \pm 0.03$ . Imperfect mode matching at the beam-splitter contributes  $0.08 \pm 0.02$  to the infidelity. The measured atom-photon polarization entanglement is  $0.92 \pm 0.02$  per ion trap which contributes 0.15 to the remote entangled state infidelity. We attribute the atom-photon polarization infidelity to spatially inhomogeneous rotations of the photon polarization, polarization-dependent loss, and multiple excitations of the remote atoms from imperfect pulse picking of resonant fast laser pulses. Combining imperfect ion-photon polarization entanglement with imperfect mode matching at the beam-splitter yields an expected fidelity of  $0.79 \pm 0.02$ , consistent with observation. This fidelity could be improved with the use of fiber beams-splitters to improve spatial mode matching of the photons. In addition, the use of phase masks could correct polarization error introduced by optical elements associated with single photon collection and transmission. Electro-optic pulse pickers with higher extinction ratios could reduce errors associated with multiple excitations of remote atoms in different modules.

Since the phase of the entangled state evolves in time (2nd term of Eq. 3.33), the remote atomic entanglement coherence time can be measured with Ramsey spectroscopy. Unlike a Ramsey experiment with a single atom, this measurement is not sensitive to long-term stability of the local oscillator [22, 75]. We measure

the remote entangled state coherence time by repeating the above experiment with constant transfer pulse phase  $\Delta\phi_T$  while varying the Ramsey zone delay before a final  $\pi/2$  microwave rotation. We utilize a spin echo pulse in the middle of the Ramsey zone delay to account for slow magnetic field gradient drifts, and measure an entanglement coherence time of 1.12(2) seconds, well in excess of the required time to create remote entanglement between modules (Fig 3.9c). Our experiment thus crosses the threshold where fault-tolerant error correction can propagate entanglement without a superexponential overhead in resources [17].

In previous experiments, entanglement between remote atom spins at rates of  $0.002 \text{ sec}^{-1}$  was accomplished using atom-photon frequency entanglement [62], and at rates of  $0.026 \text{ sec}^{-1}$  using atom-photon polarization entanglement [50]. Here, we dramatically increase the single photon collection efficiency by using high numerical aperture microscope objectives and detecting two out of four Bell states of light emitted by the atoms to achieve a heralded entanglement rate of  $4.5 \text{ sec}^{-1}$ .

The remote entanglement rate is limited by the collection and detection efficiency of emitted photons from the atoms. The probability for coincident detection of two emitted photons upon exciting both atoms simultaneously with a resonant laser pulse is  $P = p_{Bell}[P_\pi P_{S_{1/2}} Q_E T_{fib} T_{opt} \frac{\Omega}{4\pi}]^2 = 9.7 \times 10^{-6}$  where  $P_\pi = 0.95$  is the probability of exciting the atom with a resonant  $^2S_{1/2} \rightarrow ^2P_{1/2}$  laser pulse,  $^2P_{S_{1/2}} = 0.995$  is the probability to decay from  $^2P_{1/2} \rightarrow ^2S_{1/2}$  (as opposed to the  $^2D_{3/2}$  state),  $p_{Bell} = 1/2$  accounts for selecting two of the four possible Bell states of light,  $Q_E \approx 0.35$  is the quantum efficiency of the single photon PMT detectors,  $T_{fib} \approx 0.14$  is the fiber coupling and transmission probability of a single-mode op-

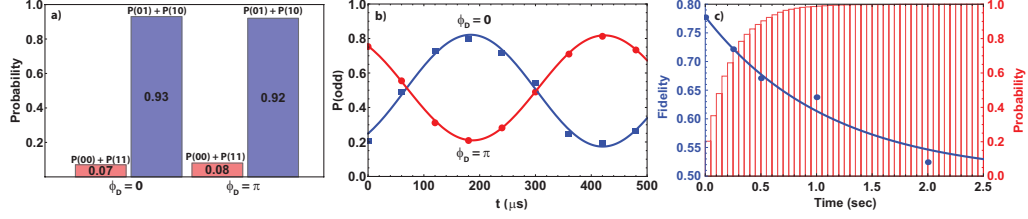


Figure 3.9: Herald ed entanglement fidelity and rate between modules. **a)** Populations of two remote atoms after heralding entanglement between modules. After detecting the photon Bell states ( $\phi_D = 0$  or  $\pi$ ), microwave transfer pulses rotate the remote atom populations to the  $\{|0\rangle, |1\rangle\}$  basis. Subsequent detection of the remotely entangled atoms results in measurement of odd parity,  $P(01) + P(10)$ , with high probability. **b)** Phase coherent time evolution of the remote entangled state with the application of an intermodule magnetic field gradient. After heralding remote entanglement between modules and applying microwave transfer pulses, the addition of a time delay prior to a  $\pi/2$  rotation on both atoms results in an out-of-phase oscillatory behavior of the remote atom entangled state with  $\phi_D = 0$  or  $\pi$  (blue squares and red circles respectively, see Eq. 3.33). **c)** Remote entangled state coherence and generation probability vs. time. We measure the remote entangled state coherence time by adding a Ramsey zone delay in the presence of an intermodular magnetic field gradient before application of a spin echo pulse and a  $\pi/2$  microwave rotation as described in the text. The decay of the fidelity from the measured loss of phase coherence of the entangled state points to magnetic field gradient noise as the dephasing mechanism. A fit to an exponential function yields a coherence time of 1.12(2) seconds. The probability of generating entanglement after a given time interval is shown in red. A fit (reduced  $\chi^2 = 0.94$ ) to an exponential function gives the average remote entanglement rate  $4.5 \text{ sec}^{-1}$ . Error bars in a)-c) (not shown for clarity) are  $\pm 1.4\%$  due to state detection error.

tical fiber,  $T_{opt} = 0.95$  is the photon transmission through optical components, and  $\frac{\Omega}{4\pi} = 0.1$  is the fraction of the solid angle each microscope objective subtends. The experimental repetition rate of 470 kHz is limited by the need for Doppler cooling (adding  $\sim 500$  ns on average to the repetition time), the atomic state lifetime of the  $^2P_{1/2}$  state (necessitating  $\sim 1 \mu\text{s}$  of optical pumping for state preparation of the pure quantum state  $|0\rangle$ ), and sound wave propagation time in AOM crystals used in the experiment. These factors result in a measured atom-atom entanglement rate of  $4.5 \text{ sec}^{-1}$ .

The observed entanglement rate within and between modules is faster than the observed entangled qubit decoherence rate. This is critical in quantum modular architectures because the required resource scaling is superexponential in the ratio of decoherence rate to entanglement rate [17]. This ratio is observed to be 0.2 in this experiment, many orders of magnitude lower than previous experiments demonstrating remote entanglement [50, 65, 66]. Overcoming the resource scaling requirement makes trapped ions a leading candidate for realizing a quantum network.

There are several ways in which the heralding rate of remote entanglement could be made higher at the expense of remote entanglement fidelity. If the single photon detectors have significant noise during the photon coincidence window, the coincident click rate will increase. Secondly, if the photons are spatially mismatched on the beam splitter, the two photon coincidence rate will also be higher. Neither of these processes play a significant role in the experiments presented here.

In the presence of single photon detector noise, the photon coincidence rate will increase at the expense of remote qubit entanglement fidelity. If the probability



of collecting and detecting a single photon from a qubit is  $p$ , then there are 8 possible detector pairs that could fire to give a remote entanglement event. If this process is attempted at a rate  $R$ , then the remote entanglement rate is  $8p^2R$ . During the coincidence window  $T$ , the single photon detectors give a dark count probability  $p_{\text{dark}} = R_{\text{dark}}T$  if the average dark count rate is  $R_{\text{dark}}$ . There are 8 possible dark-count-single-photon pairs, so the rate of detecting a qubit photon and a dark count photon is  $8pp_{\text{dark}}R$ . The ratio of these processes can be used to estimate the infidelity owing to single photon detector dark counts. The ratio of these two processes is  $p_{\text{dark}}/p$ . If one of the coincidence detection events is from a dark count, it is uncorrelated with the state of the atom. The resulting two qubit state will show no coherence but will show the correct anti-correlated population half of the time.

The resulting lowered fidelity from dark counts may be computed by considering  $N + M$  total photon coincidence events from which  $N$  events are from detection of a photon from each qubit, and  $M$  events where at least detected photon is from a dark count. The resulting modified fidelity  $F'$  in terms of the bare fidelity  $F$  (no detector dark counts) is

$$F' = F \frac{N}{N + M} + \frac{1}{4} \frac{M}{N + M}. \quad (3.36)$$

The factor of  $\frac{1}{4}$  comes from the fact that uncorrelated atoms have a 0.5 probability of being in an antisymmetric state and have zero phase coherence. The photon coincidence rate will increase at the expense of remote atom entanglement. If the modified fidelity  $F'$  is set to  $0.5 + \epsilon$  where  $\epsilon$  is a positive number less than 0.5, and

the modified entanglement rate  $R_{\text{ent}}$  in terms of the bare entanglement rate  $R_{\text{ent}}^0$  is

$$\frac{R_{\text{ent}}}{R_{\text{ent}}^0} = \frac{4F - 1}{4\epsilon + 1}. \quad (3.37)$$

The maximum increase of the entanglement rate, assuming a bare fidelity  $F = 1$  and taking the limit  $\epsilon \rightarrow 0$  is a factor of 3. The dark count probability for experiments in this thesis and in [20, 59] is  $10 \text{ sec}^{-1} \times 60 \text{ ns} = 6 \times 10^{-7}$  per entanglement attempt, and the probability of detecting a single photon per entanglement attempt is  $\sim 5 \times 10^{-3}$ .

If the photons are matched on the beam splitter, there are 16 possible detector pairs that might fire, each of which heralds its appropriate remote atom entangled state. The interferometer as shown in Fig. 3.4 in conjunction with non-photon number resolving detectors is capable of detecting 12/16 possible detector pairs. If the photons interfere perfectly, 8/16 possible pairs herald two out of the four possible Bell states. If the photons are spatially misaligned on the beam splitter, detectable two-photon coincidences will result from 12/16 possible detector pairs, heralding a remote atom product state. The increase in two-photon coincidence rate is 1.5. The typical interferometer visibility in the experiments presented here is  $V = 0.95 - 0.97$ , so the remote entanglement rate is not inflated significantly by lack of photon interference.

### 3.5 Entanglement of quantum memories using distinguishable photon interference

Most qubits systems to date that have been entangled using heralded photon interference have relied on qubits emitting identical photons. Atoms naturally emit identical photons, but solid state systems may emit distinguishable photons from uncontrolled external fields coupling to the solid state qubits. The requirement of using indistinguishable photons is an impediment towards constructing large scale quantum networks composed of heterogeneous qubits. In addition, variation in the qubits' environments from manufacturing variability leads to variations in the photon emission frequency.

The use of photons with frequency difference of order the photon bandwidth or larger has been considered before [55–57]. The use of photons with large frequency differences degrades the entangled state fidelity. One solution is to make use of “quantum eraser” techniques where only photon interarrival times  $\Delta t$  much less than  $2\pi/\Delta\omega$  where  $\Delta\omega$  is the photon frequency difference. Because the detection time is shorter than  $2\pi/\Delta\omega$ , the photon frequency difference cannot be measured in principle. The entangled state fidelity is recovered while exponentially slowing the entanglement rate [51, 65].

However, quantum mechanics guarantees unitary evolution of quantum systems will be observed if all degrees of freedom are accounted for. In addition, the wave-like properties of photons with non-orthogonal polarization should always in-

interfere on a beam splitter regardless of the frequency difference of the photons. In this light, there should be no need to slow the remote entanglement rate to recover fidelity if the interference of distinguishable photons, with resulting time dependence owing to the photon frequency difference, can be tracked.

If distinguishable photon interference is used, the remote atom state is projected in to an entangled state with a time dependent phase such as  $|01\rangle + e^{-i\Delta\omega\Delta t}|10\rangle$  (see Eqn. 3.26). The reason for the infidelity of the atom state arising from the interference of distinguishable photons becomes clear. If the entangled state phase  $\Delta\omega\Delta t$  is averaged over all experimental shots, the fidelity of the entangled atom state will be poor. If single photon detectors are used with poor timing resolution  $t_r \gg 2\pi/\Delta\omega$ , the entangled state phase cannot be determined shot to shot given the exponential statistical distribution of the photon interarrival times. Averaging over the photon interarrival time will result in measuring low entangled state fidelity. “Quantum eraser” experiments work by selecting approximately zero phase on each experimental shot by ensuring  $\Delta\omega\Delta t \ll 2\pi$ . Note that these eraser experiments could also be modified to include any constant fixed photon interarrival time as long as  $\Delta t$  can be accurately determined much better than  $2\pi/\Delta\omega$ .

Assuming spectroscopy can be done on each qubit, the photon frequency difference can be measured precisely. In  $^{171}\text{Yb}^+$  experiments using polarization encoded photons, microwave spectroscopy can easily determine the frequency difference between the  $|+1\rangle$  and  $|-1\rangle$  states. The remaining limitation is the bandwidth of the single photon detectors needed to accurately determine the entangled state phase by localizing each photon in time to less than  $1/\Delta\omega$ . If these conditions are sat-

ified, all photon coincidence time differences can be used to generate high-fidelity entanglement.

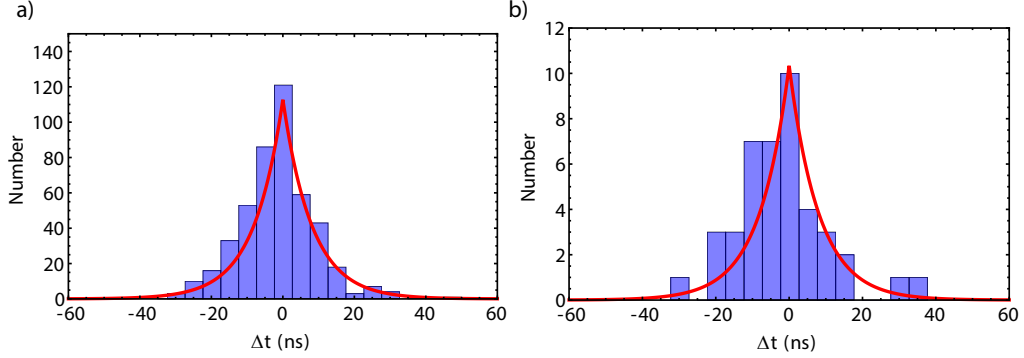


Figure 3.10: Photon statistics from interference of identical photons entangled with a qubit. Because the photons are identical ( $\Delta\omega \ll 1/\tau$ ), there is no beating of the photon number statistics as a function of interarrival time and no time evolution of the atom photon state while the photons are in flight or during the photon interarrival time  $\Delta t$ . **(a)** Photon interarrival times for detector pairs of opposite polarization, totaling 458 out of 500 coincidence events. The normalized curve is a exponential fit with characteristic lifetime of the  $P_{1/2}$  state  $\tau = 8.12$  ns. **(b)** Photon interarrival times for detector pairs detecting photons of identical polarization exiting the opposite beam splitter port. The number of observed photon coincidences for these detector pairs is 42 out of 500 total coincidences owing to imperfect mode matching of the photons on the 50/50 BS.

The remote ions are entangled using the polarization of single photons entangled with the Zeeman states  $|\pm 1\rangle$ . A  $\pi$ -polarized pulse of duration  $\sim 2$  ps excites the atom to the  $P_{1/2}$  state, followed by spontaneous emission to the ground state  $S_{1/2}$  manifold. The photons are collected along the quantization axis and coupled to a single mode optical fiber. The photons pass through a quarter wave plate to convert  $\sigma^\pm$  polarization to linear polarization, and the  $pi$ -polarized photons do not couple to Gaussian  $TEM_{00}$  modes. The fibers are strained to maintain the photon polarization. The atom-photon state from each node is  $|+1\rangle|V\rangle - i|-1\rangle|H\rangle$ .

Photons from each trapped ion impinge on the 50/50 beam splitter before

being spatially sorted in the  $\{|H\rangle, |V\rangle\}$  basis by thin film polarizers. The photons are detected in a coincidence window of duration  $T = 60$  ns that begins with the ultrafast excitation pulse to encompass  $>99$  % of the photonic temporal profile. The photon detection statistics corresponding to the interference of identical photons with frequency difference  $\Delta\omega \ll 1/\tau$  is shown in Fig. 3.10a. Detector pairs measuring  $|H_3H_4\rangle$  and  $|V_3V_4\rangle$  are shown in Fig. 3.10b. Ideally, if identical photons interfere on the beam splitter, these detector pairs do not detect coincident photons. The small numbers of these detected photon pairs are from imperfect mode matching of the photons on the beam splitter.

Detection of specific, identical photon pairs projects the atoms in to the state

$$|\Psi\rangle = |-1\rangle|+1\rangle + e^{-i(\Delta\omega\Delta t + 2\Delta\omega t' - \phi_D + \phi_0)}|+1\rangle|-1\rangle \quad (3.38)$$

where  $t'$  is the time elapsed following the detection of the second photon,  $\phi_D$  is 0 or  $\pi$  depending upon detection of the  $|\psi^\pm\rangle$  photonic Bell state, and  $\phi_0$  is a stable phase that depends on geometry [24]. The probability of two-photon collection and detection during the coincidence window  $T = 60$  ns is  $\sim 10^{-5}$ , resulting in a remote entanglement rate of order several per second.

In order to make the photon frequency difference  $\Delta\omega$  large, a large magnetic field difference could be applied to each atom. However, a minimum magnetic field must be applied to each atom to eliminate coherent dark states which reduce the efficiency of doppler cooling, state preparation, and state detection [23]. On the other hand, a large magnetic field which shifts the  $|\pm 1\rangle$  levels of order the excited

state transition linewidth complicates Doppler cooling, optical pumping, and state detection.

In order to maximize the photon frequency difference, a magnetic field of  $\sim 10$  Gauss is applied to both remote ions to induce a Zeeman shift of approximately  $2\pi \times 14$  MHz, and a half wave plate is inserted in the path of a photon from one ion trap to produce the state  $(|+1\rangle|V\rangle - i|-1\rangle|H\rangle) \otimes (|-1\rangle|V\rangle - i|+1\rangle|H\rangle)$ . Photons of identical polarization have a frequency difference of twice the Zeeman shift. Interference of these photons produces a significant number of photons with identical polarization exiting opposite ports of the beam splitter. The beating of the photon number statistics from these detector pairs projects the atoms into a remote product state. Detection of the photons of opposite polarization imprints the photon frequency difference to the remote atom entangled state phase and no beating of the photon number statistics is observed (see Eqn. 3.26). This behavior is shown in Fig. 3.11.

Upon coincident detection of non-identical photons, the remote ions are projected in to the entangled state

$$|\Phi\rangle = |-1\rangle|-1\rangle - e^{i(\Delta\omega\Delta t - 2\Delta\omega t' + \phi_D + \phi_0)}|+1\rangle|+1\rangle. \quad (3.39)$$

The resulting states in Eqn. 3.38 and Eqn. 3.39 can be analyzed with microwave rotations. Standard fluorescence techniques for state detection do not distinguish between the  $|-1\rangle$  and  $|+1\rangle$  states, so a microwave  $\pi$  pulse transfers any population in the  $|-1\rangle$  state to the  $|0\rangle$  state in both ion traps. Standard state dependent

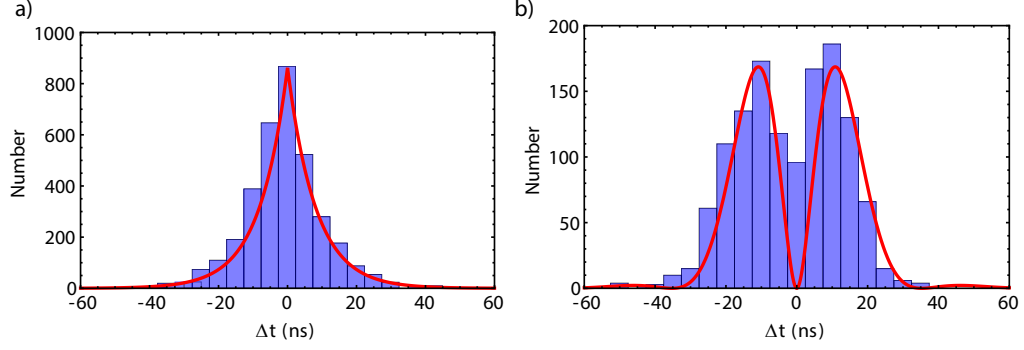


Figure 3.11: Photon statistics from interference of distinguishable photons entangled with a qubit. **(a)** Photon interarrival time for detector pairs measuring opposite polarization. The interarrival time of distinguishable photons is an exponential distribution because the photon beat frequency is imprinted on the entangled state of the remote atoms. No beating of the photon statistics are observed. The normalized fit is shown with no free parameters with characteristic decay time given by the atom excited state lifetime of  $\tau = 8.12\text{ns}$ . **(b)** Photon interarrival time for detector pairs measuring the same polarization. Because the photons have a frequency difference larger than  $1/\tau$ , beating of the photon interarrival time at the frequency difference is observed. If the photons were identical, these detector pairs would not register coincident detection. Coincident detection of photons with identical polarization exiting opposite detector ports heralds a non-entangled remote qubit state.

fluorescence can then determine the populations  $P_{|0,0\rangle}$ ,  $P_{|0,+1\rangle}$ ,  $P_{|+1,0\rangle}$ , and  $P_{|+1,+1\rangle}$ .

In order to determine the phase coherence of the entangled state, an additional analysis  $\pi/2$  microwave rotation is applied to each atom resonant with the  $|0\rangle \leftrightarrow | + 1\rangle$  transition after the first microwave transfer pulse. The phase of the analysis pulse on each atom is adjusted, and the probability the atoms are in an odd parity state  $P^o = P_{|0,+1\rangle} + P_{|+1,0\rangle}$  is measured using state-dependent fluorescence. In order to measure the coherences  $\rho_{|\Psi\rangle}$  and  $\rho_{|\Phi\rangle}$ , the amplitude of the odd parity oscillation of the remote state  $\Pi_{|i\rangle} = |\rho_{|i\rangle}|$ . The measured parity oscillations are fit to

$$\begin{aligned} P_{|\Psi\rangle}^o &= \frac{1}{2} - \Pi_{|\Psi\rangle} \cos(\phi_a - \phi_b + \Delta\omega\Delta t - \phi_d + \phi_0) \\ P_{|\Phi\rangle}^o &= \frac{1}{2} - \Pi_{|\Phi\rangle} \cos(\phi_a + \phi_b + \Delta\omega\Delta t - \phi_d - \phi_0). \end{aligned} \quad (3.40)$$



By choosing  $\phi_a = -\phi_b$  during the analysis pulse, we measure  $P_{|\Psi\rangle}^o$  and by choosing  $\phi_a = \phi_b$  during the analysis pulse, we measure  $P_{|\Phi\rangle}^o$ . The fidelity of the entangled states are  $F_\Psi = \langle \Psi | \rho | \Psi \rangle = \frac{1}{2}(P_{|0,+1\rangle} + P_{|+1,0\rangle}) + \Pi_{|\Psi\rangle}$  and  $F_\Phi = \langle \Phi | \rho | \Phi \rangle = \frac{1}{2}(P_{|0,0\rangle} + P_{|+1,+1\rangle}) + \Pi_{|\Phi\rangle}$

The entangled states using nearly identical and distinguishable photons are analyzed using PMTs with a temporal resolution of 1 ns and an electronics circuit with temporal resolution of 5 ns. With large but similar magnetic fields at both remote ions, the nearly identical photons have frequency difference of  $\Delta\omega = 2\pi \times 1.35$  MHz =  $0.068/\tau$ . With the half wave plate inserted, the distinguishable photons have frequency difference  $\Delta\omega = 2\pi \times 28.35$  MHz =  $1.45/\tau$ . We separate out the entanglement events by the photon interarrival time  $\Delta t$  recorded by the photon detection circuit and the odd parity probability  $P^o$  to measure the phase  $\phi' = \pm\Delta\omega\Delta t + \phi_0$  (see Eqn. 3.40). We calculate  $\Delta\omega$  from the slope of  $\phi'$  vs.  $\Delta t$  and average the  $\Delta\omega$  values measured for each detector pair phase  $\phi_D = 0, \pi$ . For the nearly identical photon case, we measure a photon mean frequency difference of  $\Delta\omega = 2\pi \times 1.4(2)$  MHz. For the distinguishable photon case, we measure a photon mean frequency difference of  $\Delta\omega = 2\pi \times 27.1(1.7)$  MHz, which agrees with the measured qubits splitting using microwave spectroscopy. The accrued phase also has the correct sign.

Averaging over the entangled state phase results in decoherence of the entangled state. To verify this behavior, the fidelity of the entangled state plotted for entanglement events  $\Delta t < \Delta t_{\max}$  where  $\Delta t_{\max} \leq T$  is a variable, maximum photon interarrival time (see Fig. 3.13). No significant phase evolution is expected for

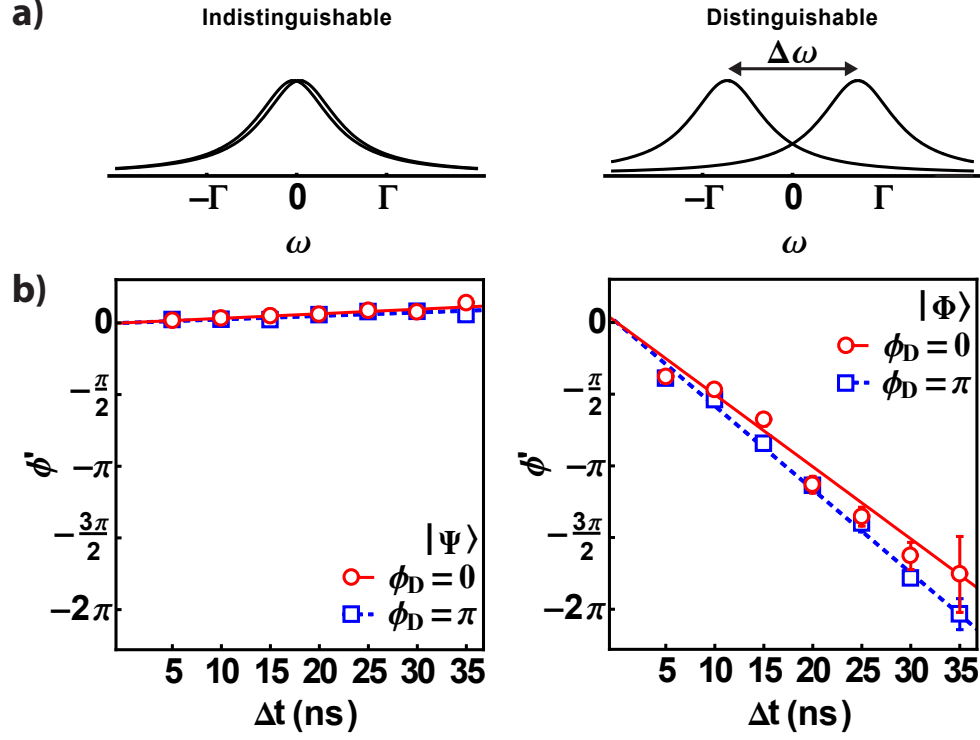


Figure 3.12: Phase evolution from interference of distinguishable photons. (a) Frequency lineshapes for indistinguishable ( $\Delta\omega = 2\pi \times 1.35$  MHz) and distinguishable photons ( $\Delta\omega = 2\pi \times 28.35$  MHz) with linewidth  $\Gamma = 1/\tau = 2\pi \times 19.6$  MHz. (b) Extracted time-dependent phase evolution of the entangled state as a function of photon interarrival time for heralding  $|\psi\rangle$  atom states with indistinguishable photons and for heralding  $|\Phi\rangle$  atom states with distinguishable photon interference. A fit to the data for each Bell state gives  $\Delta\omega = 2\pi \times 1.4(2)$  MHz and  $\Delta\omega = 2\pi \times 27.1(1.7)$  MHz. The entangled state phase has been offset in the figure so that  $\phi'(0) = 0$

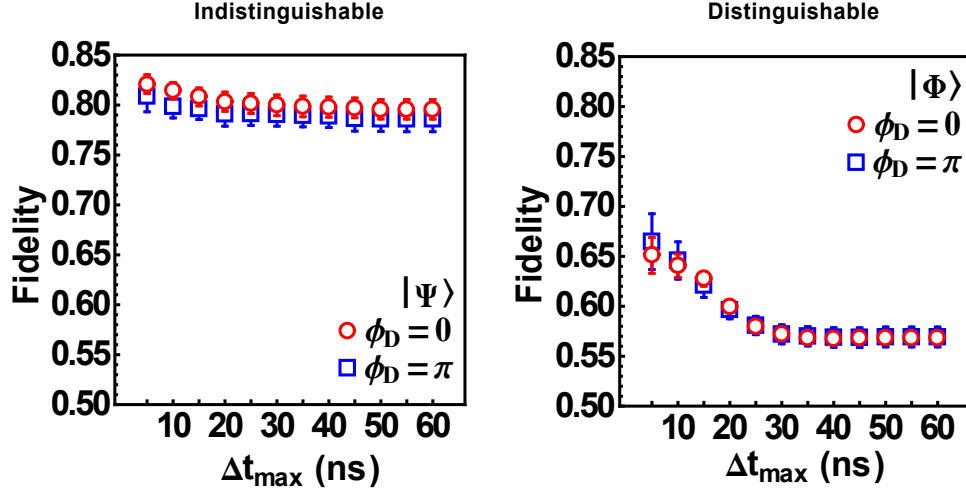


Figure 3.13: Remote atom fidelity using indistinguishable and distinguishable photon interference vs maximum time between photon detection events. For the indistinguishable case where the remote atom entangled state is  $|\Psi\rangle$ , the fidelity is nearly constant regardless of the time between detector clicks. For the distinguishable photon case, there is a clear increase in fidelity if photon coincidences  $\Delta t_{\max}$  less than  $2\pi/\Delta\omega \sim 35$  ns are accepted. The small time difference between detector pairs corresponds to minimal phase evolution of the remote atom state.

photons with frequency difference  $\Delta\omega \sim 1.4$  MHz, and the fidelity remains approximately constant over for  $0 < \Delta t_{\max} < T$ . However, the distinguishable photon case phase advances by  $2\pi$  for  $\Delta t = 2\pi/\Delta\omega \approx 35$  ns. Therefore, as  $\Delta t_{\max}$  increases, averaging out-of phase contributions to the entangled state coherence become significant and results in a low fidelity measurement.

This behavior can be seen in Fig. 3.13. The fidelity asymptotes to a value slightly higher than the mixed state value of 0.5 because most of the entanglement events occur with  $\Delta t \leq 10$  ns due to the exponential distribution of  $\Delta t$  from the atom lineshape. For  $\Delta t \leq 5$  ns, the measured fidelity of the  $|\Phi\rangle$  state does not reach the same level as  $|\Psi\rangle$  state for several reasons. The temporal resolution of the photon detection circuit contributes a few percent to the infidelity of the state.

In addition, the entangled  $|\Phi\rangle = |0\rangle|0\rangle + |+1\rangle|+1\rangle$  state is sensitive to common mode magnetic field noise. Lastly, we observe significant dephasing of single atom superposition states during the microwave transfer and analysis pulses owing to the magnetic field noise at high field from the magnetic field bias coils.

In order to set a constant entangled state phase on every experimental shot with sufficient photon detection bandwidth, either  $\Delta t_{\max}$  must be small or the photon interarrival time  $\Delta t$  must be used to feedforward a phase adjustment when measuring the remote entangled state [58]. By restricting  $\Delta t_{\max} \ll 2\pi/\Delta\omega$ , the maximum entangled state phase evolution is  $\Delta\omega\Delta t_{\max}$  but the entanglement rate slows exponentially. For example, by selecting  $\Delta t_{\max} = 5$  ns in the experiment presented here, the remote entanglement rate slows by a factor of 5. Alternatively, selecting the coincidence window  $T$  to be equal to the temporal resolution of the photon detection circuit slows the experimental entanglement rate by a factor of 14 [57].

Feeding forward the photon interarrival time with a known photon frequency difference completely eliminates the need for post-selection at the cost of increased overhead. In this experiment, the simplest method to convert the phase  $\Delta\omega\Delta t$  to a constant phase  $\phi_c$  consists of waiting a time  $t' = \frac{1}{2\Delta\omega}(\phi_c \pm \phi_D - \phi_0 - \Delta\omega\Delta t)$  following each remote entanglement event where plus (minus) sign is associated with heralding the  $|\Phi\rangle$  ( $|\Psi\rangle$ ) state. In the experiments presented here, the wait time would be  $\leq 18$  ns ( $\leq 370$  ns) for any photon interarrival time. Alternatively one could apply a stark shift to one of the atoms or the photon interarrival time  $\Delta t$  could simply be used to update the phase settings of any subsequent operations. These operations can be

accomplished many orders of magnitude faster than remote entanglement rates [20], but high temporal resolution may still be needed to track the phase evolution of the remote atom state  $2\Delta\omega t'$  (see Eq. 3.38, 3.39).

We post-process the entangled  $|\Phi\rangle$  state for  $\phi_D = \pi$  by shifting the phase of the parity oscillation for each photon interarrival time bin. Since the photon difference frequency is known from spectroscopy analyzing the qubits, the phase shift  $\Delta\omega\Delta t$  is known. The phase is shifted by  $\phi_a + \phi_b \rightarrow \phi_a + \phi_b + \Delta\omega\Delta t$ . After shifting the incoherent parity oscillations  $P_{|\Phi\rangle}^o$  (See Fig. 3.14a) by the known phase shift, the parity oscillations are clearly in phase, as is shown in Fig. 3.14b, for any photon interarrival time of the distinguishable photons. The resulting fidelity as a function of  $\Delta t_{\max}$  is shown in Fig. 3.14c. Without the phase shift, the fidelity of the  $|\Phi\rangle$  state decreases. Application of the known phase shift clearly increases the fidelity of the entangled state without sacrificing the remote entanglement rate.

Using this time-resolved photon detection technique to generate entanglement between non-identical emitters has a number of potential applications. These techniques can be applied to a heterogeneous quantum network or other modular quantum network constructed with non-identical components or whose components differ because of their local environment. Single photon detectors with timing jitter of order 10 ps are currently available as are stable oscillators and fast circuitry with bandwidths of order 10 GHz. Utilizing these technologies, photons with identical lineshapes with frequency difference of order 1 GHz could be used to generate high-quality entanglement without sacrificing entanglement rate. In addition, if faster detectors can be realized, qubits of differing physical origin, such as trapped ions

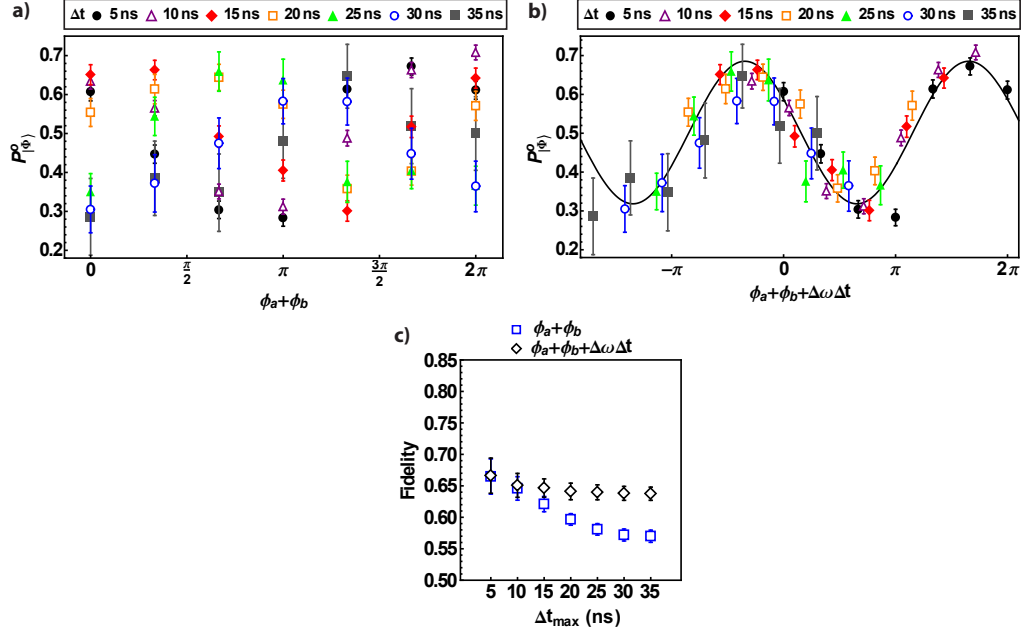


Figure 3.14: Phase coherence of remote entangled atoms using interference of distinguishable photons. **(a)** Probability of detecting odd parity as a function of the phase of the final  $\pi/2$  microwave pulse for varying photon interarrival times  $\Delta t$ . The time dependent phase shift of the atom state at the photon frequency difference shifts the phase of the parity oscillations by  $\Delta\omega\Delta t$ . The sinusoids are incoherent because of the time-dependent phase shift, so averaging over these phase shifts is decoherence of the atomic remote entangled state. **(b)** We post process the entangled state phase by shifting the phases of the analysis  $\pi/2$  pulses  $\phi_a + \phi_b \rightarrow \phi_a + \phi_b + \Delta\omega\Delta t$  using the experimentally measure photon frequency difference  $\Delta\omega$  and photon interarrival time difference  $\Delta t$ . The resulting parity oscillations are in phase. **(c)** Fidelity of the remote entangled state averaging over photon interarrival times and the post-processed data with applied phase shifts. The loss of fidelity is significantly reduced by tracking the known phase shift from the interference of distinguishable photons without sacrificing remote entanglement rate.

and quantum dots or NV centers, may entangled using the interference of distinguishable photons.

## Chapter 4: **Phonon entanglement of proximate trapped ion qubits**

### 4.1 **Entanglement between interacting trapped ions with raman lasers**

Ions confined in close proximity to each other in the same ion trap interact via the Coulomb force, resulting in normal modes of motion with anomalous dispersion. In addition to changing the spin state of the ions, as discussed in Chapter 2, Raman processes can change the spin state of the ions and raise or lower the phonon number of the modes of motion. The interaction between the spin of the ions and their normal modes of motion allows for Raman lasers to impart spin dependent forces which can result in creating entanglement between two ions. This brief section is meant to provide an overview of this type of entanglement and follows from a synthesis of more complete material presented in [76–79].

The following treatment will also assume continuous wave (CW) optical fields even though a frequency comb was used to obtain the experimental results shown in this chapter. The use of a frequency comb is not very different from the use of CW lasers for Raman interactions because the frequency difference of the lasers



determines which Raman transition is driven in a three-level,  $\lambda$ -system. Although the Rabi frequency of the transitions are modified slightly [79, 80], a frequency comb may be viewed as a collection of phase coherent, CW lasers that add in phase to drive Raman processes.

Two optical fields  $\mathbf{E}_L(\mathbf{r}) = E_L(\mathbf{r}) \cos(\mathbf{k}_L \cdot \mathbf{r} - \omega_L t - \phi_L) \epsilon_L$  with index  $L = \alpha, \beta$  and polarization  $\epsilon_L$  drive transitions between qubit states  $|0\rangle$  and  $|1\rangle$  by coupling to an excited state  $|e\rangle$ . Note that more than one excited state is actually involved, and summing over the excited states is important for computing the Rabi frequency. The optical fields have difference  $\omega_\beta - \omega_\alpha = \omega_{HF} + \delta\omega$  where the frequency  $\delta\omega$  can be scanned using an AOM. The lasers are assumed to be detuned by an amount  $\Delta = \omega_e - \omega_{\alpha,\beta}$  and the value of the electric field is evaluated at the ion position  $\mathbf{r}$ .

The atom-laser interaction can be transformed in to the rotating frame at the laser frequency  $\omega_\alpha$ , and after making the rotating wave approximation and transforming into the interaction picture, the interaction Hamiltonian is [77]

$$\begin{aligned}
H_I = & \frac{1}{2} \left( g_{1,\alpha} e^{i\mathbf{k}_\alpha \cdot \mathbf{r} - i\phi_\alpha} |e\rangle \langle 1| + \text{h.c} \right. \\
& \left. + g_{0,\beta} e^{i\mathbf{k}_\beta \cdot \mathbf{r} - i\phi_\beta} e^{-i\Delta\omega t} |e\rangle \langle 0| + \text{h.c} + \Delta |e\rangle \langle e| \right)
\end{aligned} \tag{4.1}$$

where the single photon Rabi frequency  $g_{0,L} = -\mu_L \cdot \epsilon_L E_L / 2$ . Since the detuning is large compared to the excited state linewidth, spontaneous emission will be neglected and the excited state can be adiabatically eliminated (see the appendix of [78]). The rotating wave approximation may be applied again at the qubit frequency difference

$\omega_{HF}$ , resulting in

$$\begin{aligned}
H_I &= \frac{1}{2} \left( \Omega e^{-i\Delta\mathbf{k}\cdot\mathbf{r} - \delta\omega t - \Delta\phi} |1\rangle\langle 0| + \text{h.c.} \right) \\
&+ \chi_0 |0\rangle\langle 0| + \chi_1 |1\rangle\langle 1|
\end{aligned} \tag{4.2}$$

with  $\Delta\mathbf{k} = \mathbf{k}_\beta - \mathbf{k}_\alpha$  and  $\Delta\phi = \phi_\beta - \phi_\alpha$  are the phase differences of the two optical fields and  $\Omega$  is the Rabi frequency. The stark shift  $\chi_0$  and  $\chi_1$  will be neglected since the differential stark shift of the  $^{171}\text{Yb}^+$  qubit levels from a laser at 355 nm is of order  $10^{-4}\Omega$  [28].

If there are only two ions ( $i = 1, 2$ ), it is possible to couple to four transverse modes of motion: the symmetric center of mass mode and the anti-symmetric mode along the two transverse directions to the ion chain. For simplicity, assume the  $\Delta\mathbf{k}$  vector points along only one transverse mode direction so only two transverse modes  $\omega_{1,2}$  are addressed by the optical fields. In the interaction frame of the vibrational modes, the interaction Hamiltonian is

$$\begin{aligned}
H_I &= \frac{1}{2} \sum_{i=1,2} \left[ \left( \Omega_i e^{-i[\eta_1(a_1 e^{-i\omega_1 t} + a_1^\dagger e^{i\omega_1 t}) \pm \eta_2(a_2 e^{-i\omega_2 t} + a_2^\dagger e^{i\omega_2 t})]} \right. \right. \\
&\times \left. \left. e^{i\Delta\omega t} e^{-i(\Delta\mathbf{k}\cdot\mathbf{X}_{0,i} - \Delta\phi)} |1\rangle\langle 0| + \text{h.c.} \right) + \chi_{0,i} |0\rangle\langle 0| + \chi_{1,i} |1\rangle\langle 1| \right] \tag{4.3}
\end{aligned}$$

The optical phase  $\Delta\phi = \phi_\alpha - \phi_\beta$  is the phase difference between the two Raman laser fields. If the lasers are from a single laser, fluctuations in the optical phase of the laser are common mode, fluctuations of the absolute optical phase of the laser from shot to shot will not decohere the quantum state. However, the phase

$\Delta \mathbf{k} \cdot \mathbf{X}_{0,1}$  is sensitive to path length differences of order the optical wavelength for non-copropagating laser geometries, as is typical with entangling gates that address the ion modes of motion. Stabilizing this phase requires interferometric stability. In most ion trap experiments with gate times of order 100  $\mu\text{s}$ , this phase is passively stable for a single experimental shot. In a modular quantum system, each ion trap module may have phase fluctuations relative to other modules on each experimental shot, resulting in decoherence if the wavefunction is delocalized over many modules. Overcoming this issue with absolute phase control is addressed in the next section of Chapter 4 and in [81].

If the optical fields have sufficiently low intensity such that the Rabi frequency is less than the trap frequency, the difference frequency of the laser can be tuned to address Raman transitions in the resolved sideband limit [76]. These transitions are the “carrier” transition, where the  $|0\rangle \leftrightarrow |1\rangle$  transition is addressed, and the red and blue sidebands, where the qubit state is changed and a phonon is subtracted or added to a mode of motion. When the frequency difference of the optical fields is tuned near the qubit frequency difference  $\omega_{HF}$ , the carrier interaction Hamiltonian is

$$H_I^{\text{carr}} = \frac{1}{2} \sum_{i=1,2} \sum_{n_1, n_2} \left( \Omega_i \mathcal{D}_{n_1, n_2} e^{i(\Delta \mathbf{k} \cdot \mathbf{X}_{0,i} - \Delta \phi)} \sigma_+^{(i)} + \text{h.c.} \right) \times |n_1, n_2\rangle \langle n_1, n_2| \quad (4.4)$$

where  $\sigma_+ = |1\rangle \langle 1|$ ,  $\sigma_- = |0\rangle \langle 1| = \sigma_+^\dagger$ . The Debye-Waller factor  $\mathcal{D}_{n_1, n_2}$  exponentially suppresses the carrier coupling due to the ion motion with quantum number  $n_\nu$  and is equal to  $\mathcal{D}_{n_1, n_2} = e^{-\frac{1}{2}(\eta_1^2 + \eta_2^2)} \mathcal{L}_{n_1}(\eta_1^2) \mathcal{L}_{n_2}(\eta_2^2)$ .  $\mathcal{L}_{n_\nu}(\eta_i^2)$  is a Laguerre polynomial of

order  $n_\eta$  [76]. When the ions are well within the Lamb-Dicke limit,  $\mathcal{D}_{n_1, n_2} \approx 1$ . In a copropagating laser geometry, the Lamb Dicke parameter is very small, fixing  $\mathcal{D} \approx 1$ .

When the difference frequency of the optical fields is tuned so that  $\omega_\beta - \omega_\alpha = \omega_{HF} - \omega_\nu$ , the atom is rotated from  $|0\rangle \rightarrow |1\rangle$  and the collective mode of motion is lowered by one quanta:

$$H_I^{\text{RSB}} = \frac{1}{2} \sum_{i=1,2} \eta_\nu \Omega_i \mathcal{D}_{n_\nu, n_{\nu'}} e^{i(\Delta \mathbf{k} \cdot \mathbf{X}_{0,i} - \Delta \phi)} \sigma_+^{(i)} a_\nu + \text{h.c.} \quad (4.5)$$

This red sideband interaction couples the state  $|0, n_\nu\rangle$  to  $|1, n_\nu - 1\rangle$  where the Debye-Waller factor  $\mathcal{D}_{n_\nu, n_{\nu'}}$  for the first sideband where  $\nu \neq \nu'$  [76, 77]. This Hamiltonian is a two-qubit version of the Jaynes-Cummings Hamiltonian.

When the optical field frequency difference is tuned to  $\omega_\beta - \omega_\alpha = \omega_{HF} + \omega_\nu$ , the blue sideband interaction Hamiltonian is

$$H_I^{\text{BSB}} = \frac{1}{2} \sum_{i=1,2} \eta_\nu \Omega_i \mathcal{D}_{n_\nu, n_{\nu'}} e^{i(\Delta \mathbf{k} \cdot \mathbf{X}_{0,i} - \Delta \phi)} \sigma_+^{(i)} a_\nu^\dagger + \text{h.c.} \quad (4.6)$$

where the atom is rotated from the  $|0\rangle \rightarrow |1\rangle$  state while adding one quanta to a collective mode of motion:  $|0, n_\nu\rangle \rightarrow |1, n_\nu + 1\rangle$ . This Hamiltonian is a two-qubit version of the anti-Jaynes-Cummings Hamiltonian.

The Mølmer-Sørensen interaction makes use of two laser frequency beat notes. The blue sideband is addressed off resonantly with a detuning  $+\delta$  while the red sideband is addressed off resonantly with a detuning  $-\delta$ . Both sidebands have equal

intensity on both ions  $\nu\Omega$ . Typically, the coupling is to the anti-symmetric mode due to the lower heating rate [77], denoted by  $\omega_2$ . The interaction Hamiltonian is the sum of the red and blue sidebands

$$\begin{aligned}
H_I = & \frac{1}{2} \sum_{i=1,2} \eta_2 \Omega_i \mathcal{D}_{n_2, n'_2} \left( e^{i(\Delta \mathbf{k}_r \cdot \mathbf{X}_{0,i} - \Delta \phi_r)} \sigma_+^{(i)} a_2 e^{-i\delta t} \right. \\
& \left. + e^{i(\Delta \mathbf{k}_b \cdot \mathbf{X}_{0,i} - \phi_b)} \sigma_+^{(i)} a_2^\dagger e^{i\delta t} + \text{h.c.} \right)
\end{aligned} \tag{4.7}$$

where the sideband Rabi frequency is  $\eta_2 \Omega$  and the phase factors depend on the k-vector differences of the red sideband lasers and the k-vector difference of the blue sideband lasers. Note that these two k-vector differences is an optical k-vector because each k-vector difference results from non-copropagating lasers. This equation can be simplified for one ion:

$$H_{ms}(t) = -i \frac{\eta \Omega}{2} (\sigma_+ e^{i\phi_s} - \sigma_- e^{-i\phi_s}) (a e^{-i\delta t} e^{i\phi_m} + a^\dagger e^{i\delta t} e^{-i\phi_m}) \tag{4.8}$$

where the spin phase is  $\phi_s = (\phi_r + \phi_b)/2$  and the motional phase is  $\phi_m = (\phi_r - \phi_b)/2$ . The spin phase is  $\phi_{S,i} = -(\Delta \mathbf{k}_r \cdot \mathbf{X}_{0,i} - \Delta \phi_r + \Delta \mathbf{k}_b \cdot \mathbf{X}_{0,i} - \Delta \phi_b)/2$  and the motion phase is  $\phi_{M,i} = (\Delta \mathbf{k}_r \cdot \mathbf{X}_{0,i} - \Delta \phi_r - \Delta \mathbf{k}_b \cdot \mathbf{X}_{0,i} + \Delta \phi_b)/2$ .

The time evolution of this Hamiltonian can be computed by making use of the time evolution operator. Since the Hamiltonian is time-dependent, the Magnus-expansion must be used. In general, this expansion is infinite, but because the commutator of harmonic oscillator raising and lowering operators is a complex number, this infinite series terminates at second order. The time evolution operator to second

order is

$$U(t, 0) = \exp \left[ \sum_k \hat{O}_k \right] \quad (4.9)$$

$$\hat{O}_1 = -\frac{i}{\hbar} \int_0^t dt' H(t') \quad (4.10)$$

$$\hat{O}_2 = -\frac{1}{2\hbar^2} \int_0^t \int_0^{t'} dt' dt'' [H(t'), H(t'')]. \quad (4.11)$$

Defining the spin operator  $\hat{S} \equiv -i(\sigma_+ e^{i\phi_s} - \sigma_- e^{-i\phi_s})$ , the first term in the Magnus expansion is

$$\begin{aligned} \hat{O}_1 &= \frac{\eta\Omega}{2} \hat{S} \int_0^t dt' \left( a e^{-i\delta t'} e^{i\phi_m} + a^\dagger e^{i\delta t'} e^{-i\phi_m} \right) \\ &= \hat{S} (\alpha(t) a^\dagger - \alpha^*(t) a) \end{aligned} \quad (4.12)$$

$$\alpha(t) = \frac{\eta\Omega}{2} \frac{e^{i\delta t}}{i\delta} e^{-i\phi_m}. \quad (4.13)$$

The second term in the Magnus expansion is

$$\begin{aligned} \hat{O}_2 &= -\frac{1}{2} \int_0^t \int_0^{t'} dt'' dt' [H(t'), H(t'')] \\ &= -\frac{1}{2} \left( \frac{\eta\Omega}{2} \right)^2 \hat{S}^2 \int_0^t \int_0^{t'} dt'' dt' (e^{-i\delta(t'-t'')} - e^{i\delta(t'-t'')}) \\ &= -\left( \frac{\eta\Omega}{2} \right)^2 \frac{1}{i\delta} \left( t - \frac{\sin(\delta t)}{\delta} \right) \hat{S}^2, \end{aligned} \quad (4.14)$$

with the resulting the time evolution operator

$$U_{ms}(t) = \exp \left[ \hat{S}(\alpha^*(t)a^\dagger - \alpha(t)a) + i\hat{S}^2\Phi_0(t) \right] \quad (4.15)$$

$$\Phi_0(t) \equiv - \left( \frac{\eta\Omega}{2\delta} \right)^2 \left( \delta t - \sin(\delta t) \right) \quad (4.16)$$

$$\alpha(t) = \frac{\eta\Omega}{2} \frac{e^{i\delta t}}{i\delta} e^{-i\phi_m}. \quad (4.17)$$

The Mølmer-Sørensen operation is a spin dependent force. This can be seen by expressing the spin operator in its eigenbasis and computing the time dependence of a state such as  $|0, \beta\rangle$  where  $\beta$  describes the motional state of the atomic ion. The spin operator  $\hat{S} = -i(\sigma_+ e^{i\phi_s} - \sigma_- e^{-i\phi_s})$  has eigenstates  $\frac{1}{\sqrt{2}}(\pm i e^{-i\phi_s}|0\rangle + |1\rangle)$ , denoted  $|\uparrow_{\phi_s}\rangle$  and  $|\downarrow_{\phi_s}\rangle$ , with eigenvalues  $\pm 1$ . The time evolution operator in this basis is

$$U_{MS}(t) = \exp \left[ (\alpha^*(t)a^\dagger - \alpha(t)a)(|\uparrow_{\phi_s}\rangle\langle\uparrow_{\phi_s}| - |\downarrow_{\phi_s}\rangle\langle\downarrow_{\phi_s}|) \right. \\ \left. + i\Phi_0(t)(|\uparrow_{\phi_s}\rangle\langle\uparrow_{\phi_s}| + |\downarrow_{\phi_s}\rangle\langle\downarrow_{\phi_s}|) \right], \quad (4.18)$$

and its action on the state  $|0, \beta\rangle$  is,

$$U_{MS}(t)|\downarrow_z, \beta\rangle = U_{MS}(t) \left( -ie^{i\phi_s}|\uparrow_{\phi_s}, \beta\rangle + ie^{i\phi_s}|\downarrow_{\phi_s}, \beta\rangle \right) / \sqrt{2} \quad (4.19)$$

$$= -\frac{i}{\sqrt{2}} e^{i\Phi_0(t)} e^{i\phi_s} \left( \hat{D}(\alpha(t))|\uparrow_{\phi_s}, \beta\rangle \right. \\ \left. - \hat{D}(-\alpha(t))|\downarrow_{\phi_s}, \beta\rangle \right) / \sqrt{2}, \quad (4.20)$$

with displacement operator  $\hat{D}(\alpha(t)) = \exp[\alpha^*(t)a^\dagger - \alpha(t)a]$ . The displacement operator in the coherent state basis is  $|\beta\rangle = \hat{D}(\beta)|0\rangle$  where  $|0\rangle$  is the ground state

of a quantum harmonic oscillator. For a single ion, the phase  $\Phi_0 + \phi_s$  is a global phase and can be ignored. Using the identity,  $\hat{D}(\alpha)\hat{D}(\beta) = e^{i\varphi_{\alpha,\beta}}\hat{D}(\alpha + \beta)$ , where  $\varphi_{\alpha,\beta} \equiv \text{Im}[\alpha\beta^*]$

$$U_{ms}(t)|\downarrow_z, \beta\rangle = \frac{1}{\sqrt{2}}(e^{i\varphi_{\alpha,\beta}}|\uparrow_{\phi_s}, \beta + \alpha(t)\rangle - e^{-i\varphi_{\alpha,\beta}}|\downarrow_{\phi_s}, \beta - \alpha(t)\rangle). \quad (4.21)$$

The Mølmer-Sørensen interaction becomes clear; an ion prepared in the state  $|0\rangle$  is a superposition of states in the  $\{|\uparrow_{\phi_s}\rangle, |\downarrow_{\phi_s}\rangle\}$  basis. These states are displaced by equal but opposite amounts  $|\pm\alpha(t)\rangle$  in phase space. The phase space closes when the detuning from the sidebands of motion  $\delta = 2\eta\Omega$  after time  $t = 2\pi/\delta$ . This treatment can easily be extended to two ions where the Mølmer-Sørensen Hamiltonian is

$$H_{ms}^{(2)} = -i\frac{\eta\Omega}{2}(\Sigma_+e^{i\phi_s} - \Sigma_-e^{-i\phi_s})(ae^{-i\delta t}e^{i\phi_m} + a^\dagger e^{i\delta t}e^{-i\phi_m}), \quad (4.22)$$

where  $\Sigma_\pm \equiv \sigma_\pm^{(1)} + \sigma_\pm^{(2)}$  is the total spin operator. If the atoms are prepared in the state  $|00\rangle$ , and the gate time is fixed so the phase space trajectories close at the end of the gate operation, the state evolves as

$$U_{ms}(t)|00\rangle = e^{i\hat{S}^2\Phi_0(t)}\frac{(|\downarrow\downarrow_{\phi_s}\rangle + |\uparrow\uparrow_{\phi_s}\rangle - |\downarrow\uparrow_{\phi_s}\rangle - |\uparrow\downarrow_{\phi_s}\rangle)}{2} \quad (4.23)$$

$$= \frac{e^{i4\Phi_0(t)}(|\downarrow\downarrow_{\phi_s}\rangle + |\uparrow\uparrow_{\phi_s}\rangle - |\downarrow\uparrow_{\phi_s}\rangle - |\uparrow\downarrow_{\phi_s}\rangle)}{2}. \quad (4.24)$$

With gate time and laser detuning  $t_g = \frac{2\pi}{\delta} = 2\eta\Omega$ , the phase is  $e^{i4\Phi_0(t_g)} = -i$  and



the final state is the maximally entangled state,

$$U_{ms}(t_g)|00\rangle = e^{-i\pi/4} \frac{|00\rangle - ie^{i2\phi_{ms}}|11\rangle}{\sqrt{2}}. \quad (4.25)$$

## 4.2 Quantum gates with absolute phase stability

In a quantum information processor, the control and entanglement of quantum bits is usually accomplished with external electromagnetic fields, whose phase is directly imprinted on the qubits [82]. Generating large-scale entanglement for applications in quantum information science therefore relies upon the spatial and temporal coherence of phases throughout the system. As the system grows in complexity to many qubits and many quantum gate operations, likely requiring a modular architecture [17], it will become crucial to control and coordinate the phases between modules and between qubits within a module. In one module, the start of every experiment defines the equatorial axes on the Bloch sphere; the start of a single experiment defines zero phase. In most ion trapping experiments to date, path length fluctuations on time scales longer than a single experiment are unimportant. However, in a modular architecture composed of many modules where qubits are manipulated with optical fields, and the resulting optical phase differences at each module define different phases at each module at the start of each experiment. Averaging over these phases differences between modules over many experiments results in decoherence of a quantum state spread out between modules. It is possible to set up interferometers at each node between modules to ensure relative optical

phase stability between modules, but appropriate choice of laser geometry and the distribution of a reference clock signal obviates the need for optical phase stability, resulting in absolute phase control in a modular system [81].

We restrict the consideration of designing an absolute phase control system where to qubit states with RF or microwave frequency splittings, as opposed to optical qubit splittings which require absolute optical phase stability [83]. In a quantum information processing systems, qubits are sensitive to the absolute qubit phase evolution, and thus optical qubits will require controlling the absolute optical phase of the control fields. Absolute phase control in the RF or microwave regime can be accomplished with commercially available electronics, and phase fluctuations from changes in control field path lengths are passively stable on microwave and RF wavelength scales. We demonstrate the absolute control of qubit phases in both space and time using a collection of trapped atomic ion qubits driven by optical fields. We choose appropriate laser beam geometries that eliminate the dependence of qubit phases on absolute optical path lengths from the driving field, and we use a common high quality master oscillator as a reference for all operations. These techniques are applicable to many other quantum computing platforms such as NV-centers in diamond [84], optical quantum dots [85], and optical lattices containing neutral atoms [86].

We use qubits encoded in the hyperfine clock states of trapped  $^{171}\text{Yb}^+$  atoms  $|F = 0, m_F = 0\rangle \equiv |0\rangle$  and  $|F = 1, m_F = 0\rangle \equiv |1\rangle$  of the  $^2S_{1/2}$  manifold with a hyperfine splitting of  $\omega_0/2\pi = \nu_0 = 12.64282$  GHz. Standard photon scattering methods are used for Doppler cooling, state initialization and detection [22].

The qubit state can be rotated between  $|0\rangle$  and  $|1\rangle$  with optical or microwave fields, and we demonstrate phase coherence between these fields by using them sequentially on a qubit. The use of continuous-wave (CW) lasers is technically difficult for systems with qubit splittings more than a few GHz since it requires phase-locking two monochromatic sources or the use of modulators with limited bandwidths. Alternatively, the large bandwidths of ultrafast laser pulses easily spans such splittings [80]. We use a mode-locked 355 nm ( $\nu_{PL} \approx 844.48$  THz) pulsed laser with repetition rate  $\nu_r$  for driving stimulated Raman transitions by using a copropagating geometry [76]. An acousto-optic modulator (AOM B) is driven with frequencies  $\nu_{B,1}$ ,  $\nu_{B,2}$  that are adjusted to bring the beat-note between the copropagating Raman beams on resonance with the qubit hyperfine splitting (Fig. 4.1a):

$$\nu_0 = p\nu_r + \nu_{B,1} - \nu_{B,2} \quad (4.26)$$

where  $p$  is an integer. Due to atomic selection rules, transitions may be driven when the two beams have the same circular polarization. The use of optical fields to drive rotations and create entanglement between qubits imprints an optical phase on the quantum states. In two-photon Raman processes, the imprinted phase is equal to the k-vector difference of the lasers (multiplied by the qubit position  $x_0$ ) that drive the process. Since these beams from AOM B are nominally copropagating, drifts of the path length on length scales of order the optical wavelength are nearly common mode, result in negligible phase errors on the qubit.

In order to stabilize the remaining phase resulting from the frequency difference

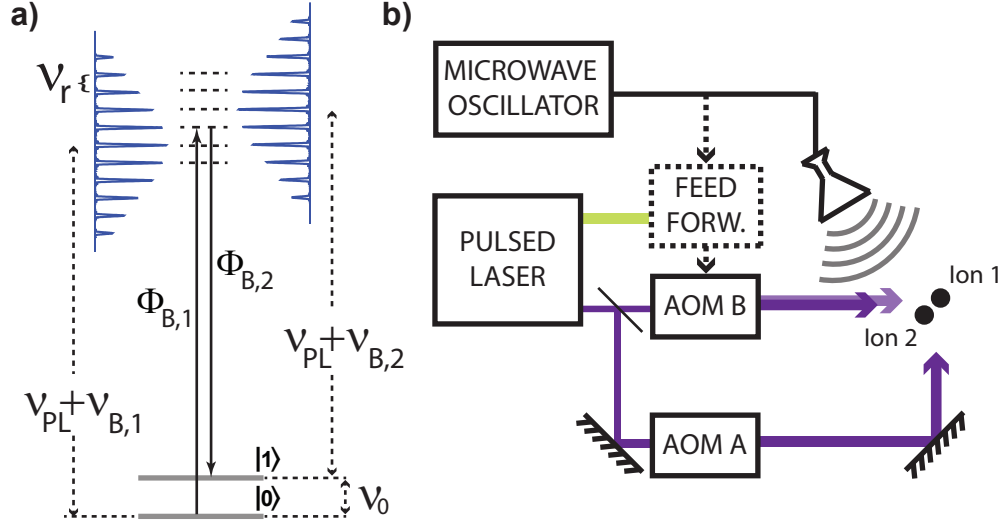


Figure 4.1: Simplified diagram for absolute phase control in a modular quantum system. **a)** The qubit is driven from atomic levels  $|0\rangle$  to  $|1\rangle$  via two-photon stimulated Raman process by absorbing from the  $\nu_{B,1}$  comb and emitting into the  $\nu_{B,2}$  comb. The phase written to the qubit in this transition is  $\Phi_{B,1} - \Phi_{B,2}$ , where  $\Phi_{B,1}$  and  $\Phi_{B,2}$  are the optical phases of the two combs at the ion position. The inverse process from  $|1\rangle$  to  $|0\rangle$  reverses these phases. This coherent transition can also be driven directly with microwaves at frequency  $\nu_0$ . **b)** Simplified experimental diagram. The master microwave oscillator and pulsed laser repetition rate are locked through a feed-forward system. Acousto-optic modulator (AOM) B is used for copropagating transitions, and AOM A is used in conjunction with AOM B for multi-qubit entangling gates.

of the co-propagating laser beams, we feed-forward fluctuations in the measured repetition rate of the pulsed laser to AOM B an external master oscillator (see Fig. 4.1b) [87]. This oscillator serves as a clock for referencing phases upon rotations and entangling gates in a modular system. By distributing this clock signal in a modular architecture, absolute phase control across a modular architecture is possible. In addition, this feed-forward technique may be more useful than directly stabilizing the laser cavity length because of the limited bandwidth of mechanical transducers and the possible inaccessibility of the laser cavity. Locking the beatnote of a mode-locked pulsed laser at microwave frequencies was accomplished by measuring the laser intensity with a fast photodiode. The electrical signal is amplified and beat against a microwave oscillator. The resulting beat note could be low passed and fed directly in to an oscillator controlling the frequency of an AOM, but bandwidth limitations of available phase locked loops results in significant phase noise on qubit operations. The microwave oscillator is therefore detuned from the qubit frequency by the desired AOM frequency, and an additional phase lock loop is added. Addition of this phase lock loop reduces the fractional spectral noise density of the optical power to  $\sim -120$  dB/Hz [87], resulting in a coherence time between the  $^{171}\text{Yb}^+$  qubit and laser beatnote of greater than 1 second.

The insensitivity co-propagating Raman transitions to differential path length fluctuations may be demonstrated by performing a Ramsey experiment on the qubit with one  $\pi/2$  pulse from the laser and the second  $\pi/2$  pulse from a relatively long-wavelength microwave source. Since the microwave oscillator serves as the reference clock in the laser-beatnote stabilization circuit, the microwave and laser  $\pi/2$  pulses

should be in phase with each other over long time scales in the absence of any dependence on the optical phase. Fig. 4.2 demonstrates the phase coherence between the laser and microwaves over long time scales compared to typical qubit operations. With this scheme, microwaves can be used for global qubit rotations, while focused Raman beams can address individual qubits in a long chain for single qubit rotations.

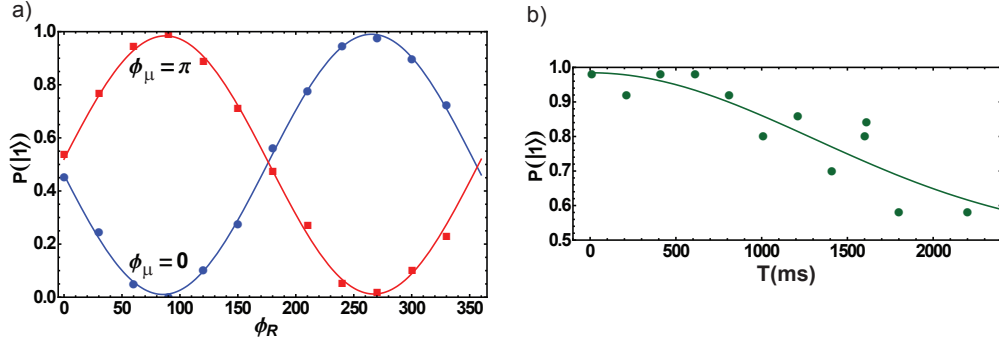


Figure 4.2: Optical phase insensitivity of copropagating Raman transitions. **(a)** A Ramsey experiment with a  $\pi/2$  microwave pulse followed by a  $\pi/2$  copropagating Raman pulse with variable phase. The two curves show the microwave phase set to  $\phi_\mu = 0, \pi$  and the Raman laser phase  $\phi_R$  is scanned. The microwave and Raman lasers are phase coherent because the state of the qubit can be controlled by the phase of either the microwaves or the laser. **(b)** With the microwave and laser phases set so the qubit state is  $|1\rangle$ , the time delay between  $\pi/2$  rotations is varied. A Gaussian fit to the data gives a  $1/e$  time of 1.8 seconds, demonstrating phase coherence between the microwaves and Raman lasers over long time periods.

### 4.2.1 Multi-qubit entangling gates

Entangling trapped atomic qubits through their Coulomb interaction requires external field gradients that provide state-dependent forces. The absolute phase and amplitude of microwave or RF fields can easily be controlled for this purpose, but generating sufficiently high field gradients requires specialized trap geometries

and high currents [88]. Instead, optical fields can be used where non-copropagating Raman beams are required to generate large field gradients [8, 89, 90].

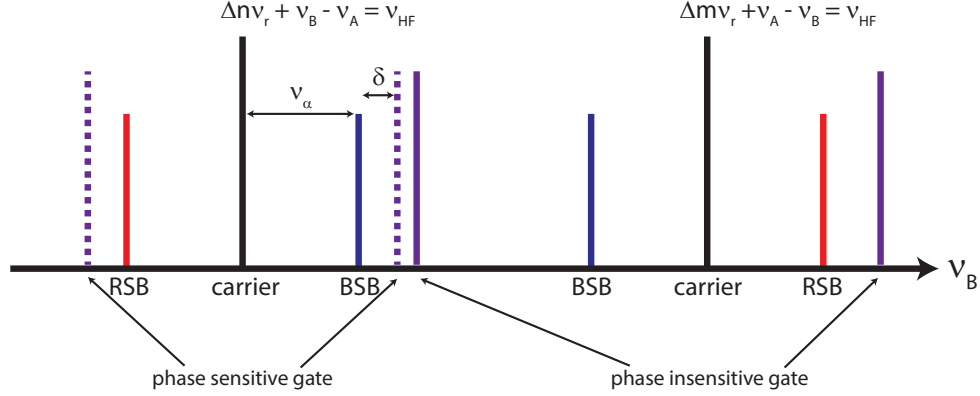


Figure 4.3: Raman spectrum diagram for phase sensitive and phase insensitive entangling gates. The diagram shows only a single collective mode of motion for simplicity. There are two carrier ( $|0\rangle|n\rangle \rightarrow |1\rangle|n\rangle$ ) transitions shown, corresponding to two different Raman transitions  $(n_B\nu_r + \nu_B) - (n_A\nu_r + \nu_A) = \Delta n\nu_r + \nu_B - \nu_A = \nu_{HF}$  and  $(m_A\nu_r + \nu_A) - (m_B\nu_r + \nu_B) = \Delta m\nu_r + \nu_A - \nu_B = \nu_{HF}$  with  $\nu_{A,B}$  corresponding to the frequencies applied to AOM A,B and directing the positive diffracted order on to the atom (see Fig. 4.1b). By applying two frequencies to AOM B, the red and blue sidebands of motion (RSB, BSB) may be addressed with detuning  $\delta$ , depicted as dotted purple lines in the figure. This frequency configuration corresponds to an entangling gate where the entangled state phase retains sensitivity to the optical phase of the Raman lasers. If the frequency configuration shown by the solid purple lines are used to perform an entangling gate, the resulting entangled state phase is not sensitive to the optical phase of the Raman laser.

We utilize a particular geometry of non-copropagating beams to realize gates insensitive to the optical phase of the laser beams. Such gates have been demonstrated on magnetic field sensitive states [91]; however, their susceptibility to magnetic field noise results in shorter coherence times compared to clock states. Phase insensitive gates on clock states have been realized with CW lasers to provide a state-dependent force by addressing both red and blue sideband transitions;  $|0\rangle|n\rangle \rightarrow |1\rangle|n-1\rangle$  and  $|0\rangle|n\rangle \rightarrow |1\rangle|n+1\rangle$  respectively where  $|n\rangle$  is the vibrational eigenstate of the ions in a harmonic trap potential [76, 77, 92]. This has also been accomplished

by simultaneously driving a carrier,  $|0\rangle|n\rangle \rightarrow |1\rangle|n\rangle$ , and a single sideband transition [93, 94]. However, this approach requires very large carrier Rabi frequencies to prevent additional gate errors [95].

Here, we experimentally demonstrate a phase insensitive gate on the clock states of two qubits, where two sidebands of a vibrational mode are excited simultaneously by an optical frequency comb generated from a pulsed laser. The beat-note of the frequency combs is locked to the master oscillator to provide phase coherence between quantum gates performed over long time scales and at different locations while maintaining phase coherence of the entangling gates with microwave and co-propagating Raman rotations. The techniques demonstrated here can also be used to maintain long coherence times on simultaneous carrier and single sideband gates [93], where the carrier transition is induced either by microwaves or Raman beams.

Two-qubit entanglement is generated following the Mølmer-Sørensen protocol [90, 96, 97], in which optical driving fields are tuned near the red and blue sidebands of a vibrational mode. In order to obtain the desired optical spectra for the phase insensitive gate [80, 87], each Raman beam passes through AOMs A and B of Fig. 4.1b to generate a relative frequency offset  $(\nu_A, \nu_{B,r}, \nu_{B,b})$  and allow phase control of the various frequency elements (Fig. 4.4a):

$$\begin{aligned}\nu_{HF} - \nu_\alpha + \delta &= \Delta n \nu_r - \nu_A - \nu_{B,r} \\ \nu_{HF} + \nu_\alpha - \delta &= \Delta m \nu_r + \nu_{B,b} + \nu_A\end{aligned}\tag{4.27}$$

where  $\Delta n$  is a positive integer and  $\Delta m$  is a negative integer,  $\nu_\alpha$  is the frequency of



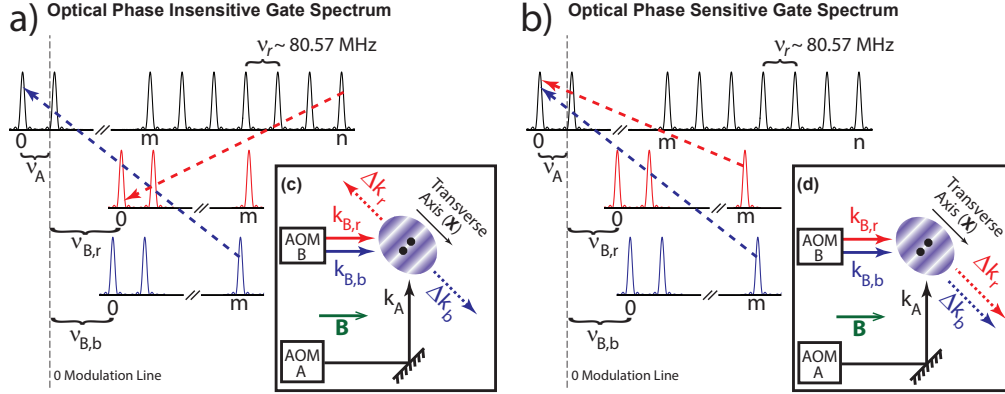


Figure 4.4: Representation of the optical combs in the frequency domain (**a**, **b**) and orientation of the Raman beams with respect to the addressed vibrational mode,  $\mathbf{X}$ , and magnetic field,  $\mathbf{B}$  (**c**, **d**). Beam  $\mathbf{k}_A$  is polarized perpendicular to  $\mathbf{B}$ , while beams  $\mathbf{k}_{B,r}$  and  $\mathbf{k}_{B,b}$  have  $\sigma_+$  polarization. This orientation allows copropagating Raman transitions to be driven by AOM B and the entangling gates to be driven by AOMs A and B. In order to drive the gate, AOMs A and B shift the reference  $0^{th}$  comb tooth by  $\nu_A$ ,  $\nu_{B,r}$  and  $\nu_{B,b}$  from the 0 modulation line (vertical dashed line) and the negative shift for  $\nu_A$  is obtained by taking negative first order diffracted beam. The beat-note between the combs, represented by the dashed arrows, have the required frequencies for the gate and the optical field gradient (purple shading) addresses the transverse modes. **a**) In the optical phase insensitive geometry, off-resonant blue sideband transition is driven by absorption from the  $m^{th}$  comb tooth of the  $\mathbf{k}_{B,b}$  beam and emission into the  $0^{th}$  comb tooth of the  $\mathbf{k}_A$  beam. The absorption and emission directions of the red sideband transition is opposite that of the blue sideband transition such that the gate is driven by absorbing from the  $n^{th}$  comb tooth of the  $\mathbf{k}_A$  beam and emitting into the  $0^{th}$  comb tooth of the  $\mathbf{k}_{B,r}$  beam. **b**) In the optical phase sensitive geometry, off-resonant red and blue sideband transitions are driven by absorption from the  $m^{th}$  comb tooth of the  $\mathbf{k}_{B,r}, \mathbf{k}_{B,b}$  beams and emission into the  $0^{th}$  comb tooth of the  $\mathbf{k}_A$  beam. **c**) In the Mølmer-Sørensen protocol, the gate phase  $\phi_G = -(\phi_{rsb} + \phi_{bsb})$ , where  $\phi_{rsb}, \phi_{bsb}$  are phases associated with the red and blue sideband transitions. Drifts of the optical path length from the source to the ions,  $\delta x$ , along the  $\mathbf{k}_{B,r}, \mathbf{k}_{B,b}$  beam path change the optical phases of these fields at the ion position resulting in a phase shift of  $\phi_{rsb}$  and  $\phi_{bsb}$  by  $\delta\phi = k_{B,r}\delta x \approx k_{B,b}\delta x$  (see Fig. 4.1a and Eq. 4.29). In the optical phase insensitive geometry, since the direction of the red and blue sideband transitions are opposite, the phase changes nearly cancel out so that  $\phi'_G = (\phi_{rsb} - \delta\phi) + (\phi_{bsb} + \delta\phi) \approx \phi_G$ , providing optical path length independence to the gate. **d**) For the optical phase sensitive case, this change is directly imprinted onto the ions:  $\phi'_G = (\phi_{rsb} + \delta\phi) + (\phi_{bsb} + \delta\phi) \approx \phi_G + 2\delta\phi$ . Similar uncorrelated phase sensitivity is also present on path length drifts of the  $\mathbf{k}_A$  beam.

the vibrational mode of interest and  $\delta$  is the symmetric detuning from this mode. Note that  $\nu_{B,r}$  and  $\nu_{B,b}$  are applied to the same AOM, resulting in two nearly copropagating beams. With  $\nu_\alpha \approx 2.5$  MHz,  $\delta = 10$  kHz,  $\nu_r \approx 80.57$  MHz and  $\nu_A = 77.5$  MHz, these equations can be satisfied by  $n = 160$ ,  $\nu_{B,r} \approx 173.4$  MHz and  $m = 154$ ,  $\nu_{B,b} \approx 160.0$  MHz.

After application of the optical fields for the gate time, the collective motion of the ions factors and the qubit states evolve as [77, 90]:

$$\begin{aligned} |00\rangle &\rightarrow |00\rangle - ie^{-i\phi_G}|11\rangle & |01\rangle &\rightarrow |01\rangle - i|10\rangle \\ |11\rangle &\rightarrow |11\rangle - ie^{i\phi_G}|00\rangle & |10\rangle &\rightarrow |10\rangle - i|01\rangle \end{aligned} \quad (4.28)$$

The gate phase is  $\phi_G = \phi_{S,i} + \phi_{S,j}$  with individual “spin” phases:

$$\begin{aligned} \phi_{S,i} &= -(\phi_{rsb,i} + \phi_{bsb,i}) \\ &= -\frac{1}{2}(\Delta\mathbf{k}_r \cdot \mathbf{X}_i - \Delta\phi_r + \Delta\mathbf{k}_b \cdot \mathbf{X}_i - \Delta\phi_b). \end{aligned} \quad (4.29)$$

Here  $\phi_{rsb,i}$  and  $\phi_{bsb,i}$  are the phases associated with the red and blue sideband transitions and  $\mathbf{X}_i$  is the position of the  $i^{th}$  ion [77]. The two optical field pairs address the red ( $\mathbf{k}_A, \mathbf{k}_{B,r}$ ) and blue ( $\mathbf{k}_A, \mathbf{k}_{B,b}$ ) vibrational sidebands. To drive the red sideband using a mode-locked pulsed laser, a photon is absorbed from the  $\mathbf{k}_A$  comb tooth and emitted into the  $\mathbf{k}_{B,r}$  comb tooth. The opposite process takes place for the blue sideband, resulting in  $\Delta\mathbf{k}_r = \mathbf{k}_A - \mathbf{k}_{B,r}$  and  $\Delta\mathbf{k}_b = \mathbf{k}_{B,b} - \mathbf{k}_A$ . Since the  $\Delta\mathbf{k}$  vectors point in opposite directions,  $\Delta\mathbf{k}_r \approx -\Delta\mathbf{k}_b$ , small fluctuations of the optical path length cancel to a high degree, leaving the gate phase unchanged (Fig. 4.4c,d). The

gate phase retains sensitivity to the rf signals applied to the AOMs and may be modified by modulating the applied phases  $\phi_A$ ,  $\phi_{B,r}$  and  $\phi_{B,b}$  to set  $\Delta\phi_r = \phi_A - \phi_{B,r}$  and  $\Delta\phi_b = \phi_{B,b} - \phi_A$  to any desired value.

During an entangling gate, the motion correlated with particular eigenstates of the two qubits are separated in phase space with application of a state-dependent force. Without loss of generality, we consider a single collective mode of motion, and the relative displacements are described by the motional phase [77]

$$\phi_{M,i} = \frac{1}{2} (\Delta\mathbf{k}_r \cdot \mathbf{X}_i - \Delta\phi_r - \Delta\mathbf{k}_b \cdot \mathbf{X}_i + \Delta\phi_b). \quad (4.30)$$

In the optical “phase insensitive” geometry [77], the optical path length dependence of  $\phi_{S,i}$  is transferred to  $\phi_{M,i}$ ; however, the phase dependence of  $\phi_{M,i}$  on the optical path is identical for the two ions and thus global fluctuations do not affect the entangling gate [92].

The static motional phase difference between two ions  $\phi_{M_i} - \phi_{M_j}$  determines the gate time [77] to produce the evolution of Eq. 5.1. If axial vibrational modes are used, the distance between the ions must be carefully controlled and the gate fidelity becomes susceptible to changes in ion spacing [92, 94]. Moreover, entangling longer ion chains becomes problematic as the distance between ions may vary along the chain. These issues are circumvented by using the transverse modes for gate operations [98]. Since the phase fronts created by the optical fields are ideally uniform across the trapping axis when the transverse modes are addressed, the motional phase is the same for all ions (Fig. 4.4c,d). However, misalignment between

the  $\Delta\mathbf{k}$  vectors and the transverse axis by an angle  $\theta_\epsilon$  would introduce a motional phase difference  $\Delta\phi_\epsilon = \Delta k l \sin(\theta_\epsilon)$  between the ions where  $l$  is the ion separation (Fig. 4.5a).

Optical fields can be aligned to better than  $\theta_\epsilon < 0.05^\circ$  by measuring the variation of the resonant photon scattering rate across the ions due to the AC Stark shift induced by the optical field gradient [99]. Since this technique relies on obtaining sufficiently large AC Stark shifts, it requires tuning the Raman beam frequencies close to the Doppler cooling transition which may be impractical with pulsed lasers due to their large bandwidths and limited tuning capabilities. Furthermore, achieving good alignment relies on using large ion crystals; while an ion crystal diameter of hundreds of  $\mu\text{m}$  can be maintained in Penning traps [99], it can be challenging to hold similar length ion crystals in rf Paul traps. An alternative technique incorporates shuttling and utilizes the phase differences of non-copropagating Raman rotations at different points along the trapping axis. The phase differences could be directly measured using a single ion for the alignment of the Raman beams with respect to the transverse axis (see Fig. 4.5b). Although not implemented in this work, high accuracy alignment can be achieved in principle with this technique.

Long term phase coherence can be maintained with an extension of the beat-note stabilization technique by feeding forward changes in  $\nu_r$  to  $\nu_{B,r}, \nu_{B,b}$ . Even in the absence of drifts in  $\nu_r$ , this technique can be used to synchronize pulsed laser operations with a master oscillator to maintain phase coherence with microwaves or operations by other pulsed lasers in the system. A free-running frequency source can be used to generate the AOM frequency  $\nu_A$  as  $\phi_A$  cancels in the gate phase,

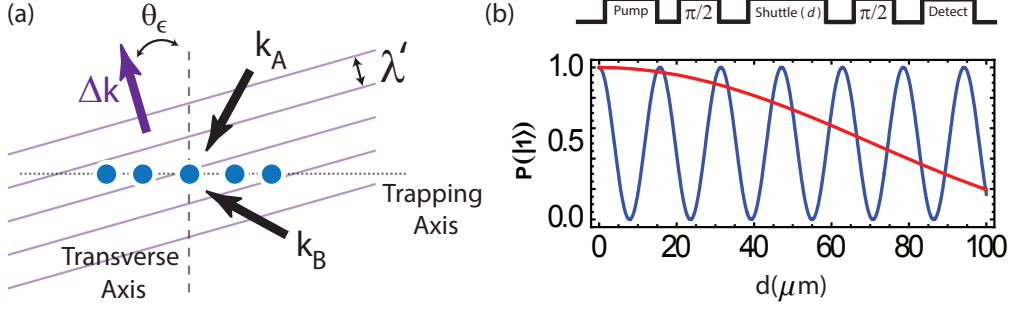


Figure 4.5: Alignment of Raman wavevectors to trapped ion chain. **a)** If the wave fronts of the optical field gradient (purple lines) are misaligned with respect to the trapping axis by an angle  $\theta_\epsilon$ , the ions experience different state-dependent force phases resulting in gate errors. The wave fronts are separated by  $\lambda' = \frac{2\pi}{\Delta k} \approx \frac{2\pi}{\sqrt{2}k} \approx 250$  nm. As an example, in order to realize a phase variation of  $<10^\circ$  along a  $30 \mu\text{m}$  ion chain,  $\theta_\epsilon$  must be  $<0.02^\circ$ . **b)** Experimental sequence for wave front alignment and expected signal. A single ion in the state  $|0\rangle$  is rotated by a resonant non-copropagating Raman  $\pi/2$  pulse and shuttled by  $d$  along the trapping axis. In the new position, the ion is rotated again by another non-copropagating Raman  $\pi/2$  pulse before fluorescent detection of the final state. The blue (red) curve shows the expected ion brightness corresponding to a  $1^\circ$  ( $0.05^\circ$ ) misalignment. The oscillation on the final qubit state is a result of the phase difference between the resonant  $\pi/2$  rotations and is given by  $P(|1\rangle) = \cos^2(\pi d \sin(\theta_\epsilon)/\lambda')$ .

$\phi_G = \Delta\phi_r + \Delta\phi_b = (\phi_A - \phi_{B,r}) + (\phi_{B,b} - \phi_A)$ . In order to maintain phase coherence between entangling gates, copropagating Raman transitions and microwave rotations that have differing drive frequencies, an AWG may be used for these operations rather than free-running frequency sources, where phase relations between different frequency components must be tracked resulting in increased system overhead.

We characterize the optical phase sensitivity of entangling gates by measuring the fidelity of various entangled states through extraction of the density matrix elements of the prepared state [74]; we measure the populations along with the parity contrast in order to extract a fidelity of  $\mathcal{F} \approx 0.86$ . The parity contrast is obtained by scanning the phase of the analysis microwave and Raman  $\pi/2$  pulses

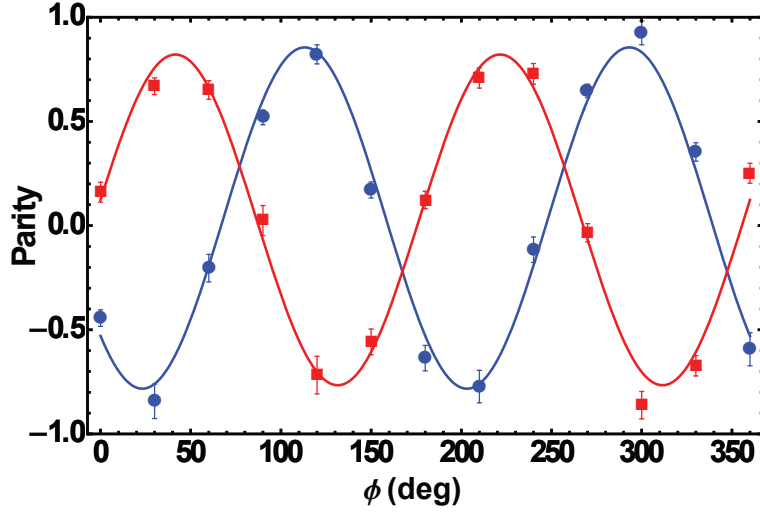


Figure 4.6: Entangling gate phase coherence. The above parity oscillation curves show the entangling gate is phase coherent with both rotations with the entangling gate laser and a microwave oscillator. Parity,  $P(|00\rangle) + P(|11\rangle) - P(|01\rangle) - P(|10\rangle) = A \cos(\phi_G + 2\phi + \phi')$ , of the two qubit entangled state. Ions are first optically pumped to the  $|00\rangle$  state and following the phase insensitive gate, a  $\pi/2$  analysis rotation with phase  $\phi$  is applied. Blue circles are the result of analysis with a copropagating Raman rotation and red squares are analyzed with a microwave rotation. The phase shift between the parity curves is due to different  $\phi'$  static offsets between the gate and the  $\pi/2$  analysis rotations.

after the entangling gate (Fig. 4.6). For the gate, Walsh modulation is implemented to suppress detuning and timing errors [21]. The imperfect fidelity is not a limitation of the phase insensitive gate; we observe similar fidelities using a phase sensitive geometry (Fig. 4.4b,d) for the gate. Thermal populations of the motional states contribute an error of  $\sim 8\%$  and histogram fitting of two ion combined brightness for parity measurements contributes an additional  $\sim 5\%$  [80].

We further characterize and compare the phase insensitive and sensitive gates by directly measuring how the phases of the driving fields are imprinted on the entangled states. In the case of a phase insensitive gate, the phase of the red and blue sideband frequencies modify the gate phase with opposite signs,  $\phi_G \approx \phi_{B,b} - \phi_{B,r}$ . The phase of the parity oscillation shift in opposite directions for red and blue sideband phase shifts. In the phase sensitive case,  $\phi_G \approx \phi_{B,r} + \phi_{B,b} - 2\phi_A$ , which results in the parity phase moving in the same direction for both sideband phase shifts (Fig 4.7a,b). To simulate a relative optical path length change at the ion position, a random phase is added to both sidebands driven by the AWG. The phase insensitive gate parity is not affected by this randomization process, while loss of contrast is observed for the phase sensitive gate as expected (Fig 4.7c,d).

Lastly, we test the stability of our system over long time scales by monitoring the phase of parity oscillations following analysis of the phase insensitive gate by a microwave pulse. We observe phase fluctuations of  $< 8^\circ$  of the parity curve over a period of 24 hours. Therefore, once relative phase relations have been characterized between different quantum operations sharing the same master oscillator, regular monitoring of these phases is not necessary. This long term stability will be necessary

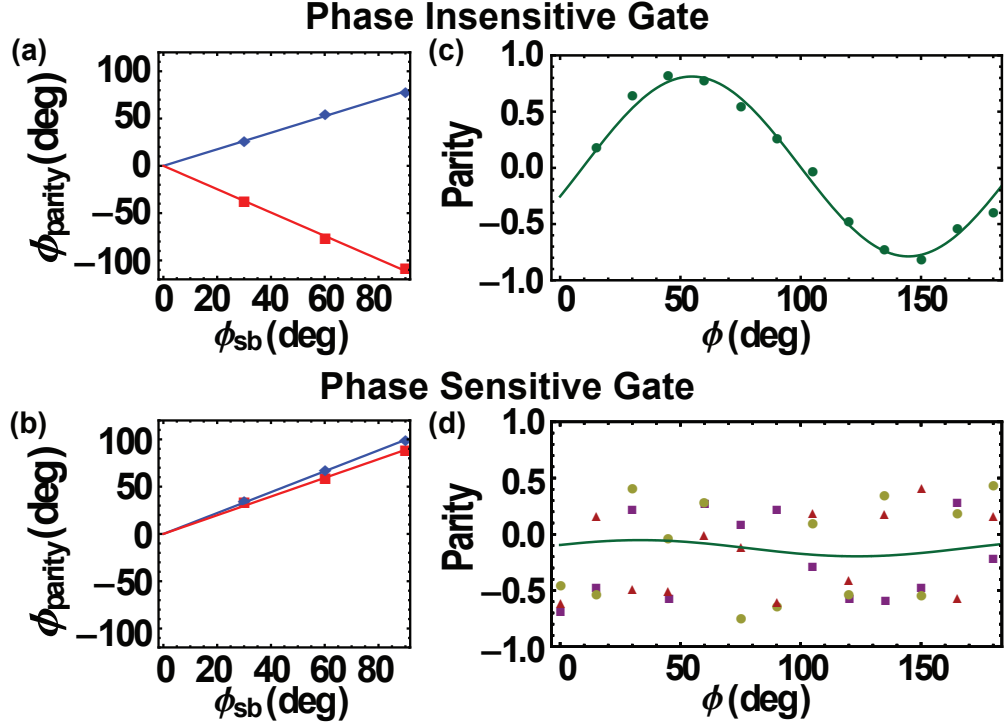


Figure 4.7: Entangling gate phase sensitivity. (a), (b) Gate phase change as a function of red and blue sideband phase advance. The gate phase is measured as the offset of the parity oscillation from the  $\pi/2$  analysis pulse. Changes in the phase of the red ( $\phi_{sb} \equiv \phi_{B,r}$ ) and blue ( $\phi_{sb} \equiv \phi_{B,b}$ ) sideband addressing frequencies cause  $\phi_G$  to shift in opposite directions for the phase insensitive gate while  $\phi_G$  shifts in the same direction for the phase sensitive gate. (c), (d) To simulate a change in the relative optical path length, a random phase is added to frequencies provided by the AWG during the gate at each point. The parity curve is not affected for the phase insensitive gate, while the phase sensitive gate parity curve becomes randomized from point to point as verified by three data sets.



for long computations.

### 4.3 Phase Stabilization Circuit

Cavity length changes cause drifts in the repetition rate of the pulsed laser,  $\nu_r + \delta_r(t)$ , which result in fluctuations of the separation between comb teeth (Fig. 4.4a,b) and thus phase and frequency drifts that can cause gate errors. Since two different comb tooth solutions are used to drive the gate (Eq. 4.27), separate phase locked loops (PLLs) are necessary to lock the  $\Delta m \nu_r$  and  $\Delta n \nu_r$  frequency splittings between the comb teeth (see[87] for details on the PLL). Moreover, phase coherence between quantum operations is needed for full qubit control and can be achieved with the circuit given in Fig. 4.8. By adding a third PLL, coherent copropagating Raman carrier transitions can also be incorporated.

In order to monitor and feed-forward the repetition rate drift  $\delta_r(t)$ , the signal from the fast photodiode is mixed with the master oscillator,  $\nu_{MO} = 12.606$  GHz, to produce beat-notes. The PLLs output a signal that is phase locked with the relevant input beat-note frequencies:

$$\begin{aligned}\nu_{PLL1} &= \Delta n[\nu_r + \delta_r(t)] - \nu_{MO} \\ \nu_{PLL2} &= \nu_{MO} - \Delta m[\nu_r + \delta_r(t)]\end{aligned}\tag{4.31}$$

where  $\Delta m = 154$  and  $\Delta n = 160$  in this experiment. These output signals are mixed

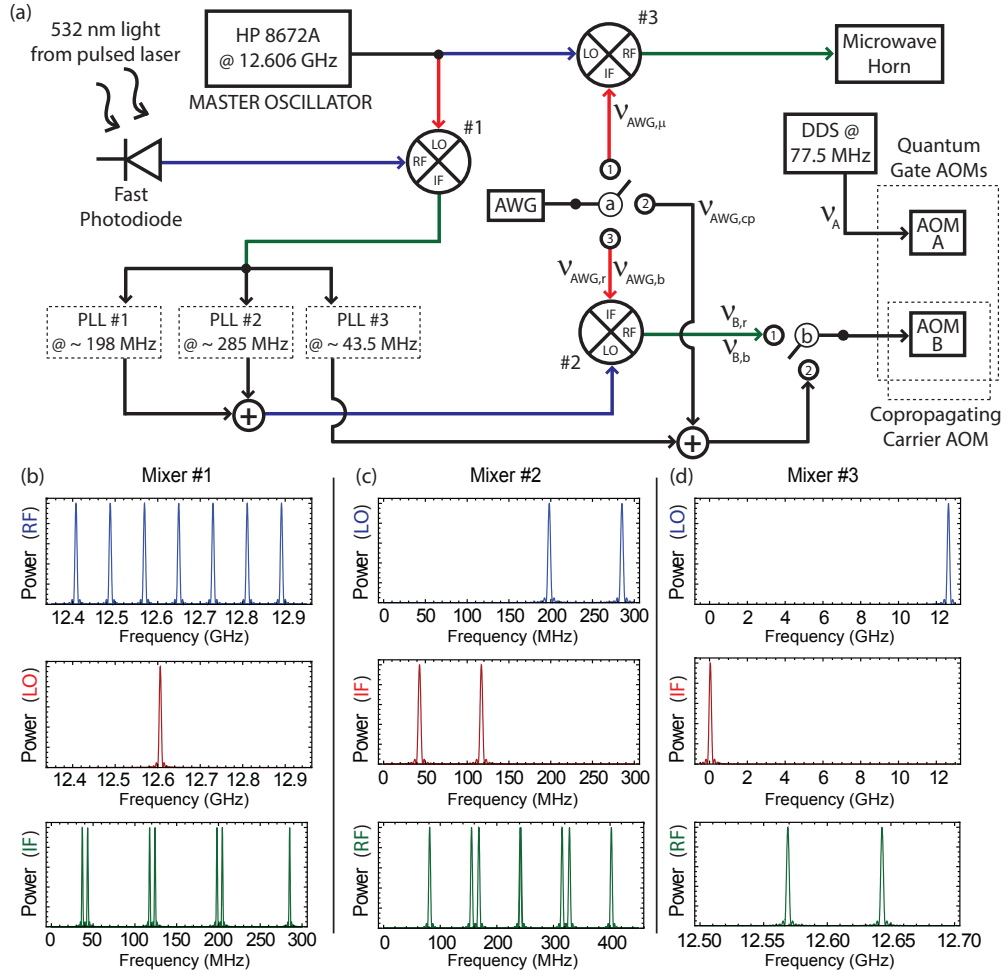


Figure 4.8: Absolute phase control circuit. **(a)** Phase coherence circuit. An AWG is used to provide the necessary frequencies for quantum operations while at the same time maintaining phase relations between different frequency components. Filters are used throughout the circuit to remove undesired frequency components of the mixer output. The second harmonic light of a mode locked Nd:YAG laser at 532 nm is directed to a fast photodiode which generates a frequency comb with tooth separation  $\nu_r$ . The third harmonic at 355 nm is used to drive atomic transitions. **(b)** The photodiode signal is mixed (#1) with the master oscillator (HP 8672A) and sent to three different PLLs which use this signal to output  $\sim 198$  MHz and  $\sim 285$  MHz, matching the difference between the oscillator and the  $m = 154$ ,  $n = 160$  comb teeth. **(c)** The PLL 1 and 2 signals are first combined and then mixed (#2) with the AWG to address the detuned sideband frequencies of the trapped ions. During the gate, switch a  $\rightarrow$  3 and switch b  $\rightarrow$  1. **(d)** Phase coherent microwave rotations with gates are realized by mixing (#3) the AWG signal with the master oscillator to drive carrier transitions. For the microwave rotations, switch a  $\rightarrow$  1. The third PLL provides phase coherent copropagating carrier transitions using the  $p = 157$  comb tooth and AOM B, with switch a  $\rightarrow$  2 and switch b  $\rightarrow$  2.

with the AWG signal to provide driving frequencies for AOM B:

$$\begin{aligned}\nu_{B,r} &= \nu_{PLL1} - \nu_{AWG,r} \\ \nu_{B,b} &= \nu_{PLL2} - \nu_{AWG,b}\end{aligned}\tag{4.32}$$

Both frequencies should be within the bandwidth of AOM B for optimal diffraction efficiency. Inserting Eq. 4.31 and 4.32 in Eq. 4.27 with  $\nu_A = 77.5$  MHz, the AWG frequencies for driving the entangling gate are:

$$\begin{aligned}\nu_{AWG,r} &= \nu_{PLL1} - \Delta n[\nu_r + \delta_r(t)] + \nu_A + \nu_0 - \nu_\alpha + \delta \\ &= -\nu_{MO} + \nu_A + \nu_0 - \nu_\alpha + \delta\end{aligned}\tag{4.33}$$

$$\begin{aligned}\nu_{AWG,b} &= \nu_{PLL2} + \Delta m[\nu_r + \delta_r(t)] + \nu_A - \nu_0 - \nu_\alpha + \delta \\ &= \nu_{MO} + \nu_A - \nu_0 + \nu_\alpha + \delta\end{aligned}\tag{4.34}$$

with  $\nu_{AWG,r} \approx 116.8$  MHz,  $\nu_{AWG,b} \approx 43.2$  MHz. As can be seen from Eq. 4.34, feed-forward to the PLLs not only eliminates sensitivity to  $\delta_r(t)$  but also utilizes the master oscillator  $\nu_{MO}$  as a reference for qubit transitions. To generate microwave rotations that are phase coherent with the Raman transitions, the master oscillator is mixed with the AWG,  $\nu_{AWG,\mu} = \nu_0 - \nu_{MO}$ , and sent to a microwave horn. The achievable coherence time between quantum operations with this technique can be increased by using oscillators with lower phase noise.

It is also possible to realize the set of operations presented in this paper by using only one comb tooth solution,  $\Delta n = \Delta m = 157$ , with  $\nu_A = 160$  MHz,  $\nu_{B,r} \approx$

169.2 MHz and  $\nu_{B,b} \approx 155.7$  MHz. Through the appropriate use of mixers, a single PLL can provide the correct feed-forward to lock these two Raman transitions to the master oscillator (Fig. 4.9). This approach has the advantage of using fewer electronic elements.

In Fig. 4.8 and 4.9, AOM B is used for both entangling gates and copropagating Raman rotations for optimal use of resources. Since the AOMs only work efficiently in a certain rf range, conversion of the rf signals might be necessary to obtain high efficiency beam diffraction for the copropagating Raman rotations. This can be achieved by mixing the rf signals with a DDS to convert signals to the correct frequency range (not shown in Fig. 4.8 and 4.9 for simplicity). As this mixing will result in a common-mode phase and frequency change in both AWG and PLL signals, the DDS signal has no effect on the phase of the rotations so a free-running source can be used.

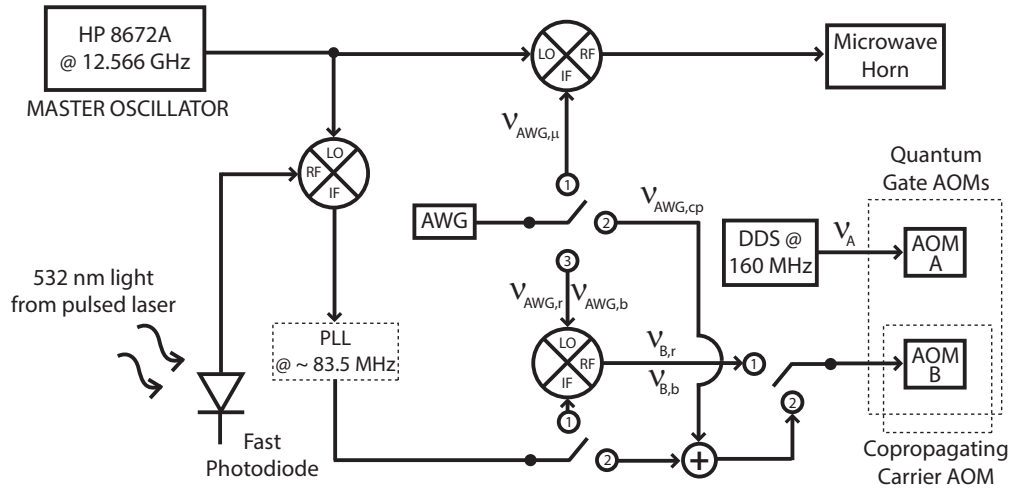


Figure 4.9: Simplified lock circuit for a modular quantum system. This circuit uses a single PLL for phase-coherent qubit operations in a modular architecture.

## 4.4 Implications towards scalability

The techniques presented here can be useful in a large scale modular quantum processor architecture [17, 20]. In this proposal, modules hold ion chains of manageable sizes and entanglement within a module is generated with mutual Coulomb interactions while photonic interfaces [49, 100] establish connections between separate modules. As shown here, the use of a common master oscillator for all quantum operations and insensitivity to optical path length fluctuations can be implemented to realize phase coherent operations across this architecture.

In the shuttling model proposed for a large-scale quantum processor, ions are transported between various trapping regions in order to perform specific operations [12]. These phase stabilization techniques might be beneficial in this model as it is important to maintain phase coherence between the operations performed at different regions of the processor and at different times. Moreover, coupling to transverse modes for multi-qubit gate operations instead of axial modes would eliminate errors that might stem from small changes in ion separation after shuttling between regions. Finally, the complexity of the device electrode structure might be reduced as it is not necessary to keep a uniform ion spacing with the use of transverse modes [98].

In summary, we demonstrate long term coherence between various qubit operations utilizing optical and microwave fields referenced to a single master oscillator. The setup presented here effectively eliminates any optical path length related phase drifts from these operations, obviating the need for optical interferometric stability in a quantum system. Moreover, the use of a master oscillator as a reference

provides coherence between qubit operations done at different times and at different locations which is central to realizing a large-scale, distributed and modular quantum computer. By using a stable master oscillator, the long coherence times of trapped atomic ions can be harnessed effectively to execute many subsequent operations on the system and preserve quantum information for long times while operations are performed on other qubits.

## Chapter 5: Entanglement using photons and phonons

Quantum entanglement is the central resource behind quantum information science, from quantum computation and simulation [1, 101] to enhanced metrology [102] and secure communication [1]. These applications require the quantum control of large networks of quantum bits (qubits) to realize gains and speedups over conventional devices. However, propagating entanglement becomes difficult or impossible as the system grows in size, owing to the inevitable decoherence from the complexity of connections between the qubits and increased couplings to the environment. Here, we demonstrate the first step in a modular approach [17] to scaling entanglement by utilizing complementary quantum buses on a collection of three atomic ion qubits stored in two remote ion trap modules. Entanglement within a module is achieved with deterministic near-field interactions through phonons [13], and remote entanglement between modules is achieved through a probabilistic interaction through photons [41]. This minimal system allows us to address generic issues in the synchronization of entanglement with multiple buses, while pointing the way toward a modular large-scale quantum information architecture that promises less spectral crowding and thus potentially less decoherence as the number of qubits increases [17]. We generate this modular entanglement faster than the observed re-

motely entangled qubit decoherence rate, showing that entanglement can be scaled by simply adding more modules.

Small modules of qubits have been entangled through native local interactions in many physical platforms, such as trapped atomic ions through their Coulomb interaction [13], Rydberg atoms through their electric dipoles [103, 104], nitrogen-vacancy centers in diamond through their magnetic dipoles [105], and superconducting Josephson junctions through capacitive or inductive couplings [106, 107]. However, each of these systems is confronted with practical limits to the number of qubits that can be reliably controlled, stemming from inhomogeneities, the complexity and density of the interactions between the qubits, or quantum decoherence. Scaling beyond these limits can be achieved by invoking a second type of interaction that can extend the entanglement to other similar qubit modules. Such an architecture should therefore exploit both the local interactions within the qubit modules, and also remote interactions between modules (an example architecture is shown in Fig 1). One promising approach is to directly move qubits between different modules [12, 60], but this approach is limited by the difficulty of moving qubits over large distances. Optical interfaces provide ideal buses for extending entanglement between modules [38, 39], as optical photons can propagate over macroscopic distances with negligible loss. Several qubit systems have been entangled through remote optical buses, such as atomic ions [49], neutral atoms [65], and nitrogen-vacancy centers in diamond [66].

In the experiment reported here, we juxtapose local phonon and remote photon entanglement buses utilizing trapped atomic ion qubits, balancing the requirements



of each interface within the same qubit system. The observed entanglement rate within and between modules is faster than the observed entangled qubit decoherence rate. This is critical in quantum modular architectures because the required resource scaling is superexponential in the ratio of decoherence rate to entanglement rate [17]. This ratio is observed to be 0.2 in this experiment, many orders of magnitude lower than previous experiments demonstrating remote entanglement [50, 65, 66]. Overcoming the resource scaling requirement makes trapped ions a leading candidate for realizing a quantum network.

Scaling this system will also require mitigating crosstalk within modules. For example, when generating photons for intermodular entanglement, laser scatter and radiated light will disturb neighboring qubits within a module. This may require the use of different species of atoms as photonic and memory qubits (see Chapter 6). Quantum information could then be transferred from the photonic qubits to the memory qubits via the Coulomb bus [108]. The second (photonic) species can also be used for intermittent sympathetic cooling [109].

The modular architecture demonstrated in this experiment can be expanded to include many modules. Here an optical cross connect switch can create a flexible, reconfigurable photonic network between modules (Fig. 5.1b) and thus be made fault tolerant for the execution of extended quantum circuits [17]. Modular architectures may be used as the backbone of a quantum repeater network [32] and of a quantum network of clocks [37]. The distance between nodes may be increased with the development of low-loss UV fibers or the efficient down-conversion of photons to telecommunication wavelengths without affecting the entanglement rate and enable

long distance quantum networks [110].

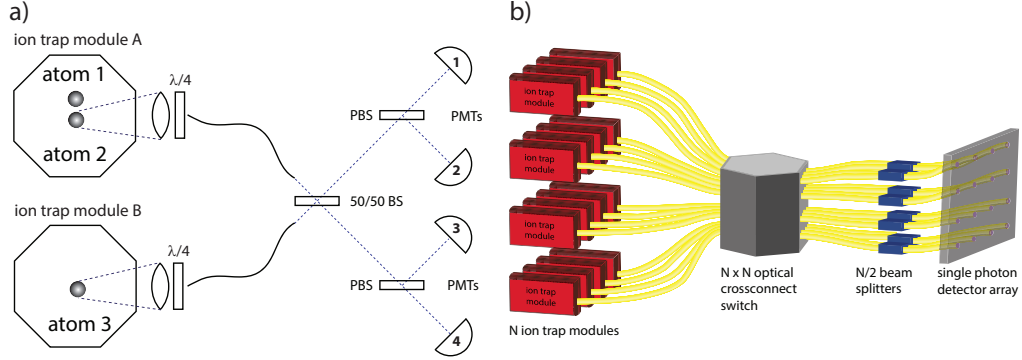


Figure 5.1: Experimental setup and a modular architecture for large scale quantum network. **a)** Two modules separated by  $\sim 1$  meter each contain an ion trap. High numerical aperture objectives couple spontaneously emitted photons from a single atom into a single-mode optical fiber. The photons from atoms in separate traps interfere on a 50/50 beam-splitter, are sorted by polarizing beam-splitters then detected by photomultiplier tubes (PMTs). Coincident detection of photons on specific PMT pairs heralds entanglement of atomic spins. **b)** Schematic of a large-scale, modular quantum network of trapped ions. Ion trap modules (red boxes) confine atoms coupled together through their Coulomb bus, and entanglement within modules is accomplished with the application of spin dependent forces to the trapped atoms [4]. Probabilistic, heralded entanglement is generated between modules via interference of emitted photons from each module. A reconfigurable  $N \times N$  cross connect switch links arbitrary modules. Photon interference occurs at fiber beam-splitters, and a single photon detector array heralds entanglement of atomic spins between modules.

## 5.1 Juxtaposition of two entanglement buses

In this experiment, ion trap module A is a segmented, four blade design useful for holding chains of trapped atoms. A trap drive frequency of 37.15 MHz is used to achieve secular transverse frequencies of  $\sim 2.4$  MHz. Module B is a four rod Paul trap that confines a single atom. This trap is driven at 37.72 MHz to achieve secular frequencies of  $\sim 1.5$  MHz. The qubits in this experiment are defined by the two hyperfine ‘clock’ states,  $|F = 0, m_F = 0\rangle \equiv |0\rangle$  and  $|F = 1, m_F = 0\rangle \equiv |1\rangle$ , which are

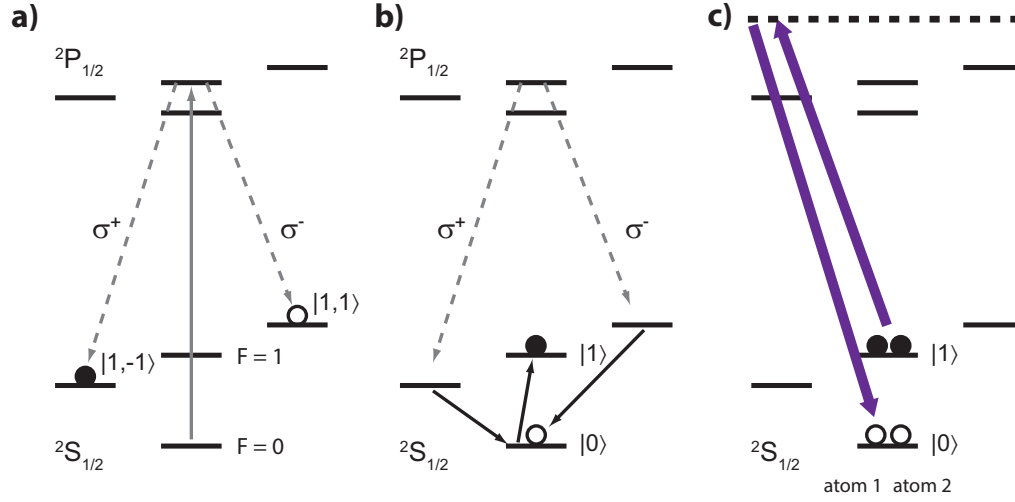


Figure 5.2: Qubit manipulations for generating entanglement between and within modules. **a)** Resonant excitation scheme and single photon emission in  $\text{Yb}^+$  atom system. After optically pumping the atoms to the  $|F, m_F\rangle = |0, 0\rangle$  state of the  $^2S_{1/2}$  manifold, a frequency-doubled, mode-locked Ti:sapphire laser excites the atom to the  $|1, 0\rangle$  state of the  $^2P_{1/2}$  manifold whereby the atom decays to the  $|1, \pm 1\rangle$  states via emission of  $\sigma^\mp$  polarized photons into optical fibers. **b)** After interference of the two photons on a 50/50 non-polarizing beam-splitter, we apply a series of microwave transfer pulses to transfer the entangled state to the clock basis, resulting in the state  $|01\rangle + e^{i\phi_{AB}}|10\rangle$  where  $\phi_{AB}$  is the intermodal phase. **c)** We entangle atomic spins within module A through spin dependent optical dipole forces [13, 74].

separated by  $\omega_0 = 2\pi \times 12.64282$  GHz in the  $^2S_{1/2}$  manifold of trapped  $^{171}\text{Yb}^+$  atoms. Laser cooling, optical pumping, and readout occur via standard state-dependent fluorescence techniques [22]. The qubits are trapped in two independent modules separated by  $\sim 1$  meter as shown in Fig. 5.1a. (The ion traps, light collection optics, and interferometer could in principle be part of a modular, scalable architecture as shown in Fig. 5.1b.)

In order to generate remote entanglement between atoms in physically separated ion trap modules, we synchronously excite each atom with a resonant fast laser pulse [49]. A fraction of the resulting spontaneously emitted light is collected into an optical fiber, with each photon's polarization ( $\sigma^+$  or  $\sigma^-$ ) entangled with its parent atom due to atomic selection rules (Fig. 5.2a). Each photon passes through a quarter-wave plate that maps circular to linear polarization ( $\sigma^+ \rightarrow H$  and  $\sigma^- \rightarrow V$ ), and then the two photons interfere on a 50/50 beam-splitter, where detectors monitor the output (see Fig. 5.1a) [50]. We select the two-photon Bell states of light  $|HV\rangle + e^{i\phi_D}|VH\rangle$ , where  $\phi_D$  is 0 or  $\pi$  depending on which pair of detectors registers the photons [33]. Finally, a series of microwave pulses transfers the atoms into the  $\{|0\rangle, |1\rangle\}$  basis (Fig. 5.2b), ideally resulting in the heralded entangled state of the two remote atomic qubits  $|01\rangle + e^{i\phi_{AB}}|10\rangle$ .

In addition to using a photonic interconnect between ion traps, we use the Coulomb-coupled transverse phonon modes of the atoms to create entanglement within one module (see Fig. 5.2c). Off-resonant laser beams drive stimulated Raman transitions between the qubit levels and impart spin-dependent forces detuned from the phonon modes. Following conventional Coulomb gate protocols [13, 90], after a

certain time the motion returns to its original state, and the four two-qubit basis states are ideally mapped to the following entangled states

$$\begin{aligned} |00\rangle &\rightarrow |00\rangle - ie^{-i\phi_A}|11\rangle & |01\rangle &\rightarrow |01\rangle - i|10\rangle \\ |11\rangle &\rightarrow |11\rangle - ie^{i\phi_A}|00\rangle & |10\rangle &\rightarrow |10\rangle - i|01\rangle, \end{aligned} \quad (5.1)$$

where  $\phi_A$  is the intramodular phase from this optical Raman process in module A [77]. This phase depends on the relative optical phases of two non-copropagating lasers (see Chapter 4). Using the above gate operation on two Doppler-cooled atoms within a module ( $\bar{n} \sim 3$ ), we create the state  $|00\rangle - ie^{-i\phi_A}|11\rangle$  with a fidelity of  $0.85 \pm 0.01$ , excluding detection error, as shown in Fig. 5.3a,b. Cooling below the Doppler limit was not implemented in this experiment in order to keep the experimental repetition rate high for fast generation of remote entanglement. Higher fidelity Coulomb gates may be achieved by better control of the RF amplitude applied to the ion trap and through the use of ground state cooling to reduce sensitivity to small detuning errors from the trapped atoms sidebands of motion. The Coulomb entangling gate makes use of Walsh function modulation  $W[1]$  to reduce the sensitivity of the gate to detuning and timing errors [21]. We pick a detuning  $\delta$  from a transverse mode of motion and set the gate time  $t_g = 2/\delta$  with a  $\pi$  phase advance of the sidebands at  $t = t_g/2$ . We adjust the average Raman laser intensity power to make sideband Rabi frequency  $\eta\Omega$  satisfy  $\delta = 2^{3/2}\eta\Omega$  to complete the entangling gate  $|00\rangle \rightarrow |00\rangle - ie^{-i\phi_A}|11\rangle$  in ion trap module A.

We now describe the integration of both photonic and phononic buses to gen-

erate entangled 3-particle states. The three atoms are first prepared in the state  $|\psi_1\psi_2\rangle_A|\psi_3\rangle_B = |00\rangle_A|0\rangle_B$  with atoms 1 and 2 in module A and the remote atom 3 in module B (see Fig. 5.1a). After heralding entanglement between atom 2 in module A and atom 3 in module B using photons, we re-initialize atom 1 to the state  $|0\rangle_A$  with an individual addressing optical pumping beam, and then we entangle atoms 1 and 2 within module A using phonons. Ideally, this produces the state

$$\begin{aligned} |\psi_1\psi_2\rangle_A|\psi_3\rangle_B = & \left( |00\rangle_A - ie^{-i\phi_A}|11\rangle_A \right) |1\rangle_B \\ & + e^{i\phi_{AB}} \left( |01\rangle_A - i|10\rangle_A \right) |0\rangle_B \end{aligned} \quad (5.2)$$

The above state is equivalent to a GHZ state [111], and the parity of any pair of atoms is correlated with the spin state of the third atom. We take advantage of this property to probe the parity of atoms 1 and 2 in module A, and correlate it with the state of remote atom 3 in module B. After making photon and phonon connections between the atoms, we apply a  $\pi/2$  Raman rotation to atoms 1 and 2 with a variable phase  $\phi$  followed by state detection of all three atoms. When the remote atom is measured in state  $|\psi_3\rangle_B = |1\rangle$ , the spin parity of atoms 1 and 2 in module A is  $\Pi = \Pi_c \cos(\phi_A - 2\phi)$ . When the remote atom is measured in state  $|\psi_3\rangle = |0\rangle_B$ , the atoms in module A should be mapped to a state with zero average parity, regardless of the phase of the  $\pi/2$  Raman rotation. We observe this correlation with a remote entangled state generation rate of  $\sim 4 \text{ sec}^{-1}$  as shown in Fig. 5.3b,c. The fidelity of detecting the state  $|00\rangle_A - ie^{-i\phi_A}|11\rangle_A$  of atoms 1 and 2 conditioned on detecting the remote atom 3 in the state  $|1\rangle_B$  is  $0.63 \pm 0.03$ .

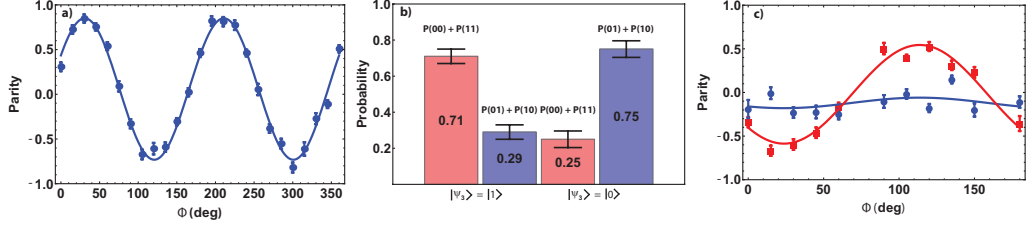


Figure 5.3: Entanglement between qubits in the same module without and with heralded entanglement between modules. **a)** After preparing the atoms in the state  $|00\rangle$  and applying an entangling gate through phonons within a module (Eq. 5.1), we measure the parity of the entangled state following  $\pi/2$  qubit rotations with variable phase  $\phi$  with respect to the intramodular phase  $\phi_A$  of the two atoms. The amplitude of the parity oscillation is  $0.79 \pm 0.02$  and the fidelity of the entangled state is  $0.85 \pm 0.01$  excluding state detection errors. **b)** Populations of two atoms in ion trap module A after remote entanglement between atoms 2 and 3 followed by entanglement between atoms 1 and 2 as described in the text. After measuring the resulting three particle state (see Eq. 5.2), if the remote atom is in the state  $|1\rangle$ , atoms 1 and 2 should be in an even parity state. If the remote atom is in the state  $|0\rangle$ , atoms 1 and 2 should be in an odd parity state. We observe this correlation with the remote atom with probability  $0.71 \pm 0.04$  and  $0.75 \pm 0.05$  respectively after averaging over detection of the entangled photon states. **c)** Parity oscillation of atoms 1 and 2 conditioned on detecting the remote atom in the state  $|1\rangle_B$  (red squares) and  $|0\rangle_B$  (blue circles). After remote entanglement between modules and entanglement within one module, we apply a Raman  $\pi/2$  rotation with variable phase  $\phi$  to atoms 1 and 2 in module A and measure the state of all three atoms. If the remote atom is in the state  $|0\rangle_B$ , a  $\pi/2$  rotation on atoms 1 and 2 maps  $|\psi_1\psi_2\rangle_A = |01\rangle_A - i|10\rangle_A$  to a state with zero average parity for any phase  $\phi$  of the rotation. If the remote atom is in the state  $|1\rangle_B$ , a  $\pi/2$  rotation with variable phase  $\phi$  of  $|\psi_1\psi_2\rangle_A = |00\rangle_A - ie^{-i\phi_A}|11\rangle_A$  maps the parity of this state to  $\cos(\phi_A - 2\phi)$ . We observe such a parity oscillation correlated with the state of the remote atom. The fidelity of the two qubit entangled state  $|00\rangle_A - ie^{-i\phi_A}|11\rangle_A$  conditioned on detecting the remote atom in  $|\psi_3\rangle_B = |1\rangle_B$  is  $0.63 \pm 0.03$ . Error bars in a)-c) are the fit error of experimental histograms of the two qubits' four basis states.

Detection error of a single atom in an ion trap module is limited by off-resonant pumping from the  $F = 1$  to the  $F = 0$  manifold of the  $^2S_{1/2}$  ground state through the  $F = 1$  manifold of the  $^2P_{1/2}$  excited state [22], and is  $\sim 1\%$  in the experiments presented here. Detection error of two qubits in the same module is limited by the use of a single PMT detector where the photon detection histograms of a single qubit in the state  $|1\rangle$  and two qubits in the state  $|11\rangle$  may overlap. This overlap is  $\sim 8\%$  in these experiments.

## 5.2 A modular quantum system

Scaling this architecture to many modules can vastly simplify the complexity of phases to be tracked and controlled. For  $N \gg 1$  modules each with  $n \gg 1$  qubits and  $m \ll n$  optical ports at each module, the number of overall phases is reduced by a factor of  $1/N + (m/n)^2$  compared to that for a fully connected set of  $nN$  qubits [17]. Of course, in a modular architecture there may be overheads associated with the reduced connectivity, but it will be useful to have flexibility in this tradeoff.

Though the connectivity of the qubits is reduced, the use of two different interactions to generate entanglement necessitates phase referencing the intramodular phases to the intermodular phases within and across all modules. The intermodule phase  $\phi_{AB}$  in the experiment is easily controlled by setting the phase difference of microwave rotations between the two modules. The intramodule phase  $\phi_A$  is determined by the optical phase difference of the two Raman lasers and is passively stable for a single entangling experiment for typical gate times of order  $100 \mu s$ .



Tracking and controlling the optical phases between many entangled pairs in spatially separated modules at different times can be accomplished by utilizing “phase insensitive” gates [77]. All phases introduced by qubit rotations and entangling operations between and within modules can be referenced to a common, high-quality master oscillator as discussed in chapter 4 [81].

In previous experiments, entanglement between remote atom spins at rates of  $0.002 \text{ sec}^{-1}$  was accomplished using atom-photon frequency entanglement [62], and at rates of  $0.026 \text{ sec}^{-1}$  using atom-photon polarization entanglement [50]. Here, we dramatically increase the single photon collection efficiency by using high numerical aperture microscope objectives and detecting two out of four Bell states of light emitted by the atoms to achieve a heralded entanglement rate of  $4.5 \text{ sec}^{-1}$ . This is critical in quantum modular architectures because the required resource scaling is superexponential in the ratio of decoherence rate to entanglement rate [17]. This ratio is observed to be 0.2 in this experiment, many orders of magnitude lower than previous experiments demonstrating remote entanglement (See Table 5.1). Overcoming the resource scaling requirement makes trapped ions a leading candidate for realizing a modular quantum network.

The experiments here suggest a figure of merit for a quantum repeater network with maximum separation between nodes: the coherent entanglement distance  $D_{\text{ent}} = d_q R \tau$ , where the physical qubit separation  $d_q$  is multiplied by the entanglement rate  $R$  and the entangled state coherence time  $\tau$ . This figure of merit indicates the maximum entanglement distance between modules of a quantum network with a positive output entanglement rate. The experiments presented here give  $D_{\text{ent}} = 1$

technology	entanglement rate (sec <sup>-1</sup> )	coherence time (sec)	$x^x$ resource scaling
ions [20]	4.5	1.1	0.72
neutral atoms [65]	10	$1 \times 10^{-4}$ [53]	$10^{3000}$
superconductors [61]	$10^4$	$1.7 \times 10^{-6}$	$10^{104}$
NV centers [66]	0.004	$10^{-3}$	$10^{100000}$

Table 5.1: Resource scaling of modular architectures across different platforms. For fault tolerant operation of a modular network, the resource scaling has superexponential dependence on the ratio of the mean remote entanglement generation time to the qubit coherence time [17], denoted  $x^x \equiv \left(\frac{\tau_E}{\tau_D}\right)^{\frac{\tau_E}{\tau_D}}$ . The superexponential resource scaling highlights the importance of creating remote entanglement at rates exceeding the decoherence rate of the qubits. When the entangled state coherence time is not provided in the listed reference, the single qubit coherence time is substituted.

$m \times 4.5 \text{ sec}^{-1} \times 1.12 \text{ sec} \approx 5$  meters, orders of magnitude larger than previous experiments in any platform (see Table 5.2). The coherent entanglement distance in this experiment can be increased by increasing the remote entanglement rate and entangled state coherence time. In addition, the qubit separation may be increased by many orders of magnitude without affecting the entanglement rate. The development of low-loss UV fibers or the efficient down-conversion of the entangled photons emitted by the atoms to wavelengths compatible to commercially available optical fibers could enable long distance quantum repeater networks [110].

technology	entanglement rate (sec <sup>-1</sup> )	coherence time (sec)	remote qubit separation (m)	$D_{\text{ent}}$
ions [20]	4.5	1.1	1	5 m
neutral atoms [65]	10	$1 \times 10^{-4}$ [53]	21	2 cm
superconductors [61]	$10^4$	$1.7 \times 10^{-6}$	$6 \times 10^{-3}$	100 $\mu\text{m}$
NV centers [66]	0.004	$10^{-3}$	3	12 $\mu\text{m}$

Table 5.2: Coherent entanglement distance across different platforms. The coherent entanglement distance  $D_{\text{ent}}$  is the product of the physical qubit separation multiplied by the entanglement rate and coherence time of the entangled state. When the entangled state coherence time is not provided in the listed reference, the single qubit coherence time is substituted.  $D_{\text{ent}}$  indicates an upper bound on the maximum distance between modules in a quantum network with positive output entanglement rate.

## Chapter 6: Dual species ion trap

Modular systems may have cross talk between photonic link qubits and the neighboring memory qubits if the two types of qubits are identical. Even with the high numerical aperture objectives used in experiments described in this thesis, the probability of generating remote entanglement after resonant excitation of two photonic qubits is  $\sim 10^{-5}$ . While attempting to make remote entanglement, resonantly scattered light by photonic link qubits can be absorbed by neighboring memory qubits with relatively high probability. By integrating over the solid angle, the probability that a photon enters a the solid angle subtended by a lens with  $\text{NA} = 0.6$  is 0.1. The maximum theoretical coupling of the atom  $\sigma^{\pm}$  modes to a Gaussian  $\text{TEM}_{00}$  fiber mode is  $P_{\text{fiber}} = 0.5$  [70]. Although two out of the four possible Bell

states of light were detected in this thesis, it is possible to detect all four Bell states of light emitted by the remote atoms [73], so  $P_{\text{Bell}}$  could be equal to 1. The atoms emit  $\sigma^\pm$  polarized light with probability  $2/3$ , fixing  $P_{\text{branch}} = 2/3$ . The quantum efficiency of the detectors used in this experiment were  $P_{\text{PMT}} = 0.35$ , but future technological developments could increase the quantum efficiency to nearly unity. If the atoms are resonantly excited and emit a photon with unit probability, an optimistic estimate of the probability of heralding entanglement between remote qubits is  $P = (P_{\Omega/4\pi} P_{\text{fiber}} P_{\text{PMT}} P_{\text{branch}})^2 P_{\text{Bell}} = (0.1 \times 0.5 \times 1 \times \frac{2}{3})^2 \times 1 = 1.1 \times 10^{-3}$ .

The probability of an ion scattering a resonant photon toward a memory qubit can be estimated from the resonant absorption cross section from a memory qubit in close proximity to a photonic link qubit. The fraction of the total  $4\pi$  solid angle subtended by the resonant absorption cross section  $\sigma = 3\lambda^2/2\pi$  of an atom a distance  $d$  away from the photonic link, assuming an isotropic radiation pattern, is

$$\frac{\Omega}{4\pi} = \frac{1}{2} \int_0^\theta \sin \theta' d\theta' = \frac{1}{2} \left( 1 - \frac{1}{\sqrt{1 + \frac{3\lambda^2}{2\pi^2 d^2}}} \right) \quad (6.1)$$

where the limit of integration  $\theta = \tan^{-1} \left( \frac{1}{d} \sqrt{\frac{3\lambda^2}{2\pi^2}} \right)$ . For typical ion spacings of a few  $\mu m$ , the probability that an ion scatters into the memory is nearly of order the maximum remote entanglement probability per attempt as is shown in Fig. 6.1. If single species qubits are used throughout a modular architecture, achieving fault-tolerant remote entanglement given perfect optical addressing of the photonic qubit will require separating the photonic link qubits from the memory qubits by large distances.

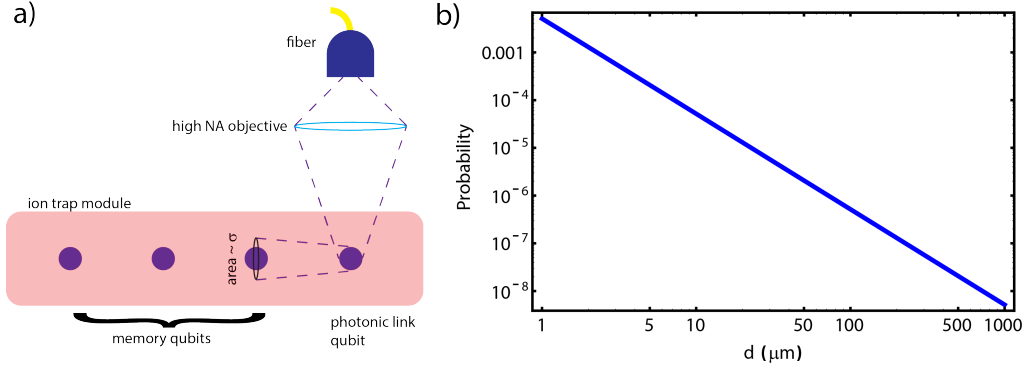


Figure 6.1: Probability of spontaneous emission from photonic qubits absorbed by neighboring memory qubits. **(a)** If a laser beam is focused down to resonantly excite a qubit with zero intensity on a neighboring qubit a distance  $d$  away, the resulting spontaneously emitted photon may still be absorbed by an adjacent qubit. The relative probabilities of collecting a single photon or scattering a photon into the memory are given by the area subtended by the collection optics and the resonant absorption cross section respectively. **(b)** The probability of a memory qubit a distance  $d$  away from the photonic qubit absorbing a photon is shown in the figure. Low errors required for fault tolerance will require large separations between photonic and memory qubits in a single-species system.

Shuttling memory qubits away from the photonic link qubits can mitigate cross talk, but the shuttling trapped atoms over large distances or around corners in junction ion traps may prove challenging in large scale systems. Alternatively, the use of two different ion species can mitigate cross talk due to widely different resonant frequencies of two different ion species. After establishing a remote entanglement between the photonic link qubits, the entangled state can be swapped to the memory qubits, freeing the photonic link qubits to re-establish remote entanglement.

There are many potential choices for a photonic link ion, but paramount in selecting a second ion should be the maximizing remote entanglement rate while using photons with appropriate wavelengths for fiber transmission. Since remote entanglement is a probabilistic process, the remote entanglement rate is the product of the success probability per attempt and the number of attempts per unit

time. Much effort and progress has been made putting qubits in cavities [54, 65] or using high numerical aperture systems for efficient light collection. However, fast experimental repetition rates are beneficial to the entanglement rate. With trapped ions and making use of entanglement between the ion spin and the photon polarization, the repetition rate is ultimately limited by the speed of preparing a pure quantum state via optical pumping. In order to prepare a pure quantum state with high fidelity, a few 10s of photons must be scattered for optical pumping. The time scale for this is set by the lifetime of the pumping transition and is of order a few hundred nanoseconds, resulting in a remote entanglement attempt rate of a  $\sim 5$  MHz.

Atomic isotopes with nuclear spin  $1/2$  are particularly useful for high remote entanglement attempt rates. The preparation of the pure quantum state  $|F, m_F\rangle = |0, 0\rangle$  by optical pumping is accomplished by switching on frequency sidebands; the fidelity of the  $|0, 0\rangle$  state need not be determined by pure polarization control. In addition, ultrafast excitation of the qubit may proceed without need to upload coherence to the remote atoms as the remote atoms can decay via  $\sigma^\pm$  decay to produce heralded  $|\psi^\pm\rangle$  entangled Bell states. Finally, spin  $1/2$  ions have relatively simple schemes for state detection without the need for shelving to metastable atomic levels. Unfortunately, nuclear spin  $1/2$ , single valence electron atoms are fairly rare. Cadmium and mercury both half spin  $1/2$  isotopes, but the deep UV transitions of these ions pose significant technical challenges to using these qubits as a photonic link in a modular quantum system. Barium has a spin  $1/2$  radioactive isotope with a half-life of  $\sim 10$  years and is used in medical imaging

applications. Because  $^{133}\text{Ba}^+$  and  $^{171}\text{Yb}^+$  have similar charge to mass ratios (thus facilitating co-trapping in a single ion trap zone), this isotope of barium may prove highly useful as a photonic link qubit while simultaneously offering simple state detection of the photonic link qubit for diagnostic purposes. In addition and unlike  $^{171}\text{Yb}^+$ ,  $^{133}\text{Ba}^+$  has a  $D_{5/2}$  metastable state outside of the Doppler cooling cycle with a decay rate of  $1/80 \text{ sec}^{-1}$  without other low lying F states, simplifying shelving if ultra-high state detection fidelity is needed. Barium also has strong transitions at 493 nm and 650 nm, thus potentially offering a path to efficient down conversion of the photon to telecommunication wavelengths [110]. To date, no qubit manipulations of  $^{133}\text{Ba}^+$  have been demonstrated. Other isotopes of Barium, such as  $^{138}\text{Ba}^+$ , also serve as a good photonic link qubit in conjunction with  $^{171}\text{Yb}^+$  memory qubits.

## 6.1 Entanglement swapping between photonic link qubits and memory qubits

After creating remote entanglement between photonic qubits, the coherence should be transferred to the memory qubits. There are a wide variety of entangling schemes to perform this entanglement swap. One such direction is the use of quantum logic spectroscopy [108], where entanglement is swapped between qubits using the collective modes of motion. This algorithm starts with two ions in the ground state of a collective mode of motion  $|0\rangle_m$ . One qubit stores a superposition state  $\alpha|0\rangle + \beta|1\rangle$ , while the other memory qubit is in the state  $|0\rangle$ . The total state is then  $(\alpha|0\rangle + \beta|1\rangle)|0\rangle|0\rangle_m$ . A red sideband  $\pi$  pulse is performed on the first

qubit, resulting in the state  $\alpha|00\rangle|0\rangle_m + \beta|00\rangle|1\rangle_m = |00\rangle(\alpha|0\rangle_m + \beta|1\rangle_m)$ . Another red sideband  $\pi$  pulse is performed on the memory qubit, and the resulting state is  $|0\rangle(\alpha|0\rangle + \beta|1\rangle)|0\rangle_m$ , thus transferring coherence from the photonic link qubit to the memory qubit. Unfortunately, this scheme relies on the qubit being in the ground state of motion  $|0\rangle_m$  making this scheme practically difficult. The photonic link is probabilistic, and photon recoil and anomalous heating of the qubits will require cooling and which may slow the remote entanglement attempt rate.

Another entanglement swapping scheme relies on the use of two Mølmer-Sørensen gates with appropriate relative phase control of the two gates. If the photonic and memory qubit states are  $(\alpha|0\rangle + \beta|1\rangle)|0\rangle = \alpha|00\rangle + \beta|10\rangle$ , then a Mølmer-Sørensen gate results in the state

$$|\psi\rangle = \alpha(|00\rangle - ie^{-i\phi_{G1}}|11\rangle) + \beta(|10\rangle - i|01\rangle) \quad (6.2)$$

where the gate phase  $\phi_{G1}$  is from the stimulated Raman transitions that drive the gate. Application of a second Mølmer-Sørensen gate imprints phase  $\phi_{G2}$  and results in the state

$$|\psi\rangle = |0\rangle\left(\alpha(1 - e^{i\phi_{G2}}e^{-i\phi_{G1}})|0\rangle - 2i\beta|1\rangle\right) + |1\rangle\left(-i\alpha(e^{-i\phi_{G2}} + e^{-i\phi_{G1}})\right)|1\rangle \quad (6.3)$$

If the phase of the second gate is shifted by  $\pi$  relative to the first gate ( $\phi_{G2} = \phi_{G1} + \pi$ ),



then the resulting state is

$$|\psi\rangle = |0\rangle(\alpha|0\rangle - i\beta|1\rangle) \quad (6.4)$$

which moves the coherence into the memory up to a single qubit rotation. Since this scheme makes use of a Mølmer-Sørensen gate, it does not rely on being in the ground state of motion and may offer practical advantages over quantum logic spectroscopy.

It is likely that the state of the photonic link qubit will need to be read out for various diagnostic purposes, although once a gate between the photonic link qubits and the memory qubits is functional, the state of the photonic link qubit can be read out via entanglement swapping in to the memory. Alignment of an entangling gate between photonic and memory qubits will be simpler with state detection of the photonic qubit. Consider the case of a Mølmer-Sørensen gate between barium ions (photonic link) and ytterbium ions (memory qubit). If the initial state of the systems is  $|\psi_{\text{Yb}}\psi_{\text{Ba}}\rangle$  is  $|0\rangle|0\rangle$ , an entangling gate produces the state  $|00\rangle + ie^{i\phi_G}|11\rangle$  after the gate time  $t_g = 2\pi/\delta$ . The time evolution of the Mølmer-Sørensen gate, including the motional state (denoted by the semi-colon in the ket) is

$$\begin{aligned} 2|\psi, t\rangle = & |\downarrow_{\phi_1}\downarrow_{\phi_2}; 0\rangle - e^{i\phi_{S1}}e^{i\Phi}|\uparrow_{\phi_1}\downarrow_{\phi_2}; \alpha\rangle - e^{i\phi_{S2}}e^{i\Phi}|\downarrow_{\phi_1}\uparrow_{\phi_2}; -\alpha\rangle \\ & + e^{i\phi_{S1}}e^{i\phi_{S2}}|\uparrow_{\phi_1}\uparrow_{\phi_2}; 0\rangle \end{aligned} \quad (6.5)$$

with  $|\uparrow_{\phi}\rangle = (-e^{-i\phi_S}|0\rangle + |1\rangle)/\sqrt{2}$  and  $|\downarrow_{\phi}\rangle = (|0\rangle + e^{i\phi_S}|1\rangle)/\sqrt{2}$  and  $|\alpha\rangle$  is a coherent state of motion, and the time dependence of the states is in the phase factors  $\phi_{S1,2}$

and  $\Phi$ . Making the substitution in to basis states  $|0\rangle, |1\rangle$ , the time dependence is

$$4|\psi, t\rangle = |00A\rangle + e^{i\phi_{S1}}e^{i\phi_{S2}}|11B\rangle + e^{i\Phi}e^{i\phi_{S2}}|01C\rangle + e^{i\Phi}e^{i\phi_{S1}}|10D\rangle \quad (6.6)$$

where the time-dependent, motional state amplitudes are denoted by the letters

$$\begin{aligned} |A\rangle &= 2|0\rangle + e^{i\Phi}(|\alpha\rangle + |-\alpha\rangle) \\ |B\rangle &= 2|0\rangle - e^{i\Phi}(|\alpha\rangle + |-\alpha\rangle) \\ |C\rangle &= |\alpha\rangle - |-\alpha\rangle \\ |D\rangle &= -|\alpha\rangle + |-\alpha\rangle \end{aligned} \quad (6.7)$$

The square of the motional states give the time dependence of the populations. Note that  $\langle\alpha|\alpha\rangle = \langle-\alpha|-\alpha\rangle = 1$ ,  $\langle-\alpha|\alpha\rangle = \langle\alpha|-\alpha\rangle = e^{-2|\alpha|^2}$ , and  $\langle 0|\pm\alpha\rangle = \langle\pm\alpha|0\rangle = e^{-|\alpha|^2/2}$ . Using these relations, the squares of the time-dependent motional amplitudes give the probability of finding the ions in their qubit states. Specifically, the time dependent qubit states are

$$\begin{aligned} P_{00} &= \frac{3}{8} + \frac{1}{8}e^{-2|\alpha|^2} + \frac{1}{2}e^{-|\alpha|^2/2}\cos\Phi \\ P_{11} &= \frac{3}{8} + \frac{1}{8}e^{-2|\alpha|^2} - \frac{1}{2}e^{-|\alpha|^2/2}\cos\Phi \\ P_{10} &= P_{01} = \frac{1}{8} - \frac{1}{8}e^{-2|\alpha|^2} \end{aligned} \quad (6.8)$$

Aligning a Mølmer-Sørensen gate can be done by examining these time-dependent populations and verifying that  $P_{00} = P_{11}$  while  $P_{01} = P_{10} = 0$  while scanning the

symmetric detuning from the motional modes  $\delta$ .

If the photonic link qubit ( $\text{Ba}^+$ ) is not directly measured, tracing over the photonic qubit after producing the state  $|00\rangle + |11\rangle$  results in the density matrix  $\rho_{\text{Yb}} = |0\rangle\langle 0| + |1\rangle\langle 1|$ , a classical mixed state with no quantum coherence. Proving dual species entanglement without detecting the state of both of the qubits will be indirect at best. There are subtle changes to the two ion spectrum upon tracing over a single ion while scanning the Mølmer-Sørensen gate detuning for fixed gate time. This can be shown by tracing over the state of one the barium photonic link qubit in Eqn. 6.6. The resulting reduced density matrix  $\rho_{\text{Yb}} = \text{Tr}_{\text{Ba}}(|\psi, t\rangle\langle\psi, t|) = \sum_{m=0,1} \text{Ba} \langle m|\rho|m\rangle_{\text{Ba}}$  is equal to a statistical mixture of pure states, each with probability  $1/2$ .

$$\begin{aligned} \rho_{\text{Yb}} = & |0A\rangle\langle 0A| + |0A\rangle\langle 1C| + |1B\rangle\langle 1B| + |1B\rangle\langle 0D| \\ & + |1C\rangle\langle 0A| + |1C\rangle\langle 1C| + |0D\rangle\langle 1B| + |0D\rangle\langle 0D| \end{aligned} \quad (6.9)$$

The probabilities of measuring the memory ( $^{171}\text{Yb}^+$ ) qubit states  $|0\rangle$  and  $|1\rangle$  are given by  $\langle A|A\rangle + \langle D|D\rangle$  and  $\langle B|B\rangle + \langle C|C\rangle$  respectively, yielding

$$\begin{aligned} P(|1\rangle_{\text{Yb}}) &= \frac{1}{2} - \frac{1}{2}e^{-|\alpha|^2/2} \cos \Phi \\ P(|0\rangle_{\text{Yb}}) &= \frac{1}{2} + \frac{1}{2}e^{-|\alpha|^2/2} \cos \Phi \end{aligned} \quad (6.10)$$

The equations for the time evolution of the qubit state probabilities of a dual species Mølmer-Sørensen gate (Eqn. 6.6) differ slightly if one of the qubits is traced over

(Eqn. 6.10). Fig. 6.2 shows these differences, and it can be seen that scanning the symmetric detuning from the sidebands of motion with constant laser intensity and time produces different probabilities of detecting  $|1\rangle$  or  $|11\rangle$ . Seeing these qualitative differences may prove useful in determining the calibration of an entangling gate, but the observation of such a spectrum does not prove entanglement between the two different qubit species. The phase coherence of the qubits must be probed to determine fidelity, requiring state detection of both qubits.

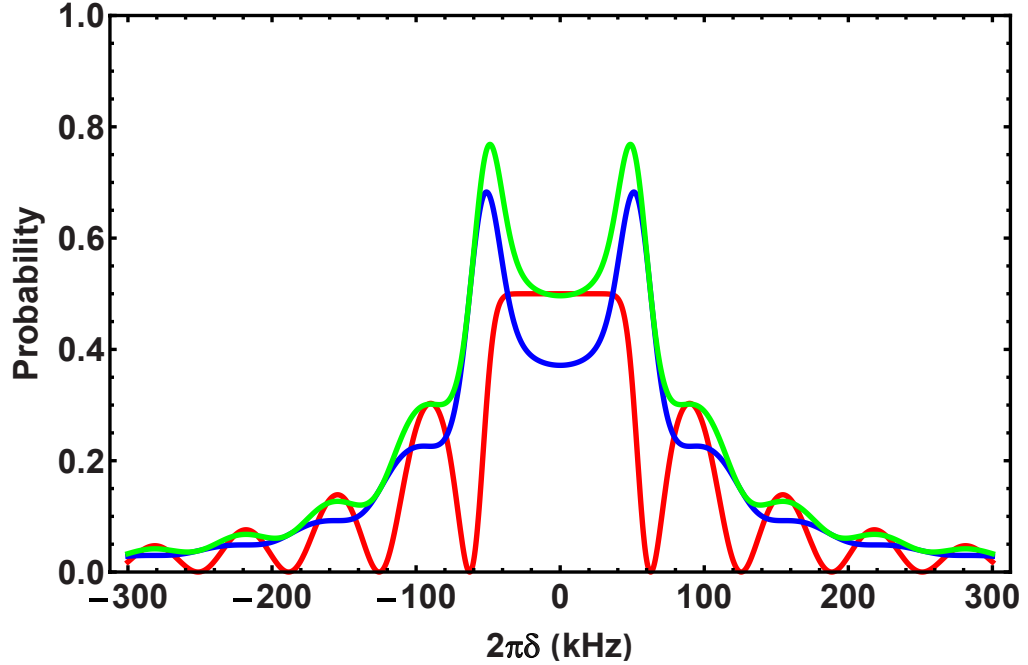


Figure 6.2: State detection of a barium-ytterbium Mølmer-Sørensen gate. The laser intensity is set to  $\eta\Omega = 2\pi \times 5\text{kHz}$ , and the probability of detecting qubit states is shown vs. symmetric detuning from the red and blue sidebands of motion. The red curve shows the probability of detecting the  $^{171}\text{Yb}^+$  qubit in the  $|1\rangle$  state with no spin interaction with the barium ion. In this case, there is only entanglement between the spin and the motion of the  $^{171}\text{Yb}^+$  ion. The blue curve shows the probability of measuring both qubits in the state  $|1\rangle$  and would be seen if the both qubits are measured. The green curve shows the probability of measuring the  $^{171}\text{Yb}^+$  ion in the state  $|1\rangle$  if the state of the barium ion is traced over. All three curves assume both qubits are in the motional ground state  $|0\rangle_m$ .

## 6.2 State detection of qubits based on entanglement

Nuclear spin  $1/2$  ion qubits have relatively simple schemes for state detection based on differential fluorescence of the qubit levels. Laser light resonant with the  $F = 1 \rightarrow F = 0$  levels of the  $S_{1/2} \rightarrow P_{1/2}$  electronic transition will produce scattered photons if the qubit is in the state  $|F, m_F\rangle = |1, 0\rangle$  while the state  $|0, 0\rangle$  will be off-resonant with the laser light, producing no scattered photons. The qubit states do not mix because of electric dipole transition selection rules. State detection based on differential fluorescence of qubit levels can be further improved by using Bayes' theorem and photon arrival time information to update the estimated qubit state [112, 113]. In qubits with nuclear spin greater than  $1/2$ , it is possible to create differential fluorescence between qubit levels by using a laser to shelve one of the qubit states to a metastable electronic state, often a  $D_{5/2}$  state with trapped ions. This shelving process has the drawback of using a relatively narrow laser to drive an electric quadrupole transition from  $S_{1/2} \rightarrow D_{5/2}$ .

In addition to using photon number and photon arrival time information for state detection, it is possible to use more photonic degrees of freedom to make measurements of the qubit state. Since the state of a single scattered photon is entangled with its parent atomic state, atom-photon entanglement can be used to determine the qubit state by measuring the photon state. This measurement technique relies on the fidelity of the atom-photon entanglement and must be independently calibrated. The use of a single photon for state detection of a qubit is necessarily probabilistic because single photons are sampled from the full solid angle and single

photon detectors typically have quantum efficiency below unity.

The architecture of a modular system is naturally amenable to perform state detection based on atom-photon entanglement on the photonic link qubit. A resonant, ultrafast laser pulse excites the photonic link atom to generate a single photon. The single photon is collected with a high numerical aperture objective and coupled into a single mode optical fiber where the photon degree of freedom is subsequently measured.

A proof of principle experiment showing state readout by using qubit-photon entanglement was carried out using a trapped  $^{172}\text{Yb}^+$  ion. This isotope has no nuclear spin; the qubit levels are the electron spin projection along the quantization axis defined by an external magnetic field:  $|0\rangle = |1/2, -1/2\rangle$  and  $|1\rangle = |1/2, 1/2\rangle$ . After Doppler cooling, this ion is optically pumped to the state  $|0\rangle$  with circularly polarized light. This light is directed along the quantization axis through the free-space, low NA objective, through the ion trap, and through the high NA microscope objective toward the single photon collection fiber (See Fig. 6.3). Because some of this laser light is coupled to the optical fiber and is detected by the PMTs, a delay of  $30\ \mu\text{s}$  is added to allow the PMTs to recover. Raman lasers or rf radiation can be used to manipulate the qubit, and detection proceeds via ultrafast  $\pi$ -polarized excitation of the  $S_{1/2}$  levels to the  $P_{1/2}$  levels. The resulting spontaneously emitted photon's polarization is entangled with the qubit state (see Fig. 6.3). The optical fiber filters out  $\pi$ -polarized radiation from the qubit; only  $\sigma^\pm$  polarized light enters the fiber. This single photon is converted from the  $|\sigma^\pm\rangle$  basis to the  $\{|H\rangle, |V\rangle\}$  basis, sorted by thin film polarizers, and detected by PMTs.

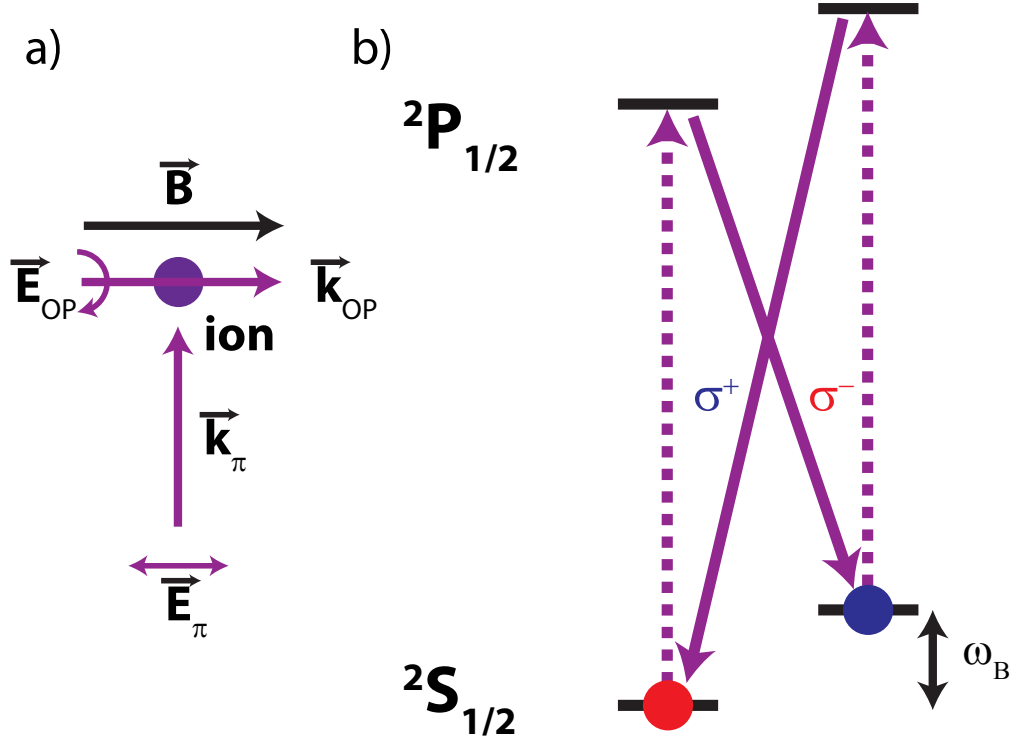


Figure 6.3: Laser geometry and state detection scheme for nuclear spin 0 ion. **(a)** The magnetic field and laser geometry for optical pumping and resonant excitation. The magnetic field is oriented along the optical fiber direction for collection of  $\sigma^\pm$  photons from an atom in to an optical fiber. State preparation is performed with circularly polarized light along the quantization axis to optically pump the ion. An ultrafast, resonant laser excites the  $S_{1/2} \rightarrow P_{1/2}$  transition at 369 nm to generate a single photon. **(b)** The excited state decays, resulting in entanglement between the photon polarization and the qubit state. Detection of the photon polarization state projects the atom into the resulting spin state. Comparing the fraction of  $\sigma^\pm$  photons detected gives statistics about the atom state.

Fig. 6.4 shows manipulation of the spin-qubit by driving a four photon Raman transition. The laser impinges on the trapped ion at a 90 degree angle from the magnetic field with circular polarization viewed from the laser propagation direction. In the basis defined by the magnetic field, the trapped ion sees a rotating field with time dependent  $\mathbf{x}$ -polarization and  $\pi$ -polarization. Because of the laser beatnote between the copropagating Raman lasers, the  $\mathbf{x}$ -polarization and  $\pi$ -polarization beat at the laser frequency difference with timescale much shorter than the Rabi frequency. The ion therefore experiences both  $\mathbf{x}$ -polarization and  $\pi$ -polarization on average, thus enabling multi-photon Raman transitions.

A Raman spectrum showing the  $|m_J\rangle = |-\frac{1}{2}\rangle \leftrightarrow |\frac{1}{2}\rangle$  four photon transition as a function of the Raman laser beatnote is shown in Fig. 6.5a in addition to Rabi flopping on the transition in Fig. 6.5b. Interestingly, the number of photons involved in the transition may be read out directly using Ramsey interferometry as shown in Fig. 6.5c. A Ramsey experiment was performed with a  $\pi/2$  pulse followed by a second  $\pi/2$  pulse with a phase advance of one of the copropagating Raman lasers. The transition shown in the figure shows two Ramsey fringes in  $2\pi$  of phase advance of the second  $\pi/2$  pulse. The two fringes arise from the phase of the second  $\pi/2$  pulse being written twice to the atom; the transition is a four-photon transition. Note this is generally applicable to any Raman transition and may be used to directly read off the number of photons involved in the Raman transition.

The state detection fidelity shown in the figures is limited by several factors. Optical pumping is sensitive to the polarization of the laser, and we observe a  $\sim 2\%$  error due to imperfect polarization control of the optical pumping laser. In addi-



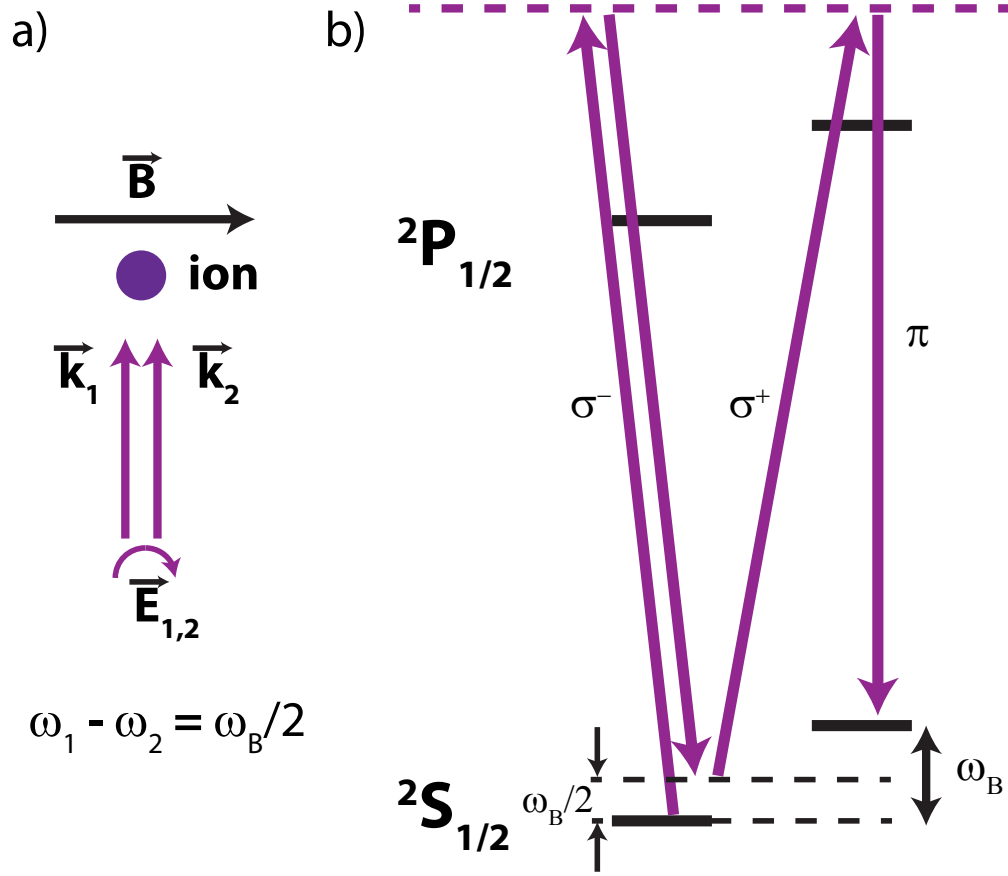


Figure 6.4: Qubit manipulations of a  $^{172}\text{Yb}^+$  ion. **(a)** After optically pumping the ion to the  $|0\rangle = |1/2, -1/2\rangle$  state, a copropagating Raman transition is driven by a mode locked laser at 355 nm. The incident light is orthogonal to the magnetic field and is circularly polarized with respect to the propagation direction. The resulting electric field polarization in the atom's quantization basis has time dependent  $\sigma^\pm$  polarization and  $\pi$  polarization. The relative polarizations at frequency  $\omega_{1,2}$  beat at the laser frequency difference  $\omega_1 - \omega_2$ . **(b)** When the beatnote of the laser matches half of the frequency difference between the  $|0\rangle = |1/2, -1/2\rangle$  and  $|1\rangle = |1/2, 1/2\rangle$  levels, a four-photon Raman transition can be driven between  $|0\rangle$  and  $|1\rangle$ . Because the Rabi frequency is much less than the laser beatnote, the atom sees all polarizations from both frequency components of the light. The figure depicts a single, four photon path for a Raman transition.

tion, the ion-photon entanglement fidelity, and integral part of this state detection method, is limited to  $\sim 0.92$ , likely due to inhomogeneous stress on the vacuum window glass. Both of these hurdles may be overcome to increase the state detection fidelity. Because of the probabilistic nature of this state detection method, this experiment is repeated as quickly as possible, but the repetition rate of the experiment was limited by the PMT recovery time after optical pumping. With an experimental repetition rate of  $\sim 30$  kHz, collecting 300 photons required about 60 seconds of time.

Though the demonstration of this state detection technique has relatively low fidelity compared to other standard state detection methods, including shelving to a metastable electronic state, this detection method makes use of existing hardware (without adding more) likely in a modular system to detect the photonic qubit. This method relies on optically pumping the photonic qubit, a necessity for making remote entanglement, and then exciting the qubit with a resonant, ultrafast laser pulse to make single photons which are subsequently collected and detected. In addition, this technique may find other uses on transitions that quench or are pumped to a dark state after scattering only one or a few photons.

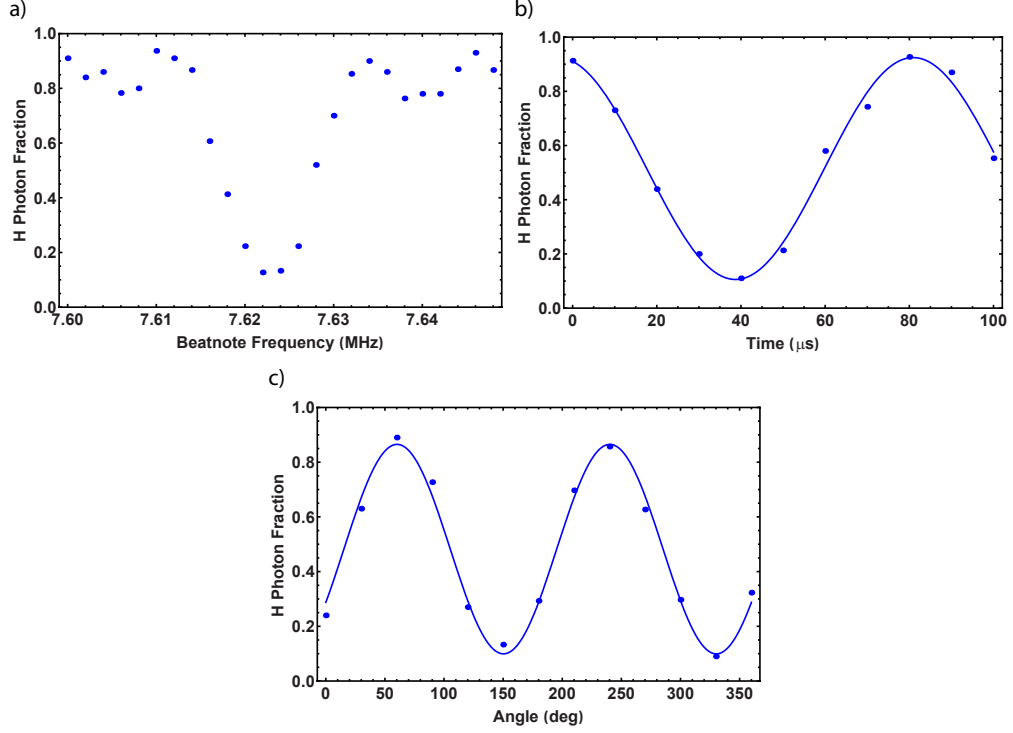


Figure 6.5: Raman spectrum and Rabi flopping between qubit levels of a  $^{172}\text{Yb}^+$  ion. **(a)** Scan of co-propagating Raman laser beatnote incident on a  $^{172}\text{Yb}^+$  ion. When the laser beatnote  $\omega_1 - \omega_2 = \omega_B/2$ , a resonant, four-photon Raman transition can be driven between qubit levels. With an applied magnetic field of  $\sim 5.4$  G, the four photon transition can be found at  $\omega_B/2 \approx 7.62$  MHz. **(b)** Rabi flopping between qubit levels using a four photon transition. **(c)** A Ramsey experiment is performed on the transition by performing a  $\pi/2$  rotation on the qubit, followed by a second  $\pi/2$  rotation with variable phase set by an AOM. The resulting two Ramsey fringes show the four photon nature of the transition: the phase is written on the atom twice in a four photon transition.

## Chapter 7: **Outlook**

The experiments in this thesis suggest that the use of high quality clocks may be important in the operation of a modular quantum network. Manipulation of qubits using optical fields among and between different modules introduces challenges in controlling the optical phase. However, as presented in Chapter 4, the sensitivity to the optical phase can be eliminated through appropriate geometry and RF frequency generation. The modular phase control system presented in Chapter 4 is a flexible, expandable control system and can be expanded to include different modules in different locations while maintaining phase coherent operations across the entire quantum network. The distribution of the clock signal and the phase insensitive laser geometry ensure that different modules, perhaps separated by large distances, can be used. Each module may have its own separate laser system and may be completely independent of other modules. The addition of the modules to a quantum network requires using the clock signal to stabilize the RF or microwave domain of the laser system (a frequency comb in this thesis). If a frequency comb is used, stabilization of the Raman laser beatnote at the qubit frequency may be accomplished by directly locking the beatnote near the qubit frequency using the clock signal. In  $^{171}\text{Yb}^+$  ions, this lock is near 12.6 GHz [87], necessitating distri-

bution of the microwave signal over long distances in a quantum network. Direct broadcast through the atmosphere may prove challenging at this frequency over long distances. Alternatively, if a frequency comb clock standard is developed, frequency combs with large bandwidth at telecommunication wavelengths could be used. The telecom comb could then be filtered and the microwave frequency components could be used as the clock at each module. Alternatively, the repetition rate of the laser may be stabilized [80]. In this scenario, the distributed clock signal must be of order the laser repetition rate, typically of order  $\sim 100$  MHz, and may be directly broadcast through the atmosphere.

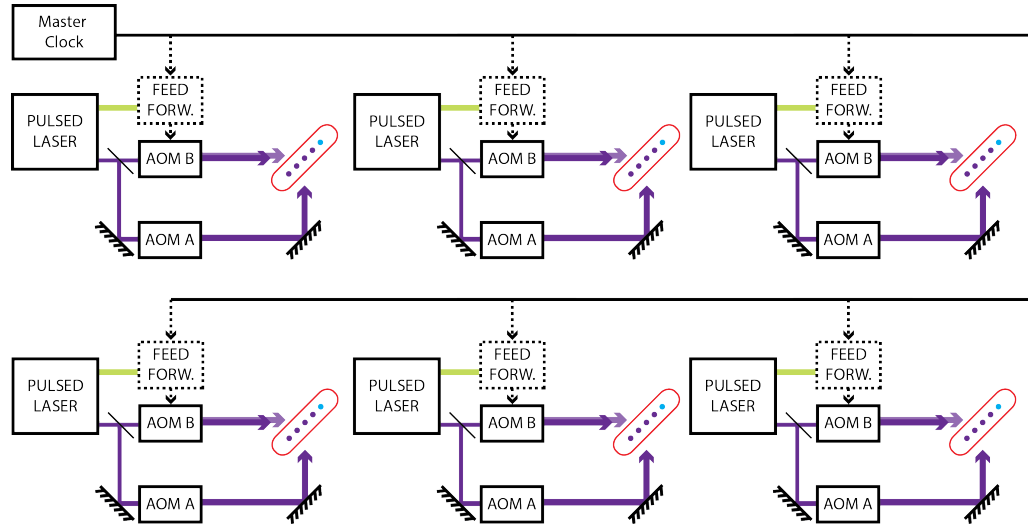


Figure 7.1: A modular quantum system of trapped atomic ions. A master clock distributes a phase reference signal to control the absolute phase of all coherent operations, including entanglement, within and between each module. The laser geometry is chosen to cancel the optical phase from the pulsed laser frequency combs, so separate pulsed lasers may be used for coherent operations in such an architecture. The number of qubits may be increased by adding more modules. The photonic link (blue) and the memory qubits are non-identical to limit cross talk between the photon and phonon mediated entanglement buses.

As discussed in Chapter 6, the use of at least two trapped ion species appears necessary in a modular system that is connected by a photonic network. Multiple

trapped ion species help prevent cross talk from resonant photon scattering between the optical link qubits and the memory qubits. In addition, using multiple ion species allows for intermittent laser cooling of ions not storing superposition states. Optical frequency combs that span the UV and visible spectrum may play an important role in such a system. Diffraction gratings may be used to split up the frequency comb, and the phase coherence of such a comb locked to an external clock would allow for entangling gates and entanglement swapping between different ion species. An early demonstration of the phase coherence between different parts of the optical spectrum is shown in Fig. 7.2. A Ramsey experiment is performed on an ion using co-propagating Raman lasers. A  $\pi/2$  pulse at 355 nm is followed by a  $\pi/2$  pulse at 532 nm with variable phase shows a clear oscillation in the figure, demonstrating cancellation of the optical phase.

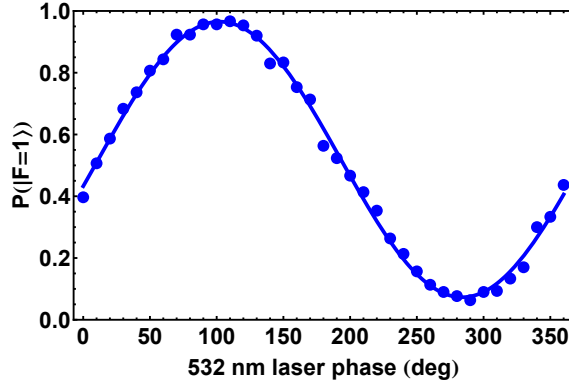


Figure 7.2: Phase coherent  $^{171}\text{Yb}^+$  qubit manipulations across the optical spectrum of a frequency comb. Using a copropagating laser geometry to cancel dependence of the optical laser phase, a Ramsey experiment is performed using a  $\pi/2$  rotation at 355 nm followed by a  $\pi/2$  rotation at 532 nm. The absolute phase control architecture may be expanded across the optical domain of a frequency comb for coherent control of multi-species qubit modules.

The photonic connection between nodes through the interference of distin-

guishable photons may also be extended to include qubits of differing physical origin with the development of ultrafast single photon detectors in combination with the use of optical clocks as outlined in Chapter 3. In addition, the lineshape of the distinguishable photons may be matched by using media with high dispersion to provide high-fidelity entangled states. Current single photon detector bandwidths are limited to  $\sim 100$  GHz, preventing the bridging of photon frequency differences in the optical domain. Given currently available technology for single photon detectors, the techniques described in Chapter 3 would likely be of use in some solid state systems, such as NV centers and quantum dots. Slow differential drifts in the photon frequency can be accounted for by performing spectroscopy periodically on the qubit and following the phase correction scheme outlined in Chapter 3.

Extending the distance of the quantum network will also be important for scaling up the number of qubits in the system. The collection of single photons from  $^{171}\text{Yb}^+$  atomic ions in this thesis have typical attenuation of  $\sim 100$  dB/km at 369 nm in a high-quality single mode fiber for UV and visible light. The high attenuation of these photon wavelengths prohibit their use for long distance communication, even in a quantum repeater network. The transmission of light at visible wavelengths is considerably better. Trapped barium ions emit light at 493 nm (see Fig. 7.3) which has an attenuation of  $\sim 10$  dB/km, and at 650 nm which has an attenuation of  $\sim 5$  dB/km. Efficient down-conversion of these wavelengths to the telecommunication band should improve the distance between modules in a quantum network.

Finally, in order to make a fault-tolerant modular quantum system, the fidelity of the operations presented in this thesis will have to be vastly improved. Several

research groups have made significant progress on fault tolerant state detection, single qubit rotations, and two qubit entangling gates between ions in the same module [113, 114]. Demonstrating higher fidelity remote entanglement and the integration of the techniques used for high fidelity operations in a single ion trap should be an exciting area in the future.

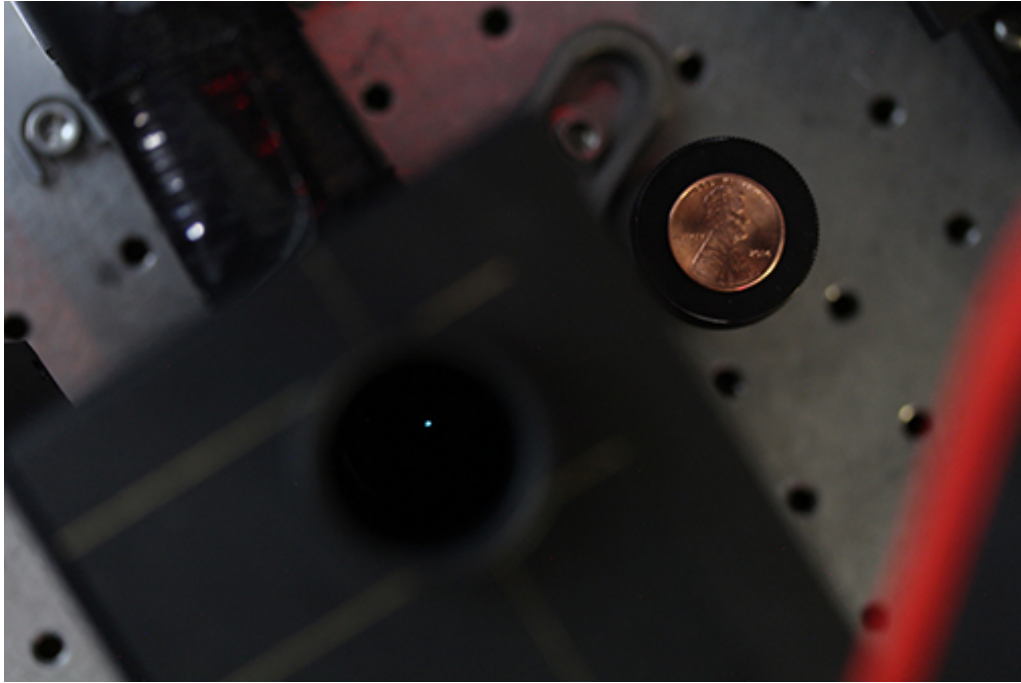


Figure 7.3: Color photograph of a single barium atom. The blue green dot ( $\lambda = 493$  nm) is a single  $^{138}\text{Ba}^+$  atom. The view is down a high numerical aperture microscope objective. A standard, commercial SLR camera was used to take this photograph. This photograph has not been retouched and is not a composite photo. The exposure time is 25 seconds so that some of the optical bench is visible. The atom is also easily visible with the naked eye from the same vantage point. Image credit: Volkan Inlek and Emily Edwards.



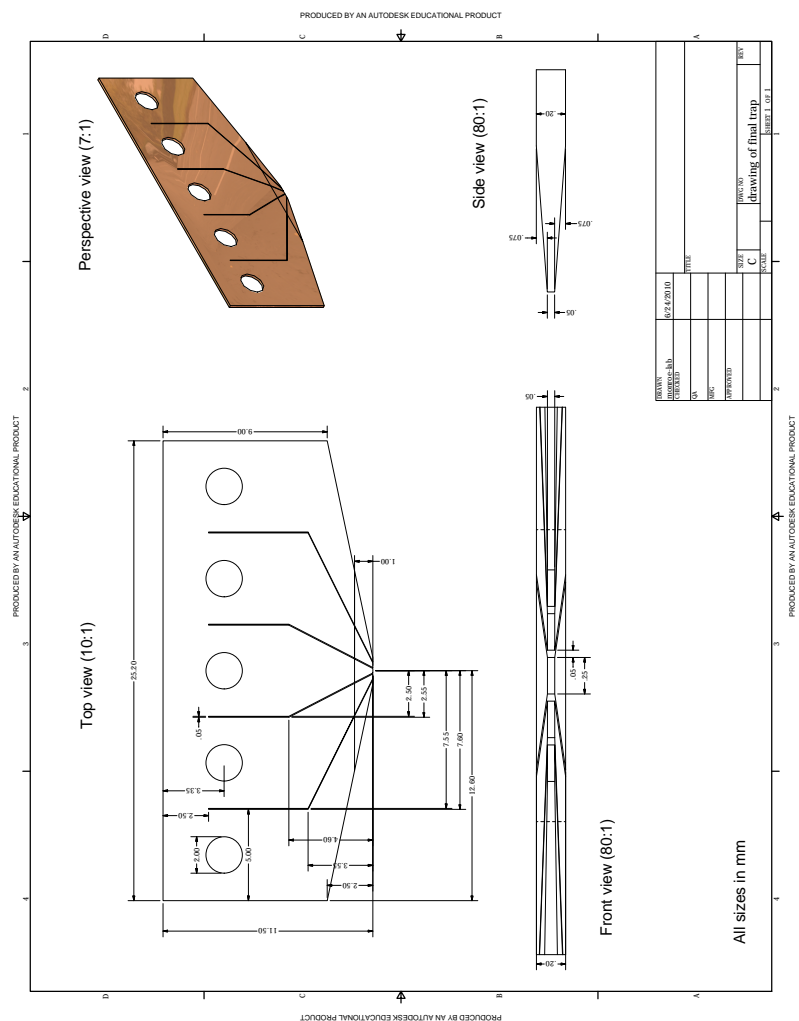
Chapter A: **Appendix**

Figure A.1: Ion trap blades used in this thesis

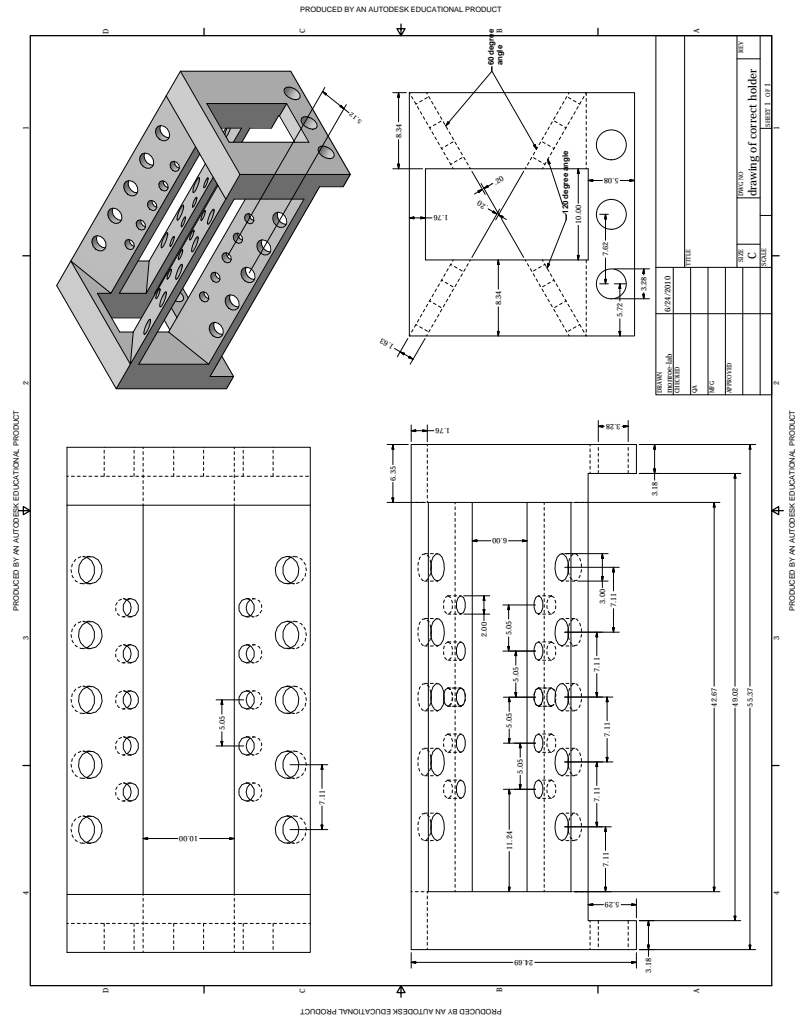


Figure A.2: Ion trap blade holder used in this thesis





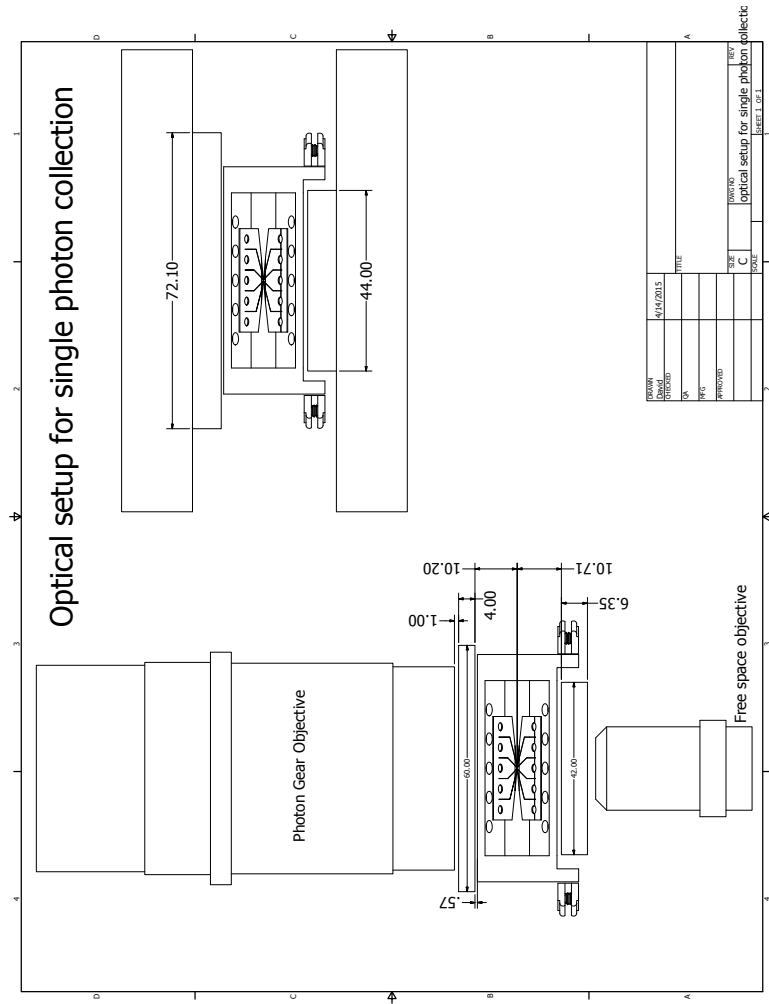


Figure A.5: Optical setup for single photon collection

## Bibliography

- [1] Nielsen, M. A. & Chuang, I. L. *Quantum Computation and Quantum Information* (Cambridge University Press, 2000).
- [2] Lloyd, S. Universal quantum simulators. *Science* **273**, 1073–1078 (1996).
- [3] Deutsch, I. Quantum simulation: dream or nightmare. *APS News Letter: The Quantum Times* **5**, 7 (2010).
- [4] Haroche, S. & Raimond, J. M. Quantum computing: dream or nightmare. *Phys. Today* **49**, 51 (1996).
- [5] Landauer, R. Is quantum mechanics useful. *Phil. Trans. R. Soc. Lond. A* **353**, 367 (1995).
- [6] Landauer, R. The physical nature of information. *Phys. Lett. A* **217**, 188 (1996).
- [7] Shor, P. Algorithms for quantum computation: Discrete logarithms and factoring. *In Proc. Annu. Symp. Found. Comput. Sci.* 124–134 (1994).

- [8] Cirac, J. I. & Zoller, P. Quantum computations with cold trapped ions. *Phys. Rev. Lett.* **74**, 4091 (1995).
- [9] Monroe, C., Meekhof, D. M., King, B. E., Itano, W. M. & Wineland, D. J. Demonstration of a fundamental quantum logic gate. *Phys. Rev. Lett.* **75**, 4714 (1995).
- [10] Shor, P. W. Scheme for reducing decoherence in a quantum memory. *Phys. Rev. A* **52**, R2493 (1995).
- [11] Shor, P. W. Fault-tolerant quantum computation. *arXiv:quant-ph* (1996).
- [12] Kielpinski, D., Monroe, C. & Wineland, D. J. Architecture for a large scale quantum computer. *Nature* **417**, 709–711 (2002).
- [13] Blatt, R. & Wineland, D. J. Entangled states of trapped atomic ions. *Nature* **453**, 1008–1015 (2008).
- [14] Childress, L. & Hanson, R. Diamond nv centers for quantum computing and quantum networks. *MRS Bulletin* **38**, 134–138 (2013).
- [15] Childress, L., Walsworth, R. & Lukin, M. D. Atom-like crystal defects: from quantum computers to biological sensors. *Physics Today* **67**, 38 (2014).
- [16] Xiang, Z.-L., Ashhab, S., You, J. Q. & Nori, F. Hybrid quantum circuits: Superconducting circuits interacting with other quantum systems. *Rev. Mod. Phys.* **85**, 623–653 (2013).

- [17] Monroe, C. *et al.* Large scale modular quantum computer architecture with atomic memory and photonic interconnects. *Phys. Rev. A* **89**, 022317 (2014).
- [18] Hensinger, W. K. *et al.* T-junction ion trap array for two-dimensional ion shuttling, storage, and manipulation. *App. Phys. Lett.* **88**, 034101 (2006).
- [19] Hucul, D. *et al.* On the transport of atomic ions in linear and multidimensional ion trap arrays. *Quant. Inf. Comp.* **8**, 501–578 (2008).
- [20] Hucul, D. *et al.* Modular entanglement of atomic qubits using photons and phonons. *Nature Physics* **11**, 37–42 (2015).
- [21] Hayes, D. *et al.* Coherent error suppression in multiqubit entangling gates. *Phys. Rev. Lett.* **109**, 020503 (2012).
- [22] Olmschenk, S. *et al.* Manipulation and detection of a trapped  $\text{Yb}^+$  hyperfine qubit. *Phys. Rev. A* **76**, 052314 (2007).
- [23] Berkeland, D. J. & Boshier, M. G. Destabilization of dark states and optical spectroscopy in zeeman-degenerate atomic systems. *Phys. Rev. A* **65**, 033413 (2002).
- [24] Olmschenk, S. *Quantum teleportation between distant matter qubits*. Ph.D. thesis, University of Michigan (2009).
- [25] Acton, M. *Detection and control of individual trapped ions and neutral atoms*. Ph.D. thesis, University of Michigan (2008).



- [26] Acton, M. *et al.* Near-perfect simultaneous measurement of a qubit register. *Quantum Inf. Comp.* **6**, 465 (2006).
- [27] Mizrahi, J. *Ultrafast Control of Spin and Motion in Trapped Ions*. Ph.D. thesis, University of Maryland (2013).
- [28] Campbell, W. *et al.* Ultrafast gates for single atomic qubits. *Phys. Rev. Lett.* **105**, 090502 (2010).
- [29] Metcalf, H. & van der Straten, P. *Laser cooling and trapping* (Springer, 1999).
- [30] Wootters, W. K. & Zurek, W. H. A single quantum cannot be cloned. *Nature* **299**, 802 (1982).
- [31] Bennett, C. H. *et al.* Teleporting an unknown quantum state via dual channel classical and einstein-podolsky-rosen channels. *Phys. Rev. Lett.* **70**, 1895 (1993).
- [32] Briegel, H.-J., Dür, W., Cirac, J. I. & Zoller, P. Quantum repeaters: The role of imperfect local operations in quantum communication. *Phys. Rev. Lett.* **81**, 5932 (1998).
- [33] Simon, C. & Irvine, W. T. M. Robust long-distance entanglement and a loophole-free bell test with ions and photons. *Phys. Rev. Lett.* **91**, 110405 (2003).
- [34] Freedman, S. & Clauser, J. Experiment test of local hidden-variable theories. *Phys. Rev. Lett.* **28**, 938–941 (1972).

- [35] Scully, M. & Druhl, K. Quantum eraser: a proposed photon correlation experiment concerning observation and “delayed choice” in quantum mechanics. *Phys. Rev. A* **25**, 2208 (1982).
- [36] Ma, X. *et al.* Experimental delayed-choice entanglement swapping. *Nature Physics* **8**, 479–484 (2012).
- [37] Kómár, P. *et al.* A quantum network of clocks. *Nature Physics* **10**, 582–587 (2014).
- [38] Cirac, J. I., Zoller, P., Kimble, H. J. & Mabuchi, H. Quantum state transfer and entanglement distribution among distant nodes in a quantum network. *Phys. Rev. Lett.* **78**, 3221–3224 (1997).
- [39] Duan, L.-M., Lukin, M. D., Cirac, J. I. & Zoller, P. Long-distance quantum communication with atomic ensembles and linear optics. *Nature* **414**, 413–418 (2001).
- [40] Cabrillo, C., Cirac, J. I., Garcia-Fernandez, P. & Zoller, P. Creation of entangled state of distant atom by interference. *J. Appl. Phys.* **83**, 5025 (1998).
- [41] Duan, L.-M. & Monroe, C. *Colloquium: Quantum networks with trapped ions.* *Rev. Mod. Phys.* **82**, 1209–1224 (2010).
- [42] Ursin, R. *et al.* Entanglement-based quantum communication over 144 km. *Nature Physics* **3**, 481 (2007).

- [43] Luo, L. *et al.* Protocols and techniques for a scalable atom-photon quantum network. *Fortschr. Phys.* **57**, 1133–1152 (2009).
- [44] Blinov, B., Moehring, D., Duan, L. & Monroe, C. Observation of entanglement between a single trapped atom and a single photon. *Nature* **428**, 153 (2004).
- [45] Gao, W., Fallahi, P., Togan, E., Miguel-Sanchez, J. & Imamoglu, A. Observation of entanglement between a quantum dot spin and a single photon. *Nature* **491**, 426 (2012).
- [46] Togan, E. *et al.* Quantum entanglement between an optical photon and a solid-state spin qubit. *Nature* **466**, 730 (2010).
- [47] Kimble, H. J. The quantum internet. *Nature* **453**, 1023 (2008).
- [48] Bloch, I. Quantum coherence and entanglement with ultracold atoms in optical lattices. *Nature* **453**, 1016 (2008).
- [49] Moehring, D. L. *et al.* Entanglement of single-atom quantum bits at a distance. *Nature* **449**, 68 (2007).
- [50] Matsukevich, D. N., Maunz, P., Moehring, D. L., Olmschenk, S. & Monroe, C. Bell inequality violation with two remote atomic qubits. *Phys. Rev. Lett.* **100**, 150404 (2008).
- [51] Bernien, H. *et al.* Heralded entanglement between solid-state qubits separated by three metres. *Nature* **497**, 86 (2013).

- [52] Chou, C. W. *et al.* Measurement-induced entanglement for excitation stored in remote atomic ensembles. *Nature (London)* **438**, 828–832 (2005).
- [53] Ritter, S. *et al.* An elementary quantum network of single atoms in optical cavities. *Nature* **484**, 195 (2012).
- [54] Casabone, B. *et al.* Heralded entanglement of two ions in an optical cavity. *Phys. Rev. Lett.* **111**, 100505 (2013).
- [55] Legero, T., Wilk, T., Kuhn, A. & Rempe, G. Time-resolved two-photon quantum interference. *Appl. Phys. B* **77**, 797–802 (2003).
- [56] Metz, J. & Barrett, S. D. Effect of frequency-mismatched photon in quantum-information processing. *Phys. Rev. A* **77**, 042323 (2008).
- [57] Dyckovsky, A. M. & Olmschenk, S. Analysis of photon-mediated entanglement between distinguishable matter qubits. *Phys. Rev. A* **85**, 052322 (2012).
- [58] Zhao, T. M. *et al.* Entangling different-color photons via time resolved measurement and active feed forward. *Phys. Rev. Lett.* **112**, 103602 (2014).
- [59] Vittorini, G., Hucul, D., Inlek, I. V., Crocker, C. & Monroe, C. Entanglement of distinguishable quantum memories. *Phys. Rev. A* **90**, 040302(R) (2014).
- [60] Barrett, M. *et al.* Deterministic quantum teleportation of atomic qubits. *Nature* **429**, 737–739 (2004).
- [61] Steffen, L. *et al.* Deterministic quantum teleportation with feed-forward in a solid state system. *Nature* **500**, 319 (2013).

- [62] Olmschenk, S. *et al.* Quantum teleportation between distant matter qubits. *Science* **323**, 486–489 (2009).
- [63] Maunz, P. *et al.* Heralded quantum gate between remote quantum memories. *Phys. Rev. Lett.* **102**, 250502 (2009).
- [64] Furusawa, A. *et al.* Unconditional quantum teleportation. *Science* **282**, 706–709 (1998).
- [65] Nölleke, C. *et al.* Efficient teleportation between remote single-atom quantum memories. *Phys. Rev. Lett.* **110**, 140403 (2013).
- [66] Pfaff, W. *et al.* Unconditional quantum teleportation between distant solid state quantum bits. *Science* **345**, 532–535 (2014).
- [67] Moehring, D. *Remote Entanglement of Trapped Atomic Ions*. Ph.D. thesis, University of Michigan (2007).
- [68] Steane, A. Overhead and noise threshold of fault-tolerant quantum error correction. *Phys. Rev. A* **68**, 042322 (2003).
- [69] Knill, E. Quantum computing with realistically noisy devices. *Nature (London)* **434**, 39 (2005).
- [70] Kim, T., Maunz, P. & Kim, J. Efficient collection of single photons emitted from a trapped ion into a single-mode optical fiber for scalable quantum-information processing. *Phys. Rev. A* **84**, 063423 (2011).

- [71] Berkeland, D. J., Miller, J. D., Berquist, J. C., Itano, W. M. & Wineland, D. J. Minimization of ion micromotion in a paul trap. *J. Appl. Phys.* **83**, 5025 (1998).
- [72] Jackson, J. D. *Classical Electrodynamics* (John Wiley & Sons, Inc., 1999).
- [73] Kwiat, P. G. & Weinfurter, H. Embedded bell-state analysis. *Phys. Rev. A* **58**, R2623(R) (1998).
- [74] Sackett, C. A. *et al.* Experimental entanglement of four particles. *Nature* **404**, 256–259 (2000).
- [75] Chwalla, M. *et al.* Precision spectroscopy with two correlated atoms. *Appl. Phys. B* **89**, 483–488 (2007).
- [76] Wineland, D. J. *et al.* Experimental issues in coherent quantum-state manipulation of trapped ions. *J. Res. Nat. Inst. Stand. Tech.* **103**, 259 (1998).
- [77] Lee, P. J. *et al.* Phase control of trapped ion quantum gates. *Jour. Opt. B* **7**, S371–S383 (2005).
- [78] Lee, P. *Quantum information processing with two trapped cadmium ions*. Ph.D. thesis, University of Michigan (2005).
- [79] Hayes, D. *Remote and local entanglement of ions with photons and phonons*. Ph.D. thesis, University of Maryland (2012).
- [80] Hayes, D. *et al.* Entanglement of atomic qubits using an optical frequency comb. *Phys. Rev. Lett.* **104**, 140501 (2010).

- [81] Inlek, I. V., Vittorini, G., Hucul, D., Crocker, C. & Monroe, C. Quantum gates with phase stability over space and time. *Phys. Rev. A* **90**, 042316 (2014).
- [82] Ladd, T. D. *et al.* Quantum computers. *Nature* **464**, 45 (2010).
- [83] Häffner, H., Roos, C. F. & Blatt, R. Quantum computing with trapped ions. *Phys. Rep.* **469**, 155–203 (2008).
- [84] Tamarat, P. *et al.* Spin-flip and spin-conserving optical transitions of the nitrogen-vacancy centre in diamond. *New J. Phys.* **10**, 045004 (2008).
- [85] Press, D., Ladd, T., Zhang, B. & Yamamoto, Y. Complete quantum control of a single quantum dot spin using ultrafast optical pulses. *Nature* **456**, 218 (2008).
- [86] Weitenberg, C. *et al.* Single-spin addressing in an atomic mott insulator. *Nature* **471**, 319 (2011).
- [87] Islam, R. *et al.* Beat note stabilization of mode-locked laser for quantum information processing. *Optics Lett.* **39**, 3238–3241 (2014).
- [88] Ospelkaus, C. *et al.* Microwave quantum logic gates for trapped ions. *Nature* **476**, 181 (2011).
- [89] Leibfried, D. *et al.* Quantum dynamics of single trapped ions. *Rev. Mod. Phys.* **75**, 281 (2003).
- [90] Mølmer, K. & Sørensen, A. Entanglement and quantum computation with ions in thermal motion. *Phys. Rev. A* **62**, 022311 (2000).

- [91] Leibfried, D. *et al.* Experimental demonstration of a robust, high-fidelity geometric two ion-qubit phase gate. *Nature* **422**, 412 (2003).
- [92] Haljan, P. C. *et al.* Entanglement of trapped-ion clock states. *Phys. Rev. A* **72**, 062316 (2005).
- [93] Bermudez, A., Schmidt, P. O., Plenio, M. B. & Retzker, A. Robust trapped-ion quantum logic gates by continuous dynamical decoupling. *Phys. Rev. A* **85**, 040302 (2012).
- [94] Tan, T. R. *et al.* Demonstration of a dressed-state phase gate for trapped ions. *Phys. Rev. Lett.* **110**, 263002 (2013).
- [95] Lemmer, A., Bermudez, A. & Plenio, M. B. Driven geometric phase gates with trapped ions. *New J. Phys.* **15**, 083001 (2013).
- [96] Milburn, G. J., Schneider, S. & James, D. F. V. Ion trap quantum computing with warm ions. *Fortschr. Phys.* **48**, 801 (2000).
- [97] Solano, E. *et al.* Deterministic bell states and measurement of the motional state of two trapped ions. *Phys. Rev. A* **59**, R2539 (1999).
- [98] Zhu, S.-L., Monroe, C. & Duan, L.-M. Trapped ion quantum computation with transverse phonon modes. *Phys. Rev. Lett.* **97**, 050505 (2006).
- [99] Britton, J. W. *et al.* Engineered two-dimensional ising interactions in a trapped-ion quantum simulator with hundreds of spins. *Nature* **484**, 489 (2012).



- [100] Duan, L.-M. *et al.* Probabilistic quantum gates between remote atoms through interference of optical frequency qubits. *Phys. Rev. A* **73**, 062324 (2006).
- [101] Insight issue: Quantum simulation. *Nature Physics, Insight Issue: “Quantum Simulation,”* **8**, 263–299 (2012).
- [102] Giovannetti, V., Lloyd, S. & Maccone, L. Quantum metrology. *Phys. Rev. Lett.* **96**, 010401 (2006).
- [103] Isenhower, L. *et al.* Demonstration of a neutral atom controlled-not quantum gate. *Phys. Rev. Lett.* **104**, 010503 (2010).
- [104] Wilk, T. *et al.* Entanglement of two individual neutral atoms using rydberg blockade. *Phys. Rev. Lett.* **104**, 010502 (2010).
- [105] Dolde, F. *et al.* Room-temperature entanglement between single defect spins in diamond. *Nature Physics* **9**, 139–143 (2013).
- [106] Dicarlo, L. *et al.* Preparation and measurement of three-qubit entanglement in a superconducting circuit. *Nature* **467**, 574–578 (2010).
- [107] Neeley, M. *et al.* Generation of three-qubit entangled states using superconducting phase qubits. *Nature* **467**, 570–573 (2010).
- [108] Schmidt, P. O. *et al.* Spectroscopy using quantum logic. *Science* **309**, 749–752 (2005).
- [109] Barret, M. D. *et al.* Sympathetic cooling of  $^9\text{Be}^+$  and  $^{24}\text{Mg}^+$  for quantum logic. *Phys. Rev. A* **68**, 042302 (2003).

- [110] Pelc, J., Langrock, C., Zhang, Q. & Fejer, M. Influence of domain disorder on parametric noise in quasi-phase-matched quantum frequency converters. *Optics Lett.* **35**, 2804–2806 (2010).
- [111] Choi, T. *et al.* Optimal control of multimode couplings between trapped ion qubits for scalable entanglement. *Phys. Rev. Lett.* **112**, 19502 (2014).
- [112] Myerson, A. H. *et al.* High fidelity readout of trapped-ion qubits. *Phys. Rev. Lett.* **100**, 200502 (2008).
- [113] Noek, R. *et al.* High speed, high fidelity detection of an atomic hyperfine qubit. *Optics Lett.* **38**, 4735 (2013).
- [114] Harty, T. P. *et al.* High-fidelity preparation, gates, memory and readout of a trapped-ion quantum bit. *Phys. Rev. Lett.* **113**, 220501 (2014).